Impact of Gas Radiation on Viscous Flows, in particular on Wall Heat Loads, in Hydrogen-Oxygen vs. Methane-Oxygen Systems, based on the SSME Main Combustion Chamber

Andreas Thellmann

Universität der Bundeswehr München

Fakultät für Luft- und Raumfahrttechnik
Institut für Thermodynamik

Impact of Gas Radiation on Viscous Flows, in particular on Wall Heat Loads, in Hydrogen-Oxygen vs. Methane-Oxygen Systems, based on the SSME Main Combustion Chamber

Dipl.-Ing. Andreas Thellmann

Vollständiger Abdruck der bei der Fakultät für Luft- und Raumfahrttechnik
der Universität der Bundeswehr München zur Erlangung des akademischen Grades eines

Doktor-Ingenieurs (Dr.-Ing.)

genehmigten Dissertation.

Vorsitzender: Prof. Dr.-Ing. Dipl.-Kfm. Bernhard Katzy
1. Berichterstatter: Prof. Dr.-Ing. Christian Mundt
2. Berichterstatter: Prof. Dr. rer. nat. Klaus Hornung

Diese Dissertation wurde am 01.06.2010 bei der Universität der Bundeswehr
München, 85577 Neubiberg eingereicht und durch die Fakultät für Luft- und
Raumfahrttechnik am 16.06.2010 angenommen.

Tag der Prüfung: 16.09.2010

Vorwort

Die vorliegende Dissertation wurde an der Fakultät für Luft- und Raumfahrttechnik der Universität der Bundeswehr München angefertigt. Die Arbeit entstand während meiner wissenschaftlichen Mitarbeit am Institut für Thermodynamik und Tätigkeit am Institut für Technologie- und Innovationsmanagement.

Mein ganz besonderer Dank gebührt meinem Doktorvater Herrn Prof. Dr.-Ing. Christian Mundt für die Anvertrauung des Forschungsthemas, die stetige Förderung und die zahlreichen Anregungen, die wesentlich zum Gelingen dieser Arbeit beigetragen haben.

Mein Dank richtet sich gleichermaßen an Herrn Prof. Dr. rer. nat. Klaus Hornung für die Übernahme des Koreferats und die wertvollen fachlichen Anregungen. Für die Förderung der Promotion und die Übernahme des Kommissionsvorsitzes danke ich Herrn Prof. Dr.-Ing. Bernhard Katzy.

Bei meinen Diplomanden Daniel Neuschel, Oliver Otto, Oliver Weiand, Daniel Birgel und im Besonderen bei meinem Nachfolger Florian Göbel möchte ich mich für die wertvolle Unterstützung und die hervorragenden Beiträge ganz herzlich bedanken.

Mein Dank gilt Herrn Prof. Dr. rer. nat. Michael Pfitzner für die wertvollen Fachdiskussionen und Anregungen. Für die ausgezeichnete fachliche Betreuung im Hinblick auf den CFD Code NSMB möchte ich Herrn Jan Vos, CFS Engineering, Lausanne danken.
Für die mathematische Unterstützung bedanke ich mich bei Herrn Prof. Dr. Martin Frank, Rheinisch-Westfälische Technische Hochschule Aachen und Herrn Prof. Dr. Axel Klar, Technische Universität Kaiserslautern.

Meinen Dank aussprechen möchte ich allen Kolleginnen und Kollegen, die mich direkt oder indirekt während meiner Zeit an der Universität der Bundeswehr München und bei der Erstellung der Arbeit unterstützt haben. Die tolle Arbeitsatmosphäre beider Institute war sehr förderlich für das Gelingen der vorliegenden Arbeit. Insbesondere möchte ich Herrn Eike Tangermann und Herrn Roman Keppeler für ihre hilfreiche Unterstützung bezüglich der Hochleistungsrechneranlage danken. Frau Maria-Magdalena Poschner möchte ich ganz herzlich danken für die Unterstützung im Hinblick auf die ANSYS Anwendungen. Bei Herrn Bastian Thorwald und Herrn Daniel Kliche möchte ich mich für die anregenden Fachdiskussionen zu der numerischen Umsetzung bedanken.

Ganz herzlich danke ich Frau Ingrid Schramm für die administrative Unterstützung und Herrn Edgar Langguth als auch Herrn Hans-Jürgen Dolnik für die IT-Unterstützung.

Im Hinblick auf die Erstellung der Dissertation gilt mein Dank Frau Eva-Maria Walter für die gründliche Korrekturlesung und die hilfreichen Verbesserungsvorschläge.

Mein besonderer Dank gilt meinen Eltern und Freunden für die geduldige Unterstützung und den nötigen Rückhalt. Insbesondere möchte ich meiner Lebensgefährtin, Steffi, für das Verständnis und die moralische Unterstützung von ganzem Herzen danken.

München, im September 2010

Andreas Thellmann

Abstract

English

Modelling gas radiation within the numerical analysis of combustion processes and reacting high enthalpy flows respectively is often neglected due to the complex mathematics of the radiative transport equation, the lack of detailed information on the spectral properties of the radiatively participating gas and the strong increase of computation time. The challenge is to identify approximative models of the radiative transport equation, as well as suitable spectral approximations, which provide the best compromise between fastness and accuracy for the present problem.

This thesis investigates the impact of gas radiation on a turbulent, reacting flow in a rocket combustion chamber based on the main combustion chamber of the Space Shuttle Main Engine (SSME). Due to the high characteristic temperature ($\approx$3800 K) and pressure ($\approx$ 21 MPa) and presence of strong radiating species, gas radiation plays a significant role in the heat transfer analysis of rocket combustion chambers. To investigate the influence of the radiatively participating species, two different combustion systems are considered: hydrogen-oxygen (H_2-O_2) and methane-oxygen (CH_4-O_2). Within the first system only water vapour (H_2O) and in the second system both water vapour and carbon dioxide (CO_2) mainly contribute to the radiative heat transfer, via absorption and emission of radiation. Methane is currently under discussion for future rocket engines due to its advantages compared to hydrogen. It is expected that the contribution of gas radiation in hydrocarbon systems such as methane-oxygen increases.

The present study reveals that both combustion systems are optically thick; the hydrogen-oxygen system has an optical thickness of 17 and the methane-oxygen system has a value of 32. Due to the optical thick situation this study demonstrates that the Rosseland model can be applied for the approximation of the radiative transfer equation and delivers physical meaningful results. To take the operating conditions of the SSME main combustion chamber into account an semi-empirical jump-correlation for the solid wall boundary condition of the Rosseland approximation is introduced and a modified Rosseland formulation in conjunction with the weighted-sum-of-gray-gases (WSGG) approach for the spectral modelling is presented. This newly derived Rosseland approximation is then implemented into the NSMB research CFD code. The results of the NSMB Rosseland model are on the one hand compared with computations of the CFX and FLUENT commercial CFD solvers, using the radiative transport models “P_1-moment method” and “Discrete Transfer Method (DTM)” and on the other hand to benchmark calculations from literature.

The results reveal that gas radiation has a relatively small influence on the flow field within the SSME main combustion chamber. The thermal boundary layer is increased slightly due to gas radiation. The influence of the gas radiation on the axial temperature in the core flow and wall shear stress is neglectable. However gas radiation contributes significantly to the total wall heat flux. The results of CFX and FLUENT for the H_2-O_2 study reveal that nearly 7.7 % and for the CH_4-O_2 study nearly 8.8 % of the total wall heat flux is caused by gas radiation. The NSMB Rosseland case induces a gas radiation impact of 32 % for the H_2-O_2 study. Including gas radiation increases the computational costs significantly for all three CFD solvers compared to a calculation without radiation. The NSMB Rosseland combination increases the CPU time by approximately 22 %, CFX and P_1 by 51 % and CFX and DTM by 466 % compared to a calculation without gas radiation.

The NSMB Rosseland case overestimates the influence of gas radiation on the wall heat loads but it results in significantly lower CPU time costs. A further development of the Rosseland solid wall boundary condition could decrease the overestimation of the fraction of gas radiation. The lower CPU time costs of the Rosseland model may lead to a better acceptance of including gas radiation in engineering problems in the scope of numerical combustion analysis.

Deutsch

Die Modellierung der Gasstrahlung innerhalb der numerischen Analyse von Verbrennungsprozessen und reagierenden Strömungen mit hoher Enthalpie wird oft vernachlässigt aufgrund der komplexen Mathematik der Strahlungstransportgleichung sowie der komplizierten Beschreibung der spektralen Größen des strahlenden Gases und der starken Zuname der Rechenzeit. Die Herausforderung hierbei ist zum einen approximative Modelle der Strahlungstransportgleichung zu identifizieren und zum anderen geeignete spektrale Modellierungen zu verwenden, die einen optimalen Kompromiss darstellen zwischen Schnelligkeit und Genauigkeit für das aktuelle Problem.

Diese Arbeit untersucht den Einfluss der Gasstrahlung auf eine turbulente, reagierende Strömung in einer Raketenbrennkammer, basierend auf der Hauptbrennkammer des Space Shuttle Hauptantriebsystems (SSME). Aufgrund der hohen charakteristischen Temperatur (≈ 3800 K), des hohen Drucks (≈ 21 MPa) und der Einwirkung stark strahlender Spezies, spielt die Gasstrahlung eine entscheidende Rolle für die Analyse der Wärmeübertragung in Raketenbrennkammern. Um den Einfluss der strahlenden Spezies zu untersuchen, werden zwei verschiedene Verbrennungssysteme betrachtet: Wasserstoff-Sauerstoff (H_2-O_2) und Methan-Sauerstoff (CH_4-O_2). Innerhalb des ersten Systems trägt nur Wasserdampf (H_2O) und in dem zweiten System tragen sowohl Wasserdampf als auch Kohlenstoffdioxid (CO_2) hauptsächlich zu dem Strahlungstransfer, mittels Absorption und Emission, bei. Methan steht derzeit in der Diskussion im Hinblick auf zukünftige Raketenmotoren aufgrund seiner Vorteile gegenüber Wasserstoff. Es ist zu erwarten, dass der Beitrag der Gasstrahlung in Kohlenwasserstoffsystemen, wie beispielsweise Methan-Sauerstoff, zunimmt.

Die vorliegende Arbeit macht deutlich, dass beide Verbrennungssysteme als optisch dicht zu betrachten sind, wobei das Wasserstoff-Sauerstoff System eine optische Dicke von 17 und das Methan-Sauerstoff System einen Wert von 32 hat. Aufgrund des optisch dichten Zustandes demonstriert diese Arbeit, dass das Rosseland Modell für die Approximation der Strahlungstransportgleichung angewendet werden kann und physikalisch sinnvolle Ergebnisse liefert. Um den Betriebsbedingungen der SSME Hauptbrennkammer Rechnung zu tragen, wird eine semi-empirische Sprungkorrelation für die Wandrandbedingung der Rosseland Näherung eingeführt. Zudem wird eine modifizierte Rosseland Formulierung in Verknüpfung mit dem Ansatz, der Summe gewichteter grauer Gase (WSGG), für die spektrale Modellierung präsentiert. Diese neu hergeleitete Rosseland Approximation wird anschließend in den CFD Forschungscode NSMB implementiert. Die Ergebnisse des NSMB Rosseland Modells werden auf der einen Seite mit Rechnungen der kommerziellen Löser CFX und FLUENT verglichen, unter Verwendung der Strahlungstransportmodelle P_1-Momenten Methode und Diskrete Transfer Methode (DTM) und auf der anderen Seite erfolgt ein Vergleich mit Benchmark Rechnungen aus der Literatur.

Die Ergebnisse zeigen, dass Gasstrahlung einen relativ kleinen Einfluss auf das Strömungsfeld innerhalb der SSME Hauptbrennkammer besitzt. Die thermische Grenzschicht wird geringfügig dicker aufgrund der Gasstrahlung. Der Einfluss der Gasstrahlung auf die axiale Temperatur in der Hauptströmung und auf die Wandschubspannung ist vernachlässigbar. Auf der anderen Seite beeinflusst jedoch die Gasstrahlung signifikant den Gesamtwandwärmestrom. Die Ergebnisse von CFX und FLUENT für die H_2-O_2 Studie zeigen, dass näherungsweise ein Anteil von 7,7 % und für die CH_4-O_2 Studie ca. 8,8 % des Gesamtwandwärmestromes von der Gasstrahlung verursacht wird. Der NSMB Rosseland Fall induziert einen Einfluss der Gasstrahlung von 32 % für die H_2-O_2 Studie. Die Berücksichtigung der Gasstrahlung erhöht bei allen drei CFD Lösern die Rechenzeit signifikant, verglichen mit einer Rechnung ohne Strahlung. Die Kombination NSMB-Rosseland erhöht die CPU Zeit um näherungsweise 22 %, CFX-P_1 um 51 % und CFX-DTM um 466 %, verglichen mit einer Rechnung ohne Gasstrahlung.

Der NSMB Rosseland Fall überschätzt den Beitrag der Gasstrahlung auf die Wandwärmelasten, führt aber zu einer deutlichen Reduzierung der Rechenzeit. Eine Weiterentwicklung der Wandrandbedingung für das Rosseland Modell könnte die Überschätzung des Gasstrahlungseinflusses reduzieren. Die niedrigeren CPU Zeiten des Rosseland Modells könnten dazu führen dass die numerische Modellierung der Gasstrahlung in Ingenieursproblemstellungen eine breitere Akzeptanz erfährt.

Table of Contents

Nomenclature

Latin Symbols		**Unit**
a	Total absorption coefficient (TAC)	[1/m]
$a_{1,x}$	x-component of vector $\overrightarrow{a_1}$ in the plane ABCD	[m]
a_i	Absorption coefficient for the i-th gray gas	[1/m]
$a_{p,i}$	Pressure absorption coefficient for the i-th gray gas	[1/(m atm)]
a_{R}	Rosseland mean absorption coefficient	[1/m]
$a_{\mathrm{R,i}}$	Rosseland mean absorption coefficient of the first interior cell	[1/m]
$a_{\mathrm{R},\Delta\lambda}$	Rosseland mean absorption coefficient in wavelength interval $\Delta\lambda$	[1/m]
a_λ	Spectral absorption coefficient	[1/m]
$\vec{a}_1$	Vector in the plane ABCD	[m]
A_l^m	Position-dependent coefficients for P_N-method	[-]
$b_{i,j}$	Smith-WSGGM polynomial coefficients; i: i-th gray gas, j: order of polynomial	$[1/\mathrm{K}^{\mathrm{j-1}}]$
c	Speed of light in a medium	[m/s]
c_0	Speed of light in vacuum, $c_0 = 2.99792458 \cdot 10^8$ m/s	[m/s]
c_p	Mass-specific heat at constant pressure	[J/(kgK)]
c_{v}	Mass-specific heat at constant volume	[J/(kgK)]
C_1	Constant in Planck's spectral energy (or intensity) distribution, $C_1 = hc_0^2 = 0.59552137 \cdot 10^{-16}$ W m^2/sr	[W m^2/sr]
C_2	Constant in Planck's spectral energy (or intensity) distribution, $C_2 = hc_0 / k = 0.014387752$ m K	[m K]
C_{abs}	Absorption cross section	[m^2]
C_{sca}	Scattering cross section	[m^2]
d	Nozzle diameter	[m]
dA	Infinitesimal surface	[m^2]
dA_{p}	Projected area of dA normal to an infinitesimal pencil of rays	[m^2]
dA_{S}	Projected area of dA normal to an infinitesimal pencil of rays	[m^2]
dS	Infinitesimal surface (boundary) element of an arbitrary volume V	[m^2]
dV	Infinitesimal volume element	[m^3]
$d\kappa_\lambda$	Spectral optical differential thickness	[-]
$d\omega$	Infinitesimal solid angle	[sr]
D	Diameter of atom or molecule	[m]
D	Path length	[m]
e	Mass-specific internal energy	[J/kg]
e_{b}	Blackbody total hemispherical emissive power	[W/m^2]
$e_{\Delta\lambda\mathrm{b}}$	Blackbody hemispherical emissive power in wavelength interval $\Delta\lambda$	[W/m^2]

$e_{\lambda\mathrm{b}}$	Blackbody spectral hemispherical emissive power = Planck's spectral distribution of emissive power	[W/(m$^2\mu$m)]
$\vec{e}_x$	Unit normal vector in x-direction	[-]
E	Mass-specific total energy, $E = e + \frac{1}{2}(u^2 + v^2 + w^2)$	[J/kg]
$\vec{f}$	Heat flux vector in x-direction	[W/m^2]
$\vec{g}$	Heat flux vector in y-direction	[W/m^2]
G_λ	Spectral incident radiation = direction-integrated intensity	[W/(m$^2\mu$m)]
h	Planck's constant, $h = 6.62606876 \cdot 10^{-34}$ J s	[J s]
$\vec{h}$	Heat flux vector in z-direction	[W/m^2]
h_g	Heat-transfer coefficient	[W/(m^2 K)]
$\Delta_\mathrm{R} H$	Reaction Enthalpy	[J]
i	Index in I-direction for addressing cell i, j, k	[-]
i	Index in summation of gray gases	[-]
i_b	Blackbody total radiation intensity	[W/(m^2 sr)]
i_λ	Spectral radiation intensity	[W/(m$^2\mu$m sr)]
$i_{\lambda b}$	Blackbody spectral radiation intensity	[W/(m$^2\mu$m sr)]
$\bar{i}_{\lambda,0}$	Spectral incident radiation or zeroth moment	[W/(m$^2\mu$m)]
$\bar{i}_{\lambda,i}$	Spectral radiation heat flux in the i-direction	[W/(m$^2\mu$m)]
$\bar{i}_{\lambda,ij}$	Spectral radiation pressure tensor, with $i \times j$-equations (moments)	[W/(m$^2\mu$m)]
I	Direction of I, J, K-coordinate system	[-]
I	Number of increments	[-]
j	Index in J-direction for addressing cell i, j, k	[-]
j	Exponent for normalized spherical harmonics, $j = \sqrt{-1}$	[-]
J	Direction of I, J, K-coordinate system	[-]
J	Number of increments	[-]
k	Index in K-direction for addressing cell i, j, k	[-]
k	Index for the k-th radiating species in a gas mixture	[-]
k	Boltzmann's constant, $k = 1.3806503 \cdot 10^{-23}$ J/K	[J/K]
k_cd	Thermal heat conductivity	[W/(mK)]
$k_\mathrm{cd,i}$	Thermal heat conductivity for the first interior cell	[W/(mK)]
k_R	Rosseland radiative heat conductivity	[W/(mK)]
K	Direction of I, J, K-coordinate system	[-]
K	Number of increments	[-]
l	Characteristic length	[m]
l	Order of the P$_N$-method, e.g. $l = 3$ corresponds to P$_3$-method	[-]
l_i	Direction cosines for rectangular coordinate system, x_1, x_2, x_3	[-]
l_j	Direction cosines for rectangular coordinate system, x_1, x_2, x_3	[-]
m	Index for series of orthogonal harmonic functions	[-]
m	Index for the summation of $\Delta\lambda_m$ wavelength intervals	[-]

$\dot{m}$	Mass flow rate	[kg/s]
M	Number of increments	[-]
Ma	Mach number	[-]
n	Refractive index; $n = c_0 / c \approx 1$ for ordinary gas mixtures	[-]
n	Coordinate in normal direction of a solid wall	[m]
n	Time step or number of iterations	[-]
$\vec{n}$	Unit surface normal vector	[-]
N	Conduction-radiation parameter	[-]
N	Number of selected terms for the P_N-method	[-]
Nu	Nusselt number	[-]
p	Static pressure	[Pa ≡ N/m²]
	In connection with WSGGM the unit atm is used (1 atm = 101325 Pa).	[atm]
p_k	Partial pressure of the radiating species k	[Pa ≡ N/m²]
$P_l^{\|m\|}$	Associated Legendre polynomials	[-]
Pr	Prandtl number, air-laminar case: $\mathrm{Pr} = 0.72$, for air-turbulent case: $0.78 \le \mathrm{Pr} \le 0.9$	[-]
q_{cd}	Heat flux due to conduction (Fourier's law)	[W/m²]
q_{conv}	Heat flux due to convection	[W/m²]
$q_{i-1/2,j,k}$	Radiative heat flux in I-direction through the cell side ABCD	[W]
q_{r}	Heat flux due to radiative heat transfer	[W/m²]
q_{rg}	Net radiative flux from Rosseland diffusion approximation	[W/m²]
q_{rw}	Radiative heat flux due to jump condition, to relate q_{rg} to the user imposed solid wall boundary condition	[W/m²]
$q_{\mathrm{r},x}$	Radiation heat flux in x-direction	[W/m²]
$q_{\mathrm{r},\lambda,x}$	Spectral radiation heat flux in x-direction	[W/(m$^2\mu$m)]
$\vec{q}_{\mathrm{r},\lambda}$	Spectral heat flux vector due to radiation	[W/(m$^2\mu$m)]
q_{TWHF}	Total wall heat flux	[W/m²]
Q_{abs}	Absorption efficiency factor	[-]
Q_{ext}	Extinction efficiency factor	[-]
Q_{sca}	Scattering efficiency factor	[-]
$Q_{i,j,k}$	Net heat flux leaving and entering the grid cell i,j,k	[W]
r_{w}	Radius of the combustion chamber	[m]
$\vec{r}$	Position vector, $\vec{r}^{\,T} = (x,y,z)$ or $\vec{r}^{\,T} = (x_1,x_2,x_3)$	[m]
R	Mass-specific gas constant, for air: $R = 287$ J/(kgK)	[J/(kgK)]
Re	Reynolds number	[-]
Re_d	Reynolds number related to nozzle diameter d	[-]
sr	Steradian, unit for solid angle ω	[m^2/m^2]
$\vec{s}$	Unit direction vector, $\vec{s} = \vec{s}(\theta,\varphi)$	[-]
$\vec{s_i}$	Incident unit direction vector, $\vec{s_i} = \vec{s_i}(\theta,\varphi)$	[-]
S	Geometric path of radiation travelling or path length	[m]

S_0	Specific point of path of radiation travelling	[m]
S'	Dummy variable of integration for geometric path length	[m]
$\tilde{S}$	Mean penetration distance of a photon	[m]
$\underline{\underline{S}}$	Surface normal tensor, with 9 components	$[\mathrm{m}^2]$
$\vec{S}^I$	Surface normal vector in I-direction, with 3 components	$[\mathrm{m}^2]$
$\vec{S}^I_{\mathrm{ABCD}}$	Surface normal vector in I-direction at surface ABCD	$[\mathrm{m}^2]$
S^I_x	Element of surface normal vector $\vec{S}^I$ in x-direction	$[\mathrm{m}^2]$
S_c	Sutherland's constant, for air: $S = 110.4$ $(100\ \mathrm{K} \leq T \leq 1900\ \mathrm{K})$	[-]
t	Time	[s]
$t_{i,j,k}$	Local time step of a single grid cell i,j,k	[s]
T	Static temperature	[K]
T_i	Temperature of the first interior finite volume grid cell	[K]
T_ju	Jump temperature and boundary condition for Rosseland radiative flux	[K]
T_w	User imposed solid wall temperature	[K]
u	Cartesian velocity component in x-direction	[m/s]
u_λ	Spectral radiative energy density	$[\mathrm{J}/(\mathrm{m}^3 \mu\mathrm{m})]$
v	Cartesian velocity component in y-direction	[m/s]
V	Arbitrary volume	$[\mathrm{m}^3]$
$V_{i,j,k}$	Discrete volume of a single grid cell i,j,k	$[\mathrm{m}^3]$
$\vec{V}$	Vector of Cartesian velocities, $\vec{V}^T = (u,v,w)$	[m/s]
w	Cartesian velocity component in z-direction	[m/s]
w_i	Weighting factor for the i-th gray gas	[-]
$\vec{W}$	State vector or solution vector of the conservative variables	$[\mathrm{J}/\mathrm{m}^3]$
W	Component of the solution vector $\vec{W}$	$[\mathrm{J}/\mathrm{m}^3]$
x	Cartesian coordinate	[m]
$\bar{x}$	Transformed axial distance	[m]
x_1	Cartesian coordinate	[m]
x_2	Cartesian coordinate	[m]
x_3	Cartesian coordinate	[m]
x_i	Cartesian coordinate, with $i = 1,2,3$	[m]
$x_{i,j,k}$	Cartesian x-coordinate at the discrete location i,j,k	[m]
X_k	Molar fraction of the radiating species k	[-]
y	Cartesian coordinate	[m]
y^+_ave	Average, dimensionless distance from first interior node to solid wall	[-]
Y^m_l	Normalized spherical harmonics for P_N-method	[-]
z	Cartesian coordinate	[m]

Greek Symbols

γ	Ratio of specific heats, for air at room temperature, $\gamma = 7/5 = 1.4$	[-]
γ	Angle for direction cosines	[rad]
δ	Angle for direction cosines	[rad]
δ	Kronecker delta	[-]
δ_th	Thickness of the thermal boundary layer	[m]
$\Delta \mathrm{gw}$	Radiation mean free path for calculation of jump temperature	[m]
$\Delta\lambda_m$	Infinitesimal wavelength interval with index m	[m]
Δn	Distance first interior node to wall = half width of first interior cell	[m]
∂V	Boundary of an arbitrary volume	[m^2]
ε	Convergence parameter	[-]
ε_g	Total emissivity of a real gas	[-]
ε_w	Emissivity of a solid wall	[-]
θ	Polar or cone angle measured from normal of surface	[rad]
θ	Angle for direction cosines	[rad]
κ	Total optical thickness (TOT), $\kappa = \int_0^\infty \int_0^S a_\lambda(S')\, dS'\, d\lambda$	[-]
κ_D	Total optical thickness for path length D, $\kappa_D = a\, D$	[-]
κ_λ	Spectral optical thickness, $\kappa_\lambda = \int_0^S a_\lambda(S')\, dS'$	[-]
λ	Wavelength	[m]
λ_0	Wavelength in vacuum	[m]
λ_m	Wavelength interval with index m	[m]
λ_m	Wavelength in a medium other than vacuum	[m]
μ	Dynamic viscosity	[Pa s]
μ	Direction cosine, i.e. $\mu = \cos\theta$	[-]
μ_{ref}	Dynamic viscosity at the reference temperature T_{ref}, for air: $\mu_{ref} = 17.5 \cdot 10^{-6}$ [Pa s] at $T_{ref} = 280$ K	[Pa s]
π	Mathematical constant, $\pi = 3.14159$, for a circle with diameter 1, its circumference is π	[-]
ξ	Characteristic size parameter of $\xi = \pi D / \lambda$	[-]
ρ	Gas density	[kg/m^3]
σ	Stefan-Boltzmann constant, $\sigma = 5.670400 \cdot 10^{-8}$ W/(m^2 K^4)	[W/(m^2 K^4)]
$\sigma_{s\lambda}$	Spectral scattering coefficient	[1/m]
$\underline{\underline{\tau}}$	Viscous stress tensor	[N/m^2]
τ_{xx}	Normal stress component of the viscous stress tensor	[N/m^2]
τ_{xy}	Shear stress component of the viscous stress tensor	[N/m^2]
φ	Azimuthal or circumferential angle	[rad]
Φ_λ	Spectral scattering phase function	[-]
ψ	Jump coefficient for Rosseland Radiation Model	[-]
ψ_eff	Effective jump coefficient for Rosseland Radiation Model	[-]
ψ_User	Heuristic effective jump coefficient for Rosseland Radiation Model	[-]

Ψ	Component of the viscous stress tensor	[W/m²]
ω	Solid angle	[sr]
ω_i	Incident solid angle	[sr]

Subscripts

cd	Heat conduction according to Fourier's law
cv	Heat convection
i	Index in I -direction for addressing cell i,j,k
i	Incoming; incident; inner
j	Index in J -direction for addressing cell i,j,k
k	Index in K -direction for addressing cell i,j,k
vi	Viscous Quantity
x	Quantity which changes in x -direction
y	Quantity which changes in y -direction
z	Quantity which changes in z -direction
λ	Wavelength (spectrally) dependent
$\Delta\lambda$	For a wavelength band $\Delta\lambda$

Superscripts

n	Time step or number of iterations

Abbreviations and Acronyms

CFD	Computational Fluid Dynamics
CFL	Courant-Friedrichs-Levy
CPU	Central Processing Unit
DOM	Radiative transport: Discrete Ordinates Method
DTM	Radiative transport: Discrete Transfer Method
EBCOW	Excel Based Comparison of WSGG models
FORTRAN	Formula Translation
$k-\varepsilon$	Turbulence model
LES	Large-Eddy Simulation
LRE	Liquid Rocket Engine
LTE	Local Thermodynamic Equilibrium
MTIG	Mixture of Thermal Ideal Gases
NASA	National Aeronautics and Space Administration
P_1	Radiative transport model, based on the moment method
PDF	Probability Density Function
RANS	Reynolds-Averaged-Navier-Stokes (equations)
RRM	Radiative transport: Rosseland Radiation Model
RTE	Radiative Transfer Equation
RWHF	Radiative Wall Heat Flux
SSME	Space Shuttle Main Engine
SSOR	Symmetric Successive Over Relaxation
SST	Turbulence model: Menter's Shear Stress Transport version of the $k-\omega$ model
TAC	Total Absorption Coefficient

TRI	Turbulence-radiation interactions
TWHF	Total Wall Heat Flux
WSGGM	Weighted Sum of Gray Gases Model

Further symbols and conventions

da	Infinitesimal quantity a
δ_{ij}	Kronecker delta, with $\delta_{ij} = 1$ for $i = j$ and $\delta_{ij} = 0$ for $i \neq j$
$O(n)$	Order of magnitude of n
$\vec{V}$	Vector
$\vec{V}^{T}$	Transposition of vector $\vec{V}$
$\mathbf{M}$	Matrix
$\underline{\underline{T}}$	Tensor
$\vec{\nabla}$	Nabla operator in Cartesian coordinates: $\vec{\nabla} = \frac{\partial}{\partial x}\vec{i} + \frac{\partial}{\partial y}\vec{j} + \frac{\partial}{\partial z}\vec{k}$, with Cartesian unit vectors $\vec{i}, \vec{j}, \vec{k}$
$grad$	Gradient of a scalar variable ($grad\ T = \vec{\nabla} T$)
div	Divergence of a vector variable ($div\ \vec{V} = \vec{\nabla} \cdot \vec{V}$)
rot	Rotation of a vector variable ($rot\ \vec{V} = \vec{\nabla} \times \vec{V}$)
∂_{x_i}	$= \frac{\partial}{\partial x_i}, i = 1, 2, 3$

1 Introduction

1.1 Background and Motivation

The focus of this thesis is the investigation of the impact of thermal radiation on the overall heat transfer balance in a rocket combustion chamber. Thermal radiation is sometimes also termed as radiative heat transfer, describing the heat transfer caused by electromagnetic waves. Thermal radiation is subdivided into radiative heat exchange between solid surfaces surrounded by a transparent medium and into energy transfer through translucent media. A translucent medium can absorb, emit and scatter radiation. For a gaseous medium the term “gas radiation” is commonly used and described in detail in the text books by Pai [1] and Penner & Olfe [2]. Some important applications of gas radiation are hot gas furnaces, engine combustion chambers at high pressures, rocket propulsion engines and hypersonic shock layers. In this thesis the main combustion chamber of the Space Shuttle Main Engine (SSME) is considered as practical engineering problem.

Thermal radiation differs from the other two modes of heat transfer, i.e. heat conduction and convection. For both mechanisms, energy transfer between two locations depends on their temperature difference to approximately the first power. Considering conduction in gases and liquids, energy is transferred from molecule to molecule due to a huge number of microscopic collisions. Heat transfer by convection, on the other hand, is dominated by the motion of the molecules. Many of the molecules with a specific kinetic energy move along their path and transfer energy from one location to another. Hence, both conduction and convection require the presence of a medium for heat transfer. However, thermal radiation is transferred by photons and depends on the difference of the fourth power of the temperature between two locations. From this basic difference between radiation and convection, respectively heat conduction, it is evident that the importance of radiation is intensified at high temperatures. A basic introduction into thermal radiation is provided in the text books by Hottel & Sarofim [3], Modest [4] and Siegel & Howell [5].

The modelling of radiation is often neglected in combustion analysis, mainly because it involves complex mathematics which increase computation time and also because of the lack of detailed information on the optical properties of the participating gas. Thermal radiation in hot-gas flows can be an important mode of heat transfer even when scattering is neglected. Ignoring radiative transfer may introduce significant errors in overall predictions [6].

A second important field in which radiation plays a significant role pertains to the re-entry of a space vehicle into an atmosphere [7-10]. At hypersonic velocities, shock waves are created in front of the spacecraft, resulting in large pressures, extremely high temperatures (≈ 20000 K), and dissociation of involved molecules. For instance, gas radiation during re-entry into the Earth’s atmosphere can have a considerable impact on the heat transfer for re-entry velocities exceeding the Earth's parabolic velocity (≈ 11 km/s) [2].

With regard to the discipline of rocket propulsion systems, Sutton & Biblarz state in [11] that between the first space launch in 1957 until the end of 1998 approximately 4102 space launch attempts have taken place in the world, of which approximately 129 failed. Two missions, the Delta flight 269 in 1999 [12] and the Ariane 5 flight 157 in 2002 [13], for example failed due to the malfunction of the rocket combustion chamber. Haarmann [14] points out that it is essential to define the thermal loads on the chamber wall material as accurately as possible to avoid a failure of the rocket chamber. For the accurate prediction of total heat transfers it is important to include the contribution of radiation. The study of the radiative heat transfer for liquid rocket engines gained importance with the development of large-scale, high pressure rocket engines. Sutton & Biblarz [11] point out that radiative heat transfer is especially important for liquid rocket combustion chambers with a large gas volume. Furthermore, they asserts that heat conduction can be neglected compared to convection which is the main transport mechanism in the rocket combustion chamber. Additionally, they mention that the contribution of radiation to the overall transferred heat can range from 5 % to 35 %. In the field of rockets, one of the first examples of the importance of thermal radiation is the base heating from the exhaust plume which was observed during the development of the Saturn V rockets in the late 1950s [15]. It was demonstrated that radiative heat transfer was one of the two main energy transport modes involved. The same base-heating mechanism was studied with respect to the space shuttle's first and second stages some 20 years later [16].

For a long time it had been assumed that thermal radiation in combustion chambers and nozzles does not play a significant role regarding liquid hydrogen-oxygen (LH_2-LO_2) engines with the main heat transfer to the walls effected via convection [17]. However, with respect to hydrogen scramjet combustors Nelson [18] showed that radiative heating represents roughly 10 % of convective heating, and Liu & Tiwari [19] found that radiative effects on the wall heat transfer might be significant in chemically reacting hydrogen nozzle flows. With regard to the LH_2-LO_2 SSME main combustion chamber Naraghi et al. [20] establish that the radiative heat flux can reach 10 % of the total wall heat flux and Wang [21] states a radiation influence of 5 % for the same system. There are attempts to reduce the wall heat loads in rocket engines by cooling the wall with a film of an inert and radiatively transparent fluid, isolating the chamber wall and the hot combustion gas. In this context it should be noted that film cooling by a nearly transparent film may only reduce the convective wall heat flux but not the radiative heat flux, leading to a higher radiation-convection ratio with respect to the wall heat flux [17].

Currently, research is underway in order to use methane (CH_4) instead of hydrogen (H_2) in rocket engines and scramjets. NASA and partners [22; 23], see Fig. 1, DLR and partners [24-27] and several other small research groups [28] are involved in the investigation of new rocket combustion chambers. Methane offers superior properties concerning coking and soot deposition in contrast to hydrocarbon fuels (e.g. kerosene) and delivers a slightly higher specific impulse compared to kerosene [29]. Compared to liquid hydrogen (LH_2, liquid at 20 K) the storage of liquid methane (LCH_4) is easier due to the higher condensation temperature of 110 K which is close to liquid oxygen (LO_2, liquid at 90 K). This fact results in similar cooling units for fuel and oxidizers and less mass for the isolation of the liquid fuel. In addition, methane has a higher density compared to hydrogen, hence it requires less mass for storage which in turn reduces the take-off weight and increases the payload capacity of the launch vehicle.

Figure 1: Hot-firing test of XR-5M15 at Mojave Air and Space Port, from [23]

Methane could also be interesting for future outer space missions as it can be manufactured on Mars or even collected from the “methane-lakes” on Saturn’s moon Titan [30]. Replacing the conventional fuel LH_2 by LCH_4 will result in a redesign of the prediction of the thermal loads in the rocket chamber. With regard to LH_2-LO_2 systems, only water vapour (H_2O) contributes significantly to radiation as it is known as a “strong radiator”. In the case of LCH_4-LO_2 combustion not only H_2O but also carbon dioxide (CO_2) is produced which radiates even stronger as opposed to water vapour. Hence, replacing hydrogen by methane increases the influence of radiation on the overall heat transfer. In [20] it is concluded that the amount of radiative to total wall heat flux reaches 30 % for a kerosene-operated rocket engine.

Hydrocarbon fuels are not only of interest for rocket engines but also for scramjet propulsion systems. The X-51A program [31], see Fig. 2, is the world's first investigation of a hypersonic Mach 6+ free-flying vehicle with a hydrocarbon fuel scramjet engine instead of a hydrogen operated engine [32]. Using hydrocarbon fuels instead of hydrogen enables the use of much smaller fuel storage tanks due to the higher density of hydrocarbons, resulting in an increased payload capacity. The JP-7 liquid fuel is used to cool the chamber walls of the scramjet engine and hence prevents only convective heating but not radiative heating. Currently, no publications are known on the investigation of the influence of radiation on the heat loads on the chamber walls of scramjet engines with regard to hydrocarbon fuels.

The facts mentioned above underline the significance of radiative heat transfer in different disciplines of aerospace and provide the motivation of this thesis to investigate the influence of radiation on the flow dynamics for both LH_2-LO_2 and LCH_4-LO_2 systems.

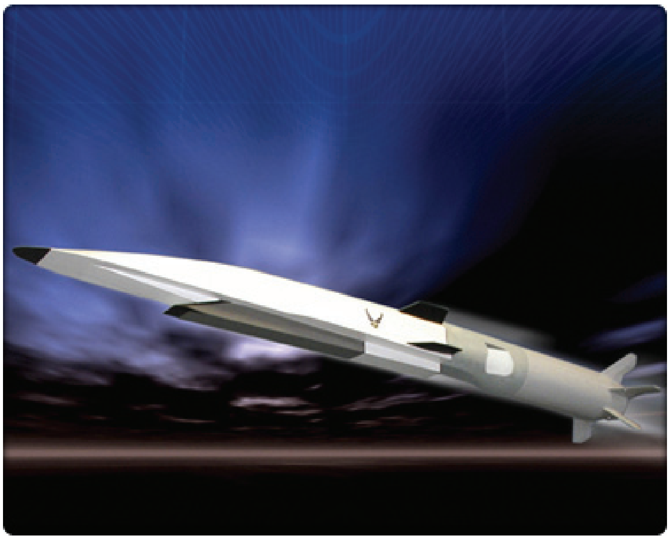

Figure 2: X-51 WaveRider, free-flying hypersonic vehicle, from [31]

1.2 Current State of Research

This subchapter gives a short overview of the work done on the modelling of radiative heat transfer in gases and the coupling of gas radiation and fluid dynamics. A general review of literature until 2002 can be found in [5] and until 2003 in [4].

A multitude of publications is available investigating the combined heat transfer of convection, conduction and radiation, for instance in [33-37]. Considering the governing equation of energy for the heat transfer in fluids, convection-dominated problems tend to be of a hyperbolic nature in the main flow in terms of physical space but have high normal gradients near solid walls, necessitating a very fine near-wall mesh. Similar to heat conduction, radiation problems tend to be of an elliptic nature and are further complicated by a directional and spectral dependency on radiative intensity. In nearly all practical cases, convection, conduction and radiation are coupled only via the energy equation of the corresponding set of governing equations. Bataller [38] investigates a laminar, viscous flow over a flat plate and finds that radiation influences the work due to deformation and heat transfer. Hence, even in the absence of chemical reactions the interaction of radiation and hydrodynamics can be observed.

The results of the research group under the leadership of Klar and Pinnau can be found in the SFB 568 report [39] (funded by the DFG - German Research Foundation) which issues the investigation of fast methods for the solution of the radiative transfer equation (RTE) and the coupling of radiation and fluid dynamics in gas turbine combustion chambers. They conclude that the M_1-model, also called the maximum entropy closure radiation model, offers a good compromise in accuracy vs. speed compared to a diffusive and detailed approximation of the RTE, respectively. Furthermore, they discovered that the coupling between radiation and a low Mach number inert flow is weak, while the coupling of radiation and chemistry can be significant. In connection with [39], Teleaga et al. [40] investigate the interaction between radiation and a low Mach number flow for a fire in a tunnel. The fire is represented by a heat source, hence chemistry is not modelled. The convective heat transfer is influenced significantly by the radiative heat transfer only if the radiating heat source is large enough. Dubroca et al. [41]

include chemical reactions and investigate the coupling to radiation for a low Mach number, two-dimensional diffusion methane-air flame. They apply the M_1-model for the radiative transport modelling and a non-gray spectral formulation, indicating that the M_1-model covers the entire optical range, i.e. optical thin and thick characteristics of the radiatively participating media. They demonstrate that both temperature distribution and the velocity field are affected by the presence of radiation and point out that 21 % additional CPU time are required if radiation is included. Turbulence-radiation interactions (TRI) are not taken into account.

Combining high-level models for turbulence and radiation requires great care to avoid instabilities, lack of convergence and/or exorbitant computer memory and CPU requirements [4]. A good overview of turbulence-radiation interactions is given in the PhD thesis of Mazumder [42] and Li [43]. For a long time, radiation and turbulence have been treated as independent phenomena, i.e. the influence of turbulent fluctuations on composition variables has been neglected. Experimental data obtained by the research groups headed by Faeth et al. [44] indicate that, depending on fuel and other conditions, radiative emissions from a flame may be as much as 50 % to 300 % higher than would be expected based on mean values of temperature and absorption coefficients. Mazumder & Modest [45] studied a nonreacting combustion gas mixture using a Monte Carlo Method for the radiative transport and found out that TRI are never of great importance in nonreacting flows, never changing radiative fluxes by more than 10 %. On the other hand, with regard to a methane-air diffusion flame using the Probability Density Function (PDF) for chemistry modelling, the heat loss of the flame increases up to 75 % beyond the temperature self-correlation due to TRI [46]. Li & Modest [47] systematically investigate the effects of TRI on nonluminous jet diffusion flames for the radiating species CO_2, H_2O and CH_4, with soot being neglected. They discovered that TRI affect the flame in two ways: first, emissions from and self-absorption by the flame are both increased significantly and approximately equally, and secondly, the additional net heat loss causes the flame to cool. This can in turn substantially lower emissions as well as chemical reaction rates. Modest indicates in [4] a discrepancy between the fact that Faeth et al. [44] conclude that TRI effects are significant for sooting flames, while Mazumder [42] suggests that TRI can be neglected when soot is modelled. Gupta et al. [48] perform a Large-Eddy Simulation (LES) for a two-dimensional turbulent, chemically reacting flow, showing that in the absence of chemical reactions radiation significantly modifies the mean temperature profiles but temperature fluctuations and turbulence-radiation interactions (TRI) are small. Chemical reactions enhance the composition and temperature fluctuations and hence the influence of TRI.

In addition to radiation interactions with chemically reacting turbulent flows, gas radiation also plays a significant role in the field of re-entry and general aeroheating problems. During re-entry into an atmosphere, shocks are generated in front of the spacecraft, resulting in extremely high temperatures, which causes the shock gas layer to emit and slightly absorb radiation. Furthermore, the gas between the shock and the forebody is also radiatively participative due to the still high temperatures and the activation of radiating species. A good overview is provided by the PhD thesis of Hartung [7] who describes the coupling of a nonequilibrium radiation code to a thermochemical nonequilibrium CFD flow solver of NASA. He shows that the radiative heat flux of the implemented P_l-method is 20 % to 25 % lower compared to the often used one-dimensional tangent slab method. Matsuyama et al. [49] investigate the interaction of radiation, turbulence and ablation reactions in the near wall region for a fully-coupled radiative gas dynamic problem in thermochemical equilibrium. They determine that although the temperature in the near wall region of the forebody is increased due to a larger eddy viscosity, this results in a weaker absorption of radiation because the mass fraction of the ablation product in the gas is reduced. Wright et al. [50] investigate a Titan aerocapture aeroheating problem which is characterized by an optically thin shock layer and dominated by strong radiative heating. They find that the radiative heat flux (119 W/cm²) in the stagnation point is 6 times higher compared to the convective flux (18.7 W/cm²). The flowfield is simulated in three dimensions, fully-coupled to the NEQAIR [51] radiation transport code which computes the emission, absorption, and transport of radiation line by line using a one-dimensional tangent-slab approximation. Additionally, a more accurate view-factor-based approach is used for computing radiative heating. Based on former results it was detected that the tangent-slab approximation overestimates the radiative wall heat transfer about 25 % in the stagnation region when compared to the view-factor method. It is concluded that the post-shock vibroelectronic temperature decreases approximately 10 % (from 8300 K to 7450 K). Removing energy from the hot-gas flowfield of the luvside due to radiation causes the shock to move 17 % (from 29 cm to 24 cm) closer to the body. Capra [10] experimentally investigates in her PhD thesis according to [50] the same configuration as a subscale model in an expansion tube. Capra concludes that the stagnation radiative heat flux is about 40 W/cm², hence 3 times smaller compared to the numerical prediction in [50]. She argues that the deviation partly results from the overprediction of the numerical study and the uncertainty considering the scaling of the measured subscale model with regard to the real configuration.

In contrast to [50], Feldick et al. [52] investigate turbulence-radiation interactions using large-eddy simulations (LES) on transmissivities in hypersonic turbulent boundary layers for the re-entry of Orion CEV in the Earth's atmosphere. The LES in conjunction with a modified line-by-line radiative transport equation solver show that the effects of absorption turbulence-radiation interactions due to radiation emitted in the shock layer are minimal, although a slight decrease of boundary layer transmissivities is predicted.

In addition to the external aeroheating problems, radiation is also important for internal flows in rocket engines and scramjets. The following overview concentrates on rocket combustion chambers; as indicated by Nelson [18], however, it shows that radiation can significantly influence convective heating, even with regard to hydrogen scramjets.

Several numerical investigations of radiation heat transfer in liquid rocket engines (LREs) are performed by Badinand [17], Byun [53], Liu [19], Naraghi [20; 54-57] and Wang [21] and their co-authors.

Badinand & Fransson [17] study the importance of thermal radiation in film-cooled LH_2-LO_2 rocket engine thrust chambers using the finite volume method (FVM) based on the discrete ordinate method (DOM) for modelling radiative transport. The spectral properties of the gases are modelled with the spectral-line weighted-sum-of-gray-gases model (SLWSGGM) by Denison & Webb [58]. Badinand & Fransson [17] conclude that film-cooling only prevents the convective heating of the hot gases; absorption of radiative energy, however, can be neglected due to the transparent properties of the film and the thin film layer. With regard to the design of more powerful combustion chambers with higher temperatures and pressures, radiation should thus be included in the analysis of life prediction in case of reusability. Regarding shocked nozzles in [17] it is established that radiation increases the wall temperature in the vicinity of the separation region by approximately 30 % and that radiation influences the position of the occurring shocks. These results underline that radiation may play a significant role in the heat load prediction of the wall material, even with regard to nonhydrocarbon fuels and even if scattering is neglected.

Byun & Baek [53] use the discrete ordinate method similar to [17] in conjunction with the WSGG approach; however, in contrast to [17] they investigate liquid kerosene-oxygen combustion including scattering by soot. They find that the high temperature zone decreases due to the energy loss caused by radiation. In summary, they state that the accurate modelling of the soot production is still a challenging problem however, it is crucial for the calculation of the scattering coefficient.

The Space Shuttle Main Engine (SSME) is a well investigated rocket engine. To demonstrate the influence of gas radiation on the overall energy transfer the SSME main combustion chamber is identified and used as a validation case in this thesis. Experimental data for the total wall heat flux of the SSME main combustion chamber are not available [59] and therefore the numerical studies by Naraghi et al. [20] and Wang [21] are often used as benchmark data. Naraghi and Wang independently simulated the SSME main combustion chamber and come to the conclusion that gas radiation can increase the total wall heat flux by 10 % on average.

1.3 Work Objectives

The main objective of this thesis is to numerically investigate the impact of gas radiation in a liquid rocket combustion chamber on the fluid dynamics and wall heat loads. Therefore, for the gas radiation suitable approximations needs to be identified and applied to a real rocket combustion chamber, which is additionally used as validation case.

Furthermore, two areas of the radiative heat transfer needs a detailed investigation: approximation of the radiative transport and spectral modelling of the radiative quantities. Thus, a detailed literature survey is necessary to identify suitable radiative transport approximations with a good compromise between fastness and accuracy. In addition, a detailed literature survey is necessary to identify suitable spectral approximations, which are well qualified for the use in rocket combustion chambers. Most of the spectral models are valid for atmospheric conditions only; hence sophisticated spectral models are required for high operating pressures and temperatures.

An accurate knowledge of the heat loads in rocket combustion chambers is crucial for the design of vital systems, such as cooling of the chamber walls. Underestimation of the total wall heat flux leads to fatal disintegration whereas overestimation may decrease the performance of the rocket engine. In CFD studies of combustion chambers radiation modelling is often neglected or only surface to surface radiation is considered, assuming a transparent gas between the chamber walls. In reality the combusted gas is radiatively participating, i.e. absorbs, emits and scatters radiation; and the gas radiation influences the flow dynamics and the heat loads of the wall.

Up to date, radiation and flow dynamics are often coupled weak, respectively segregated and often investigated for two-dimensional problems only. Thus, the aim is to study the interaction between gas radiation and flow hydrodynamics, applying the three-dimensional method of Computational Fluid Dynamics (CFD).

Heat transfer in a rocket combustion chamber in axial direction is dominated by convection and induces downstream a strong energy transport. The energy transfer upstream due to heat conduction can be neglected. In this context it should be investigated which impact heat transfer due to gas radiation has to the flow field in upstream direction.

The characteristic optical properties in a typical hydrogen-oxygen rocket combustion chamber indicate that the optical thickness of the combusted gas mixture is high enough to allow the use of a diffusive approximation of the radiative transfer equation. In this context the Rosseland diffusion approximation could fulfil the physical and numerical requirements. Due to its diffusive characteristics it can be easily implemented into an existing CFD solver and represents the fastest available approximation method for the radiative transfer equation. Based on the SFB 568 report [39] the intention is to use a model with low CPU time costs, and combining it with a sophisticated spectral model.

First attempts with the commercial ANSYS CFX code revealed that the Rosseland model delivers significant unphysical results. With respect to this observation a detailed investigation of the jump boundary condition is necessary, and the Rosseland approximation should be modified and implemented into the NSMB research CFD code, to empirically identify a more realistic Rosseland boundary condition for the coupling between radiation and flow hydrodynamics; particularly for a strong convection dominated flow.

Considering the optical properties, the characteristic gas radiation is strong connected with the radiating species of the combusted gas mixture. Thus, the influence of the fuel on the gas radiation needs to be investigated. Methane is currently under discussion for future rocket engines due to its advantages compared to hydrogen. Hence, it should be investigated if methane increases the impact of gas radiation compared to hydrogen.

In addition, it was observed that simulating a rocket combustion chamber with the ANSYS CFX and FLUENT CFD codes, revealed a different distribution of the total wall heat flux when scalable wall functions are used in the scope of the turbulence modelling. In this context it is necessary to further investigate the influence of different wall resolutions, turbulence models and CFD codes (structured vs. unstructured) on the near-wall quantities, as the predictive determination of the total wall heat flux is essential for the design of the wall-cooling.

1.4 Approach

To achieve the objectives of subchapter 1.3 the influence of gas radiation is numerically investigated with the methods of the Computational Fluid Dynamics (CFD). Thus, in chapter 2 a short introduction is given considering the governing equations, which are approximated and solved via CFD.

In chapter 3 a short introduction in the field of thermal radiation is given and the radiative transport equation is presented. In addition, the standard Rosseland approximation is derived from the radiative transfer equation and rewritten in conjunction with the weighted-sum-of-gray-gases (WSGG) approach.

In chapter 4 the implementation of the Rosseland model in the NSMB CFD solver is described and validated, presenting a new empirical jump boundary condition. In chapter 5 the implementation of the WSGG models is illustrated and a comparison of the selected spectral models is presented.

In order to demonstrate the impact of gas radiation in a real rocket chamber, the Space Shuttle Main Engine (SSME) main combustion chamber is selected as validation case, with the CFD studies by Naraghi et al. [20] and Wang [21] used as benchmarks.

The SSME main combustion chamber is simulated with the ANSYS CFX and FLUENT CFD solvers and the NSMB research CFD code in chapter 6. Several WSGG models identified in chapter 5 are implemented analytically in CFX. Referring to the Rosseland model in NSMB an empirical investigation is performed to identify an empirical jump boundary condition for a physically better resolution of the wall values.

The CFD simulation of the SSME main combustion chamber is divided into two studies: the original hydrogen-oxygen combustion system (chapter 6.4) and a novel methane-oxygen system (chapter 6.5).

Within the scope of the hydrogen and methane CFD studies three approximation methods for the radiative transfer equation are compared. Additionally, the impact of different derivations of the spectral WSGG approach on the radiative heat fraction is investigated in detail. Furthermore, the interaction of gas radiation and flow field is studied.

2 Governing Equations

In the scope of this thesis the contribution of radiative heat transfer is implemented into the NSMB research CFD code. For a better understanding the corresponding governing equations, which NSMB solves, are presented in the following. The coupling between the Navier-Stokes equations is discussed in chapter 4.1.

2.1 The Compressible Navier-Stokes Equations

In 3D Cartesian coordinates the unsteady compressible Navier-Stokes equations can be expressed in conservation form as

$$\frac{\partial}{\partial t}(\vec{W})+\frac{\partial}{\partial x}(\vec{f}_{\mathrm{cv}}-\vec{f}_{\mathrm{vi}})+\frac{\partial}{\partial y}(\vec{g}_{\mathrm{cv}}-\vec{g}_{\mathrm{vi}})+\frac{\partial}{\partial z}(\vec{h}_{\mathrm{cv}}-\vec{h}_{\mathrm{vi}})=0\,. \tag{1}$$

Equation (1) is given in the Eulerian formulation and holds for a fixed control volume in space. For a better overview Eq. (1) represents only the “basic” Navier-Stokes system without extensions. Regarding the energy transport only convective heat transfer, viscous effects and heat conduction are present in Eq. (1). The NSMB CFD solver additionally allows a more complex modelling of the flow problem, including e.g. chemical reactions, chemical and thermo-non-equilibrium of high enthalpy flows, turbulence modelling and a Large-Eddy formulation.
The solution of the set of partial differential equations is represented by the state vector, $\vec{W}$, i.e.

$$\vec{W}=\begin{pmatrix}\rho\\ \rho u\\ \rho v\\ \rho w\\ \rho E\end{pmatrix}, \quad \rho,u,v,w,E=f(x,y,z,t)\,, \tag{2}$$

where E is the total energy of the fluid

$$E=e+\frac{1}{2}(u^2+v^2+w^2)\,. \tag{3}$$

The convective (inviscid) fluxes are defined as

$$\vec{f}_{\mathrm{cv}}=\begin{pmatrix}\rho u\\ \rho u^2+p\\ \rho uv\\ \rho uw\\ u(\rho E+p)\end{pmatrix},\vec{g}_{\mathrm{cv}}=\begin{pmatrix}\rho v\\ \rho vu\\ \rho v^2+p\\ \rho vw\\ v(\rho E+p)\end{pmatrix},\vec{h}_{\mathrm{cv}}=\begin{pmatrix}\rho w\\ \rho wu\\ \rho wv\\ \rho w^2+p\\ w(\rho E+p)\end{pmatrix}. \tag{4}$$

The viscous (diffusive) fluxes are defined as

$$\vec{f}_{\mathrm{vi}}=\begin{pmatrix}0\\ \tau_{xx}\\ \tau_{xy}\\ \tau_{xz}\\ \Psi_x-q_{\mathrm{cd},x}\end{pmatrix},\vec{g}_{\mathrm{vi}}=\begin{pmatrix}0\\ \tau_{yx}\\ \tau_{yy}\\ \tau_{yz}\\ \Psi_y-q_{\mathrm{cd},y}\end{pmatrix},\vec{h}_{\mathrm{vi}}=\begin{pmatrix}0\\ \tau_{zx}\\ \tau_{zy}\\ \tau_{zz}\\ \Psi_z-q_{\mathrm{cd},z}\end{pmatrix}. \tag{5}$$

Assuming Newton's law of friction and the hypothesis of Stokes the elements of the stress tensor $\underline{\underline{\tau}}$ can be expressed in terms of the normal and shear stresses. The normal stresses of the viscous tensor $\underline{\underline{\tau}}$ are

$$\tau_{xx}=\frac{2}{3}\mu\left(2\frac{\partial u}{\partial x}-\frac{\partial v}{\partial y}-\frac{\partial w}{\partial z}\right), \tag{6}$$

$$\tau_{yy}=\frac{2}{3}\mu\left(-\frac{\partial u}{\partial x}+2\frac{\partial v}{\partial y}-\frac{\partial w}{\partial z}\right), \tag{7}$$

$$\tau_{zz}=\frac{2}{3}\mu\left(-\frac{\partial u}{\partial x}-\frac{\partial v}{\partial y}+2\frac{\partial w}{\partial z}\right), \tag{8}$$

and the shear stresses of the viscous tensor $\underline{\underline{\tau}}$ are

$$\tau_{xy}=\tau_{yx}=\mu\left(\frac{\partial v}{\partial x}+\frac{\partial u}{\partial y}\right), \tag{9}$$

$$\tau_{xz}=\tau_{zx}=\mu\left(\frac{\partial w}{\partial x}+\frac{\partial u}{\partial z}\right), \tag{10}$$

$$\tau_{yz}=\tau_{zy}=\mu\left(\frac{\partial v}{\partial z}+\frac{\partial w}{\partial y}\right). \tag{11}$$

The viscous dissipation in the energy equation is calculated from

$$\Psi_x=u\tau_{xx}+v\tau_{xy}+w\tau_{xz}, \tag{12}$$

$$\Psi_y=u\tau_{yx}+v\tau_{yy}+w\tau_{yz}, \tag{13}$$

$$\Psi_z=u\tau_{zx}+v\tau_{zy}+w\tau_{zz}, \tag{14}$$

and the heat flux due to conduction is calculated according to Fourier's law,

$$q_{\mathrm{cd},x}=-k\frac{\partial T}{\partial x};\ q_{\mathrm{cd},y}=-k\frac{\partial T}{\partial y};\ q_{\mathrm{cd},z}=-k\frac{\partial T}{\partial z}. \tag{15}$$

In modern CFD literature, the entire system of flow equations, Eq. (1), for the solution of a viscous flow is called Navier-Stokes equations. Equations (1) represent a coupled system of nonlinear partial differential equations which are very difficult to solve analytically. To date, there is no general closed-form solution to these equations [60].

2.2 Thermodynamic Closure of the Navier-Stokes Equations

For the Navier-Stokes equations, Eq. (1), in the conservative form five equations in terms of six unknown flow-field variables ρ, p, u, v, w, e are counted. The thermal equation of state for a perfect gas provides a sixth equation

$$p = \rho R T\,, \tag{16}$$

but it also introduces a seventh unknown, the temperature T. The caloric equation of state for a perfect gas ($c_{\mathrm{v}}, c_p = const$) relates the internal energy to the temperature of the medium

$$e = c_{\mathrm{v}} T\,, \tag{17}$$

$$c_{\mathrm{v}} = \frac{R}{\gamma - 1}, \quad c_p = \gamma\, c_{\mathrm{v}}\,. \tag{18}$$

For a caloric perfect gas the viscosity μ in Eqs. (6) to (11) can be calculated from Sutherland’s law, which states for air at standard atmosphere:

$$\frac{\mu}{\mu_{ref}} = \left(\frac{T}{T_{ref}}\right)^{3/2} \frac{\left(T_{ref} + S_{\mathrm{c}}\right)}{\left(T + S_{\mathrm{c}}\right)}\,. \tag{19}$$

The thermal heat conductivity in Eq. (15) is related to the viscosity in Eq. (19) by the Prandtl number

$$\mathrm{Pr} = \frac{\mu\, c_p}{k_{\mathrm{cd}}}\,, \tag{20}$$

which can be assumed with $\mathrm{Pr} = 0.72$ for a laminar air case and $0.78 \le \mathrm{Pr} \le 0.9$ for a turbulent air case.

3 Theory of Radiative Heat Transfer

3.1 Definition and Characteristics of the Basic Radiative Quantities

This chapter introduces significant radiative variables which are important for the understanding of the derived radiative relationships at a later stage. For a detailed explanation and derivation of radiative quantities the text books by Modest [4], Siegel & Howell [5], Hottel & Sarofim [3] are recommended. In this thesis the notation of Siegel & Howell is generally applied.

First of all, the radiation intensity within a medium is introduced, because it is a convenient quantity for studying radiative transfer in absorbing, emitting and scattering media. In this thesis the medium is always a single gas or a gas mixture without scattering particles. The spectral radiation intensity i_λ is defined as the radiation energy passing through the local area dA within the gas, per unit time, per unit of the projected area dA_p and per unit of solid angle $d\omega$. In Fig. 3 the radiation from direction θ and within the solid angle $d\omega$ passes through the infinitesimal gas surface dA. The projected area $dA_\mathrm{p} = dA\cos\theta$ is formed by taking the area dA through which the energy is passing and projecting it normal to the direction of the radiation. The radiative intensity i_λ in the gas can be imagined as an infinitesimal pencil of rays. The infinitesimal solid angle $d\omega$ is centred about the direction of i_λ and has its origin at dA. The solid angle with which an infinitesimal area dA_S is seen from a point P is defined as the projection of the surface dA onto a plane perpendicular to the direction of i_λ, divided by the square of the distance S between dA_S and P. For simplification reasons dA_S is assumed to be normal to the direction of i_λ, hence the relation for the solid angle can be written as

$$d\omega = \frac{dA_\mathrm{S}}{\mathrm{S}^2}. \tag{21}$$

The spectral radiation intensity i_λ at a wavelength λ is defined as the intensity per unit wavelength interval around a specified λ. In [4; 5] it is demonstrated that the spectral radiation intensity in a given direction in a nonattenuating and non-emitting medium with constant properties is independent of the position along a path in the given direction. This characteristic allows a suitable description of absorption, emission and scattering of radiative energy within a participating medium because any changes in intensity along any given path must be due to one or more of these phenomena.

A particular case of the spectral radiation intensity is the spectral intensity of a blackbody, declared as $i_{\lambda\mathrm{b}}$. A blackbody is a perfect absorber for all incident radiation. By definition it absorbs the maximum possible radiation from its surrounding at each wavelength and from each direction. In radiative equilibrium the blackbody emits as much energy as it absorbs, hence it is also a perfect emitter. Furthermore, the total radiant energy emitted by a blackbody in a vacuum is a function only of its temperature. In literature, e.g. in [4], a situation is referred to as radiative equilibrium when the thermodynamic equilibrium within the medium is achieved only by virtue of thermal radiation. This means that radiation is the dominant mode of heat transfer and other modes, e.g. conduction and convection are negligible.

The total blackbody intensity is defined as

$$i_{\mathrm{b}} = \int_{\lambda=0}^{\infty} i_{\lambda \mathrm{b}}(\lambda,T,t)\, d\lambda\,, \tag{22}$$

i.e. it includes the radiation for all wavelengths of the entire spectrum and is defined as the energy emitted per unit time, per unit infinitesimal surface area and in a unit elemental solid angle.

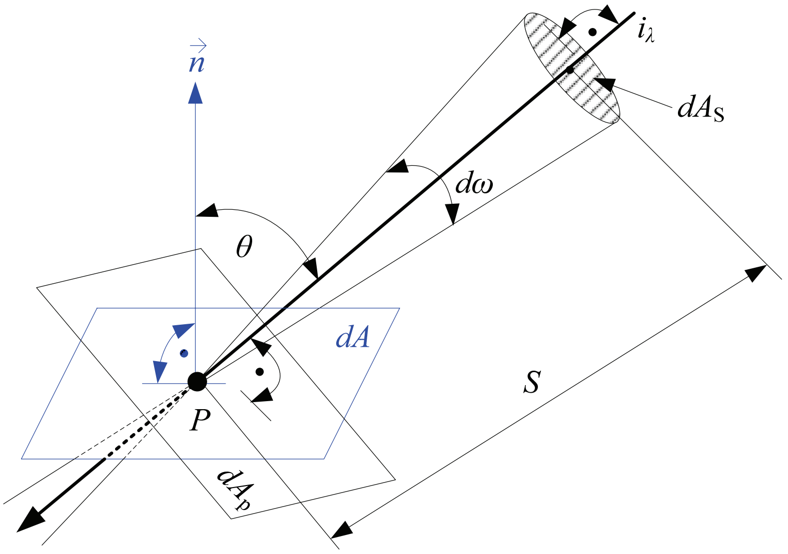

Figure 3: Definition of the spectral intensity i_λ in a radiatively participating medium

For the description of practical radiation problems it is useful to know the amount of energy a surface element (e.g. from a gas layer) is emitting in the hemisphere surrounding it. For this purpose the hemispherical spectral emissive power $e_{\lambda \mathrm{b}}$ is introduced. $e_{\lambda \mathrm{b}}$ is the energy emitted by a black surface element, per unit time, per unit area and per unit wavelength interval around λ. Two important relations between the blackbody spectral intensity and the blackbody spectral hemispherical emissive power are listed in the following.

Firstly, the blackbody spectral and total intensities, $i_{\lambda \mathrm{b}}$ respectively i_{b}, are independent of the direction so that emission of energy into a direction at θ away from the surface normal direction $\vec{n}$ (see Fig. 3) is proportional to $\cos\theta$. This is commonly known as Lambert's cosine law:

$$e_{\lambda \mathrm{b}}(\theta) = i_{\lambda \mathrm{b}} \cos\theta\,. \tag{23}$$

Secondly, when the blackbody spectral intensity is integrated over all solid angles of the hemisphere (i.e. $0 \le \theta \le \pi / 2$), it results in the following simple relation:

$$e_{\lambda \mathrm{b}} = i_{\lambda \mathrm{b}} \int\limits_{\varphi=0}^{2\pi} \int\limits_{\theta=0}^{\pi/2} \cos\theta \sin\theta \; d\theta d\varphi = \pi i_{\lambda \mathrm{b}} \,. \tag{24}$$

The spectral emissive power $e_{\lambda \mathrm{b}}$ can be calculated with Planck's spectral distribution of emissive power which is based on the quantum theory [5] and verified experimentally. For emission into a medium with refractive index n this relation gives:

$$e_{\lambda \mathrm{b}}(\lambda_0, T) = \pi i_{\lambda \mathrm{b}}(\lambda_0, T) = \frac{2\pi n^2 C_1}{\lambda_0^5 (e^{\frac{C_2}{\lambda_0 T}} - 1)} \,. \tag{25}$$

In the field of engineering it is commonly assumed that radiatively participating gases do not reduce the speed of light of the penetrating radiation. Hence the refraction index of ordinary gases can be estimated with $n = c_0 / c \approx 1$. Furthermore, it is crucial to note that the blackbody spectral intensity only depends on the wavelength and the temperature of the corresponding arbitrary volume element dV of the participating medium.
When Eq. (25) is integrated over the entire wavelength spectrum the Stefan-Boltzmann law results:

$$e_{\mathrm{b}} = \int\limits_{\lambda=0}^{\infty} e_{\lambda \mathrm{b}} \; d\lambda = \int\limits_{\lambda=0}^{\infty} \pi i_{\lambda \mathrm{b}} d\lambda = \pi i_{\mathrm{b}} = n^2 \sigma T^4 \,. \tag{26}$$

3.2 The Radiative Transfer Equation

Figure 4 illustrates an infinitesimal pencil of rays travelling into direction $\vec{s}$. The spectral intensity i_λ changes along its path from S to $S + dS$ in an absorbing, emitting and scattering medium. Assuming that only radiation is considered and no other mode of heat transfer (e.g. heat conduction, convection) the change in intensity can be written according to [4; 5] as

$$\begin{aligned} i_\lambda(S + dS, \vec{s}, t + dt) - i_\lambda(S, \vec{s}, t) = {} & \overbrace{a_\lambda(S)\; i_{\lambda \mathrm{b}}(T, t)\; dS}^{\mathrm{I}} - \overbrace{a_\lambda(S)\; i_\lambda(S, \vec{s}, t)\; dS}^{\mathrm{II}} \\ & \overbrace{- \sigma_{s\lambda}(S)\; i_\lambda(S, \vec{s}, t)\; dS}^{\mathrm{III}} \\ & + \overbrace{\frac{\sigma_{s\lambda}(S)}{4\pi} \int\limits_{\omega_{\mathrm{i}}=0}^{4\pi} i_\lambda(S, \vec{s}_{\mathrm{i}}, t)\; \Phi_\lambda(\vec{s}_{\mathrm{i}}, \vec{s})\; d\omega_{\mathrm{i}}\; dS}^{\mathrm{IV}} \end{aligned} \quad . \tag{27}$$

Equation (27) is commonly called equation of transfer or radiative transfer equation (RTE). For a fixed coordinate system the spectral intensity i_λ is a function of the location $S = S(x, y, z)$, the direction $\vec{s} = \vec{s}(\theta, \varphi)$, the time t and the wavelength λ, i.e. seven independent variables in total. Instead of the wavelength it is also common to describe the spectral dependence in terms of the frequency or the wave number. For the transfer equation it is assumed that the medium has an index of refraction of $n \approx 1$, which is a common assumption for ordinary gases.

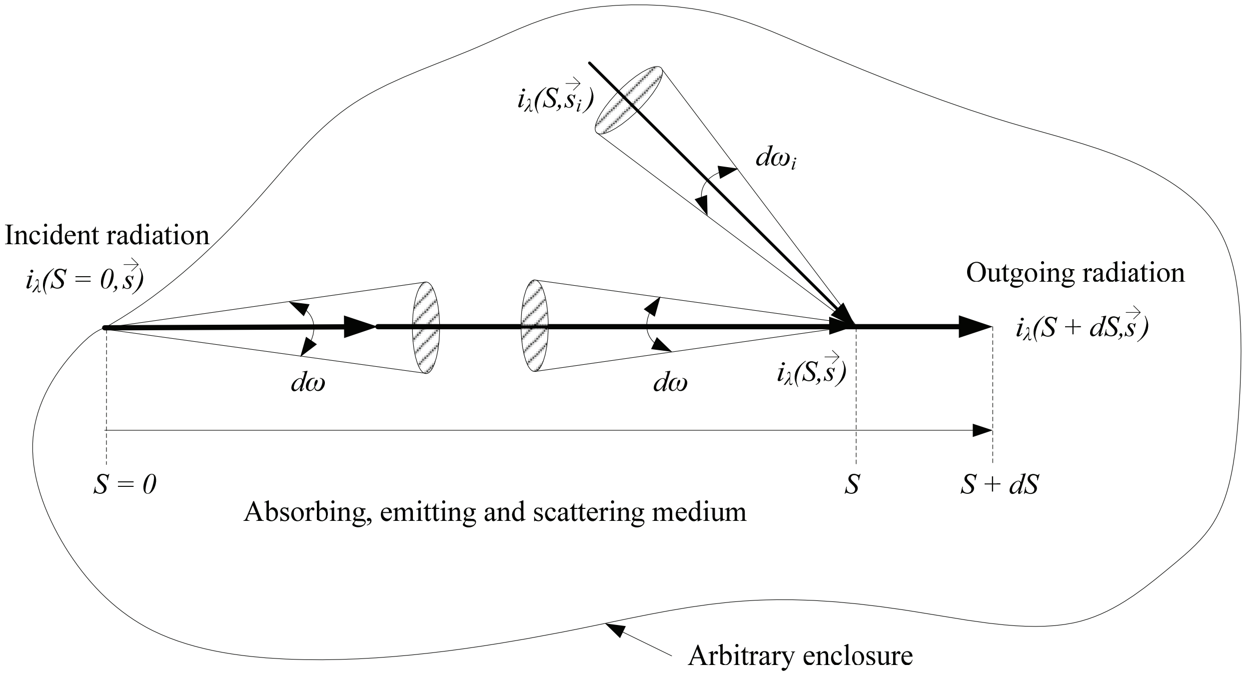

Figure 4: Enclosure for derivation of radiative transfer equation

The first term (I) of Eq. (27) represents the gain by emission and includes only spontaneous emission. Spontaneous emission is the result of an excited energy state of the considered medium in its unstable condition, decaying spontaneously to a lower energy state. As shown in [5] the spontaneous spectral emission of an isothermal volume element dV is isotropic, i.e. independent of direction. Hence the corresponding spectral intensity emitted by a volume element into any direction exactly corresponds to the blackbody spectral radiation intensity, $i_{\lambda b} = i_{\lambda b}(T,t)$. This assumption applies to an arbitrary volume element dV, which is small enough for energy emitted within dV to escape before reabsorption from other molecules within dV. The emitting gas must be in local thermodynamic equilibrium (LTE) with respect to its internal energy. The term LTE means that the incident energy absorbed by a local gas volume dV is quickly redistributed into an equilibrium distribution (Planck spectral distribution) of internal energy states at the temperature T of the gas. The assumption that a gas emits according to the Planck spectral distribution, Eq. (25), regardless of the spectral distribution of intensity passing through and being absorbed by dV is called "local thermodynamic equilibrium" (LTE) [5].

The second term (II) of Eq. (27) accounts for the loss by absorption and also includes induced emission. When the radiative energy passes the path length dS it is not only absorbed, but there is an additional phenomenon where the radiation stimulates some of the atoms or molecules to emit energy. This process is called induced emission in contrast to spontaneous emission; acting like negative absorption. The spectral absorption coefficient a_λ depends on the local properties of the medium and can be interpreted as a proportional coefficient for the augmentation of the intensity after passing dS. When scattering and spontaneous emission of the participating medium is neglected Eq. (27) gives

$$i_\lambda(S+dS,\vec{s},t+dt)-i_\lambda(S,\vec{s},t)=-a_\lambda(S)\; i_\lambda(S,\vec{s},t)\; dS\,. \tag{28}$$

The spectral absorption coefficient is a physical property and in general a function of the local temperature, pressure and composition of the medium. In this thesis the temperature and pressure are given in terms of the local thermodynamic gas condition and the composition is indicated in terms of the molar fraction X_k, of the k-th radiating species, hence $a_\lambda = a_\lambda(\lambda, T, p, X_k)$. The absorption coefficient has the unit of reciprocal length and is therefore called linear coefficient. Analogous to the mean free path of an atom or molecule in the gas dynamics, the mean free path $\tilde{S}$ for a photon is a measure for the mean penetration distance of a photon until it undergoes absorption. The general relation for a constant absorption coefficient a_λ along the path length S is

$$a_\lambda = \frac{1}{\tilde{S}}\,. \tag{29}$$

Hence, the average penetration distance before a photon is absorbed is the reciprocal of the mean free path $\tilde{S}$, when a_λ does not vary along the entire path S. Integration of Eq. (28) over a finite path length S gives

$$\int_{i_\lambda(S=0)}^{i_\lambda(S)} \frac{di_\lambda}{i_\lambda} = -\int_0^S a_\lambda(S')\; dS'\,, \tag{30}$$

where $i_\lambda(S=0)$ is the incident spectral radiation intensity at the boundary of an arbitrary control volume, see Fig. 4. On the right side of Eq. (30) a new useful dimensionless quantity is established, the spectral optical thickness or opacity which is defined as:

$$\kappa_\lambda(S) \equiv \int_0^S a_\lambda(S')\; dS'\,, \tag{31}$$

and is a function of all the values of $a_\lambda(S')$ between 0 and S. The optical thickness is a measure of the ability of the medium along a given path length S to attenuate radiation of a given wavelength, i.e. a large optical thickness provides large attenuation.

Carrying out the integration in Eq. (30) results in Bouguer's law:

$$i_\lambda(S) = i_\lambda(S=0)\cdot e^{-\kappa_\lambda(S)}\,. \tag{32}$$

Assuming that the absorption coefficient a_λ is constant along the path S and that the path length S is exactly the mean free path, i.e. $S=\tilde{S}$, and applying the relation of Eq. (29), Eq. (32) gives:

$$i_\lambda(S) = i_\lambda(S=0)\cdot e^{-\frac{1}{\tilde{S}}\cdot\tilde{S}} = i_\lambda(S=0)\cdot\frac{1}{e} \approx i_\lambda(S=0)\cdot 37\%\,. \tag{33}$$

Equation (33) reveals that for the particular case of $S=\tilde{S}$, approximately 63 % of the incident radiation intensity $i_\lambda(S=0)$ is absorbed, assuming that the medium is only absorbing (induced emission included) and not scattering.

The third term (III) of Eq. (27) stands for the loss by scattering away from the direction of $\vec{s}$ and **term (IV)** is the gain by scattering into the direction of $\vec{s}$. In general, scattering describes the interaction between photons or electromagnetic waves with small particles. In contrast to absorption a particle only changes the direction in which a photon travels. The nature of the interaction between electromagnetic waves and particles is determined by a characteristic size parameter:

$$\xi = \frac{\pi D}{\lambda_\mathrm{m}}, \tag{34}$$

where D is the spherical particle diameter and λ_m the wavelength of the surrounding medium. Three typical regimes can be distinguished:

(a) For $\xi << 1$ the particles are orders of magnitude smaller than the characteristic wavelength of the radiation: this type is called Rayleigh scattering. It is important in the atmosphere where the sunlight is scattered by gas molecules. Within the visible part of the spectrum blue light is scattered the most, resulting in a blue sky and red light is scattered the least, causing a red sunset. In [4] an example for the burning of propane is given. The volume fraction of the produced soot is observed to be 10^{-4} %, and the mean particle diameter is assumed to be $D = 0.05$ μm at a wavelength of $\lambda_\mathrm{m} = 3$ μm. Hence, the particle size parameter is $\xi \approx 0.05 \ll 1$ and therefore only Rayleigh scattering is assumed. To compare the influence of absorption and scattering, the absorption efficiency factor Q_abs,

$$Q_\mathrm{abs} = \frac{C_\mathrm{abs}}{\frac{\pi D^2}{4}}, \tag{35}$$

respectively the scattering efficiency factor Q_sca,

$$Q_{\text{sca}} = \frac{C_{\text{sca}}}{\frac{\pi D^2}{4}}, \tag{36}$$

are introduced. C_{abs} is the absorption cross section and C_{sca} the scattering cross section.
The extinction efficiency factor is

$$Q_{\text{ext}} = Q_{\text{abs}} + Q_{\text{sca}}. \tag{37}$$

The efficiency factors for the propane example are $Q_{\text{abs}} = 5.85 \cdot 10^{-2}$, $Q_{\text{sca}} = 1.21 \cdot 10^{-5}$, and $Q_{\text{ext}} = 5.85121 \cdot 10^{-2}$. Hence, the contribution of scattering to the radiative heat transfer within the propane combustion in this example is $0.0207\ \%$ and scattering may be neglected compared with absorption.

(b) For $\xi = O(1)$, or Mie scattering, the size of a particle is in the same order of magnitude compared to the wavelength of the radiation.
An example for the amount of absorption compared with scattering is given in [4] for a Mie scattering problem. For a typical particle cloud with 10^4 particles per cm^3, a wavelength of $\lambda_{\text{m}} = 3.1416\mu\text{m}$, an average particle diameter of $D = 10\mu\text{m}$ and a size parameter of $\xi \approx 10$, the absorption coefficient is $8.307 \cdot 10^{-3}\ \ 1/\text{cm}$ and the scattering coefficient is $1.073 \cdot 10^{-2}\ \ 1/\text{cm}$. The extinction coefficient is the sum of both, i.e. $1.904 \cdot 10^{-2}\ \ 1/\text{cm}$. Hence 43.6 % of the attenuation result from the absorption of the gas and 56.4 % from the scattering.

(c) For $\xi >> 1$, the surface of the particle may be treated as a normal surface and properties may be found through geometric optics.

In this thesis gas mixtures in rocket combustion chambers without suspended particles are considered in which only the species H_2O and CO_2 are radiatively participating. From the molecule sizes of H_2O and CO_2 and the characteristic infrared wavelength spectrum follows $\xi << 1$, or Rayleigh scattering. Compared to the contribution of emission and absorption of the H_2O and CO_2 molecules Rayleigh scattering can be neglected [4; 5]. Following from the absence of larger particles (e.g. soot) scattering by regime (b) and (c) can also be neglected; hence H_2O and CO_2 only absorb and emit radiative energy in the scope of this thesis. Consequently, from this point on the contribution of scattering is neglected in the following radiative relations.

Equation (27) is true for an energy balance in Lagrangian notation for a ray which travels at the speed of light c from S to $S + dS$, whereas dS and dt are related through $dS = c \cdot dt$. To obtain an Eulerian formulation the outgoing intensity may be developed into a truncated Taylor series for a single direction $\vec{s}$:

$$i_\lambda(S+dS,\vec{s},t+dt)=i_\lambda(S,\vec{s},t)+\frac{\partial i_\lambda}{\partial t}dt+\frac{\partial i_\lambda}{\partial S}dS\ , \tag{38}$$

$$di_\lambda(S,\vec{s},t)=i_\lambda(S+dS,\vec{s},t+dt)-i_\lambda(S,\vec{s},t)=\frac{\partial i_\lambda}{\partial t}dt+\frac{\partial i_\lambda}{\partial S}dS\ , \tag{39}$$

in combination with Eq. (39), Eq. (27) may be simplified to:

$$\frac{1}{c}\frac{\partial i_\lambda(S,\vec{s},t)}{\partial t}+\frac{\partial i_\lambda(S,\vec{s},t)}{\partial S}=a_\lambda(S)\ \left[i_{\lambda\mathrm{b}}(T,t)-i_\lambda(S,\vec{s},t)\right]\ . \tag{40}$$

For practical engineering applications the characteristic time scale of photon propagation is orders of magnitude larger compared to the characteristic time scale of the fluid dynamics. With this argument the first term (transient term) of Eq. (40) may be neglected [4] without significant loss of accuracy. This simplification gives:

$$\frac{\partial i_\lambda(S,\vec{s})}{\partial S}=a_\lambda(S)\ \left[i_{\lambda\mathrm{b}}(T)-i_\lambda(S,\vec{s})\right]\ . \tag{41}$$

Equation (41) is the quasi-steady form of the radiative transfer equation for absorbing and emitting media, whereas scattering and the time dependence of the intensity are neglected. Additionally, Eq. (41) does not include phenomena as polarization, dispersion, coherence, interference or quantum effects, which are therefore neglected in this thesis.

3.3 P$_1$-Approximation of the Radiative Transfer Equation

This chapter discusses the approximation of the radiative transfer equation (RTE) in the form of Eq. (41). In literature a couple of methods are presented for approximating the RTE. The majority of radiative heat transfer analyses today appear to use one of the following methods: (a) P$_N$-method (also called method of spherical harmonics, moment method, differential approximation), (b) discrete ordinates method (also called S$_N$-method or multi-flux method) or its more modern form, the finite volume method, (c) zonal method, (d) Monte Carlo method and (e) discrete transfer method which is related to the discrete ordinate and Monte Carlo method. For an elaborate description of the methods; see [4].

In this thesis the general P$_N$-method is applied to derive the simplest approximation related to this group, the P$_1$-method. Assuming radiative equilibrium, the Rosseland diffusion approximation can be derived directly from the P$_1$-method.

The P$_N$-method transforms the integral equations of radiative transfer to a set of simultaneous partial differential equations by approximating the transfer relations by a finite set of moment equation. The moments are generated by multiplying Eq. (41) by powers of direction cosines (cosine of the angle between the coordinate direction and the direction of the intensity), and then integrating the transfer equation over all solid angles $d\omega$. The general P$_N$-approximation provides one equation less than the number of unknowns generated. To solve this problem, the local radiation intensity is approximated by a series expansion in terms of spherical harmonics denoted by P, giving the P$_N$-method its name. The series is truncated after a selected number N of terms. This strategy provides a closure relation for the system of moment equations. When the series is truncated after one or three terms the method is called P$_1$ or P$_3$-approximation. The derivation of the P$_N$-method is described in [4; 5].

In the following the P$_1$-approximation is developed for a rectangular coordinate system x_1, x_2, x_3 shown in Fig. 5. For an absorbing and emitting medium the change of the spectral intensity i_λ starting at position $\vec{r}$ along the path S, in the direction of the unit vector $\vec{s}$ is given by the radiative transfer equation, Eq. (41).

At each location $\vec{r}$ in a medium radiation is travelling in all directions $\vec{s}$ away from the point S_0. Therefore it is useful to express the path S of the intensity i_λ in terms of the polar angle θ and the azimuthal angle φ in a spherical coordinate system or in terms of direction cosines l_i ($i = 1,2,3$) of the unit direction vector $\vec{s} = \vec{s}(\theta,\varphi)$, resulting in the following form:

$$\begin{aligned}\frac{\partial i_\lambda(S,\theta,\varphi)}{\partial S} &= \cos\theta \frac{\partial i_\lambda(S,\theta,\varphi)}{\partial x_1} + \sin\theta\cos\varphi \frac{\partial i_\lambda(S,\theta,\varphi)}{\partial x_2} + \sin\theta\sin\varphi \frac{\partial i_\lambda(S,\theta,\varphi)}{\partial x_3} \\ &= l_1 \frac{\partial i_\lambda(S,\theta,\varphi)}{\partial x_1} + l_2 \frac{\partial i_\lambda(S,\theta,\varphi)}{\partial x_2} + l_3 \frac{\partial i_\lambda(S,\theta,\varphi)}{\partial x_3}\end{aligned} , \quad (42)$$

where $l_1 = \cos\theta,\ l_2 = \cos\delta,\ l_3 = \cos\gamma$. For example, the direction cosine $l_1 = \cos\theta$ is the projection of the unit direction vector $\vec{s}$ on the x_1-axis. The transfer equation, Eq. (41), is then rewritten to

$$\sum_{i=1}^{3} l_i \frac{\partial i_\lambda(S,\theta,\varphi)}{\partial x_i} = a_\lambda(S)\ \left[i_{\lambda \mathrm{b}}(T) - i_\lambda(S,\theta,\varphi)\right] , \quad (43)$$

where $i_{\lambda \mathrm{b}}(T)$ is also a function of the path S because the temperature of the medium is $T = T(S)$. To develop the P$_1$-method, the intensity at each path S is expressed as an expansion in a series of orthogonal harmonic functions:

$$i_\lambda(S,\theta,\varphi) = \sum_{l=0}^{\infty} \sum_{m=-l}^{l} A_l^m(S) Y_l^m(\theta,\varphi) . \quad (44)$$

The spherical harmonics approximation of the radiation intensity is exact within the limit of an infinite number of terms in the series, $l \to \infty$. The terms $A_l^m(S)$ are position-dependent coefficients to be determined by the solution of the set of moment equations.

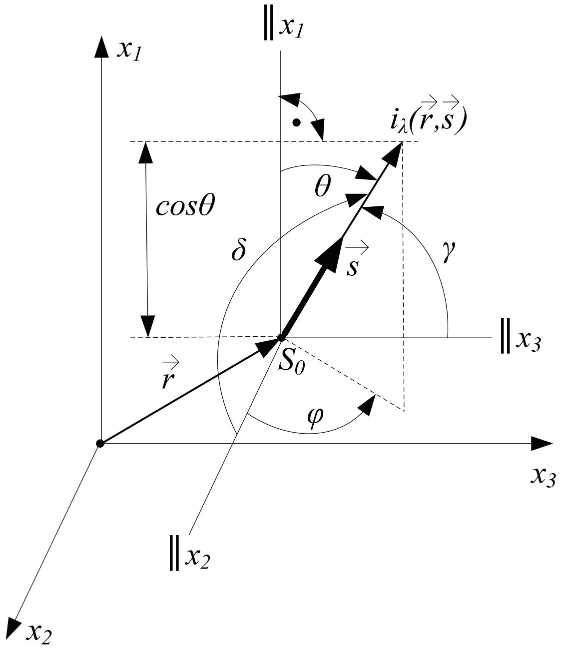

Figure 5: Coordinate system with geometrical relations for the P$_1$-approximation

The terms $Y_l^m(\theta,\varphi)$ are angularly dependent normalized spherical harmonics

$$Y_l^m(\theta,\varphi) = \left[\frac{2l+1}{4\pi}\frac{(l-|m|)!}{(l+|m|)!}\right]^{1/2} e^{jm\varphi} P_l^{|m|}(\mu), \tag{45}$$

where $j=\sqrt{-1}$ so that $e^{jm\varphi}$ provides the harmonics $\cos m\varphi$ and $\sin m\varphi$. The $P_l^{|m|}(\mu)$ with the direction cosine $\mu=\cos\theta$ are associated Legendre polynomials of the first kind, of degree l and order m,

$$P_l^{|m|}(\mu) = \frac{(1-\mu^2)^{|m|/2}}{2^l l!}\frac{d^{l+|m|}}{d\mu^{l+|m|}}(\mu^2-1)^l \tag{46}$$

The terms $P_l^{|m|}(\mu)$ are $P_l^{|m|}(\mu)\equiv 0$ for $|m|>l$ and $P_l^{|0|}(\mu)\equiv P_l\,(\mu)$. To apply the P$_N$-method, Eq. (44) is truncated after a finite number of N terms, giving the method its name. For radiative heat transfer problems in engineering it is common to truncate the series in Eq. (44) after $l=0,1$ (P$_1$-method) or $l=0,1,2,3$ (P$_3$-method). A higher-order approximation adds considerable complexity without increasing accuracy significantly. Even-order approximations (i.e. P$_2$, P$_4$ etc.) are not used because accuracy is increased only marginally compared to the next lower odd-order expansion. Moreover, boundary conditions are difficult to apply to the even-order approximations [5]. For the P$_1$-method Eq. (44) gives

$$i_\lambda(S,\theta,\varphi) = A_0^0(S)Y_0^0(\theta,\varphi) + A_1^{-1}(S)Y_1^{-1}(\theta,\varphi) + A_1^0(S)Y_1^0(\theta,\varphi) + A_1^1(S)Y_1^1(\theta,\varphi). \tag{47}$$

To evaluate intensity $i_\lambda(S,\theta,\varphi)$ in Eq. (47) the coefficients $A_l^m(S)$ are unknown and need to be determined. For this purpose, the moment approach is applied by multiplying the local intensities at location S by powers of the direction cosines l_i ($i=1,2,3$) and then integrating over all solid angles. This results in the zeroth, first and second moment, as

$$\overline{i}_{\lambda,0}(S)=\int_{\omega=0}^{4\pi} i_\lambda(S,\theta,\varphi)\,d\omega\,, \tag{48}$$

$$\overline{i}_{\lambda,i}(S)=\int_{\omega=0}^{4\pi} l_i\; i_\lambda(S,\theta,\varphi)\,d\omega \quad (3\text{ equations: } i=1,2,3)\,, \tag{49}$$

$$\overline{i}_{\lambda,ij}(S)=\int_{\omega=0}^{4\pi} l_i\; l_j\; i_\lambda(S,\theta,\varphi)\,d\omega \quad (9\text{ equations: } i,j=1,2,3)\,. \tag{50}$$

The zeroth moment, Eq. (48), can be seen as the spectral incident intensity impinging on a point in the medium from all sides at a specified wavelength. When the zeroth moment is divided by the speed of light c the spectral radiative energy density is obtained at location S as

$$u_\lambda(S)=\frac{1}{c}\int_{\omega=0}^{4\pi} i_\lambda(S,\theta,\varphi)\,d\omega\,. \tag{51}$$

Adding the contributions from all possible directions gives the total radiative energy, $u_\lambda\; dV$, stored within an infinitesimal volume dV.

The first moment, Eq. (49), is the radiative heat flux in the i-direction, and the second moment, Eq. (50), is the radiative pressure tensor. In the next step the local intensity in Eq. (44) is substituted into the integrals of the moment equations and the integrations are carried out. Siegel et al. [5] present forms for the unknown $A_l^m(S)$ coefficients in terms of the moments. Substituting these expressions for $A_l^m(S)$ into Eq. (44) gives the relation for the P$_l$-approximation for the local intensity $i_\lambda(S,\theta,\varphi)$ in terms of its moments as

$$i_\lambda(S,\theta,\varphi)=\frac{1}{4\pi}\Big[\overline{i}_{\lambda,0}(S)+3\overline{i}_{\lambda,1}(S)\cos\theta+3\overline{i}_{\lambda,2}(S)\sin\theta\cos\varphi+3\overline{i}_{\lambda,3}(S)\sin\theta\sin\varphi\Big]. \tag{52}$$

To continue the derivation expressions for the zeroth, first and second moments of intensity must be developed in order to obtain explicit relations for the P$_l$-approximation of intensity from Eq. (52). This is done by generating moment-differential equations from the differential radiative transfer equation, Eq. (43). The first moment-differential equation is generated by integrating Eq. (43) over all solid angles $d\omega$

$$\sum_{i=1}^{3} l_i \frac{\partial i_\lambda(S,\theta,\varphi)}{\partial x_i} = a_\lambda(S)\;\left[i_{\lambda \mathrm{b}}(T) - i_\lambda(S,\theta,\varphi)\right] \;\Bigg|\; \int\limits_{\omega=0}^{4\pi} \; d\omega, \tag{43}$$

giving

$$\sum_{i=1}^{3} \int\limits_{\omega=0}^{4\pi} l_i \frac{i_\lambda(S,\theta,\varphi)}{\partial x_i}\, d\omega = a_\lambda(S) \left[\int\limits_{\omega=0}^{4\pi} i_{\lambda \mathrm{b}}(T)\, d\omega - \int\limits_{\omega=0}^{4\pi} i_\lambda(S,\theta,\varphi)\, d\omega \right] . \tag{53}$$

The integrals over solid angles and the derivatives can be interchanged and substitution of the zeroth and first moment from Eqs. (48) and (49) into Eq. (53) gives the first moment-differential equation

$$\sum_{i=1}^{3} \frac{\partial \overline{i}_{\lambda,i}(S)}{\partial x_i} = a_\lambda(S)\;\left[4\pi i_{\lambda \mathrm{b}}(T) - \overline{i}_{\lambda,0}(S)\right] \;, \tag{54}$$

where the index i represents the Cartesian coordinate direction x_i.

The set of second moment-differential equations is obtained by multiplying the radiative transfer equation, Eq. (43), by the direction cosine l_j and integration over all solid angles $d\omega = \sin\theta\; d\theta\; d\varphi$

$$\sum_{i=1}^{3} \int\limits_{\omega=0}^{4\pi} l_j\; l_i \frac{\partial i_\lambda(S,\theta,\varphi)}{\partial x_i} d\omega = a_\lambda(S) \left[i_{\lambda \mathrm{b}}(T) \overbrace{\int\limits_{\omega=0}^{4\pi} l_j\; d\omega}^{=0} - \int\limits_{\omega=0}^{4\pi} l_j\; i_\lambda(S,\theta,\varphi)\, d\omega \right] , \tag{55}$$

where the index j represents a coordinate direction with $j = 1,2,3$, i.e. three equations result for the second differential moments. Substituting the first and second moments from Eqs. (49) and (50) into Eq. (55) gives the three second moment-differential equations

$$\sum_{i=1}^{3} \frac{\partial \overline{i}_{\lambda,ij}(S)}{\partial x_i} = -a_\lambda(S)\; \overline{i}_{\lambda,j}(S) \quad (3 \text{ equations:} j = 1,2,3) \,. \tag{56}$$

Up to this point two moment-differential equations, Eqs. (54) and (56) are present but three unknown moments $\overline{i}_{\lambda,0}(S)$, $\overline{i}_{\lambda,i}(S)$ and $\overline{i}_{\lambda,ij}(S)$. To close the set of moment-differential equations values must be found for the three unknown moments. This problem is solved by substituting Eq. (52) into the second moment equation, Eq. (50), to generate a relation for the second moment $\overline{i}_{\lambda,ij}(S)$. This relation is not exact because Eq. (52) was truncated to $N = 1$ for the P_1-method. However, an approximate closure condition [4; 5] is generated and gives

$$\overline{i}_{\lambda,ij}(S) = \frac{1}{3}\delta_{ij}\overline{i}_{\lambda,0}(S) , \tag{57}$$

where δ_{ij} is the Kronecker delta, with $\delta_{ij}=1$ for $i=j$ and $\delta_{ij}=0$ for $i\neq j$, hence $\overline{i}_{\lambda,11}(S)=\overline{i}_{\lambda,22}(S)=\overline{i}_{\lambda,33}(S)=\overline{i}_{\lambda,0}(S)/3$ and all the other $\overline{i}_{\lambda,ij}(S)=0$. Levermore [61] discusses in detail the non-trivial problem to obtain a suitable closure condition, i.e. the term "$1/3\cdot\delta_{ij}$" in Eq. (57). The fact that the non-diagonal elements (i.e. $\delta_{ij}=0$) of the pressure tensor $\overline{i}_{\lambda,ij}(S)$ are zero results from the rotational invariance of the radiative intensity. The rotational invariance of the intensity can be physically interpreted as the axis-symmetry distribution of the radiative intensity around the path of transfer. The result that only the diagonal elements $\overline{i}_{\lambda,11}(S),\overline{i}_{\lambda,22}(S),\overline{i}_{\lambda,33}(S)$ contribute to the radiative pressure $\overline{i}_{\lambda,ij}(S)$ follows from the fact that the axis-symmetric characteristic of the intensity only induces radiative pressure normal to the direction of transfer.

From a mathematical point of view the factor $1/3$ in Eq. (57) is one possible result of the so called "moment closure problem" according to the classical Eddington approximation [62]. Due to the fact that the radiative intensity is considered isotropic within the moment approach, the factor $1/3$ can be physically interpreted as follows: from the isotropy of the incident intensity follows that $\overline{i}_{\lambda,0}(S)$ is equal for all paths of transfer impinging on a point in the medium. Hence the contribution of the incident intensity to the radiative pressure in one spatial direction (i.e. x_i, with $i=1,2,3$) corresponds to $1/3$ of the total incident radiation.

Inserting Eq. (57) into the second moment-differential equations, Eq. (56), gives

$$\sum_{i=1}^{3}\frac{1}{3}\delta_{ij}\,\frac{\partial\overline{i}_{\lambda,0}(S)}{\partial x_i}=-a_\lambda(S)\;\overline{i}_{\lambda,j}(S)\quad(3\text{ equations: } j=1,2,3)\,. \tag{58}$$

Equations (54) and (58) are called the P$_1$-approximation of the radiative transfer equation in terms of radiative intensity as transport variable.

In order to apply the finite volume method to the numerical discretisation of the differential equations it is more convenient to express the P$_1$-equations, Eqs. (54) and (58), in terms of flux based quantities. First of all, the zeroth moment, Eq. (48), is restated in terms of a scalar, $G_\lambda(\vec{r})$, which is defined as the spectral incident radiation function, describing the total intensity impinging on a point $\vec{r}$ in the medium from all directions

$$G_\lambda(\vec{r})=\overline{i}_{\lambda,0}(\vec{r})=\int_{\omega=0}^{4\pi} i_\lambda(\vec{r},\vec{s})\;d\omega\,, \tag{59}$$

where the path variable S from Eq. (48) is substituted by the three-dimensional position vector $\vec{r}$. Furthermore, the second moment, Eq. (49), is commonly written in terms of the spectral radiative flux vector which is related to the radiative intensity as

$$\vec{q}_{\mathrm{r},\lambda}(\vec{r}) = \int_{\omega=0}^{4\pi} i_\lambda(\vec{r},\vec{s})\;\vec{s}\;d\omega = \begin{pmatrix} \overline{i}_{\lambda,1}(\vec{r}) \\ \overline{i}_{\lambda,2}(\vec{r}) \\ \overline{i}_{\lambda,3}(\vec{r}) \end{pmatrix} \;. \tag{60}$$

Supposing Eqs. (59) and (60), the first P_1-equation, Eq. (54), can be written as

$$\frac{\partial \overline{i}_{\lambda,1}(\vec{r})}{\partial x_1} + \frac{\partial \overline{i}_{\lambda,2}(\vec{r})}{\partial x_2} + \frac{\partial \overline{i}_{\lambda,3}(\vec{r})}{\partial x_3} = a_\lambda(\vec{r})\;\left[4\pi i_{\lambda\mathrm{b}}(T) - G_\lambda(\vec{r})\right], \tag{61}$$

and give the scalar equation in terms of the spectral radiative flux as

$$\vec{\nabla}\cdot\vec{q}_{\mathrm{r},\lambda}(\vec{r}) = a_\lambda(\vec{r})\;\left[4\pi i_{\lambda\mathrm{b}}(T) - G_\lambda(\vec{r})\right], \tag{62}$$

where the temperature is also a function of the location in the medium, i.e. $T = T(\vec{r})$. The second P_1-equation, Eq. (58), can be rearranged as

$$\begin{aligned}
\frac{1}{3}\left(\delta_{11}\frac{\partial \overline{i}_{\lambda,0}(\vec{r})}{\partial x_1} + \delta_{21}\frac{\partial \overline{i}_{\lambda,0}(\vec{r})}{\partial x_2} + \delta_{31}\frac{\partial \overline{i}_{\lambda,0}(\vec{r})}{\partial x_3}\right) &= -a_\lambda(\vec{r})\;\overline{i}_{\lambda,1}(\vec{r}) \\
\frac{1}{3}\left(\delta_{12}\frac{\partial \overline{i}_{\lambda,0}(\vec{r})}{\partial x_1} + \delta_{22}\frac{\partial \overline{i}_{\lambda,0}(\vec{r})}{\partial x_2} + \delta_{32}\frac{\partial \overline{i}_{\lambda,0}(\vec{r})}{\partial x_3}\right) &= -a_\lambda(\vec{r})\;\overline{i}_{\lambda,2}(\vec{r}) \\
\frac{1}{3}\left(\delta_{13}\frac{\partial \overline{i}_{\lambda,0}(\vec{r})}{\partial x_1} + \delta_{23}\frac{\partial \overline{i}_{\lambda,0}(\vec{r})}{\partial x_2} + \delta_{33}\frac{\partial \overline{i}_{\lambda,0}(\vec{r})}{\partial x_3}\right) &= -a_\lambda(\vec{r})\;\overline{i}_{\lambda,3}(\vec{r})
\end{aligned} \tag{63}$$

and with Eqs. (59) and (60) combined as

$$\vec{\nabla} G_\lambda(\vec{r}) = -3\;a_\lambda(\vec{r})\;\vec{q}_{\mathrm{r},\lambda}(\vec{r}) \,. \tag{64}$$

Equations (62) and (64) are known in literature [4; 5] as the P_1-method or P_1-approximation of the radiative transfer equation in flux notation. Milne [63] and Eddington [62] (Milne-Eddington approximation) independently developed a one-dimensional approximation for the radiative transfer equation in a plane-parallel medium and in principle obtained the same results as for Eqs. (62) and (64). Krook [64] showed that the P_1-method derived on the basis of spherical harmonics, as presented in this chapter, is equivalent to the Milne-Eddington approximation.

3.4 Rosseland Approximation of the Radiative Transfer Equation

In this thesis the Rosseland diffusion approximation is implemented into the NSMB CFD Solver. The Rosseland approximation can be assigned to the P_N-method and is the simplest form of that group. The method was derived first by Rosseland [65] in 1931 on the basis of photon diffusion by extension of a basic notation of Jeans [66]. The following argumentation shows that the Rosseland approximation is a special case of the P$_N$-method, assuming radiative equilibrium. Radiative equilibrium in terms of the radiative heat flux without internal heat sources is defined as

$$\int_{\lambda=0}^{\infty} \vec{\nabla} \cdot \vec{q}_{\mathrm{r},\lambda}(\vec{r})\, d\lambda = \vec{\nabla} \cdot \vec{q}_{\mathrm{r}}(\vec{r}) = 0\,, \tag{65}$$

where $\vec{q}_{\mathrm{r}}(\vec{r})$ is the total radiative heat flux for the entire wavelength spectrum [4; 5]. Considering an infinitesimal volume dV, the divergence of the total radiative heat flux, $\vec{\nabla} \cdot \vec{q}_{\mathrm{r}}(\vec{r})$, is the total amount of energy per unit time (net flux) leaving and entering the volume dV; it is expressed in the unit $[\mathrm{W/m^3}]$. Assuming radiative equilibrium Eq. (62) reduces to

$$G_{\lambda}(\vec{r}) = 4\pi i_{\lambda \mathrm{b}}(T) = 4 e_{\lambda \mathrm{b}}(T)\,, \tag{66}$$

i.e. the incoming radiation $G_{\lambda}(\vec{r})$ impinging on a point from all sides, it is four times the blackbody spectral emissive power, Eq. (25), emitted by this point. Inserting Eq. (66) in the second P$_1$-equation, Eq. (64), gives

$$\vec{q}_{\mathrm{r},\lambda}(\vec{r}) = -\frac{4}{3\, a_{\lambda}(\vec{r})}\, \vec{\nabla} e_{\lambda \mathrm{b}}(T)\,. \tag{67}$$

Integrating Eq. (67) over the entire wavelength spectrum and applying Eq. (26) gives the total radiative heat flux as

$$\vec{q}_{\mathrm{r}}(\vec{r}) = \int_{\lambda=0}^{\infty} \vec{q}_{\mathrm{r},\lambda}(\vec{r})\, d\lambda = -\frac{4}{3\, a_{\mathrm{R}}(\vec{r})}\, \vec{\nabla} e_{\mathrm{b}}(T) = -\frac{4 n^2 \sigma}{3\, a_{\mathrm{R}}(\vec{r})}\, \vec{\nabla}[T(\vec{r})]^4\,. \tag{68}$$

where $a_{\mathrm{R}}(\vec{r})$ is the Rosseland mean absorption coefficient and n the refractive index, which can be assumed to be $n = c_0 / c \approx 1$ for ordinary gas mixtures. Equations (67) and (68) are commonly known as the Rosseland approximation since they were originally derived by Rosseland [65; 67] or the diffusion approximation since Eq. (68) is of the same type as Fourier's law of heat diffusion (conduction), see Eq. (15), and Fick's law of mass diffusion. The Rosseland diffusion approximation reveals that the radiative heat flux depends only on the conditions (temperature, pressure, species concentration) in the immediate vicinity of the position being considered and is expressed in terms of the temperature gradient of the local conditions at that position. For further reading, Hottel & Sarofim [3] elucidate in their book a discrete and continuum approach to directly derive the Rosseland approximation without applying the method of spherical harmonics.

By expanding the temperature gradient in Eq. (68) in a Taylor series and neglecting terms of higher order, one can define a “radiative heat conductivity”

$$k_{\mathrm{R}} = \frac{16 n^2 \sigma T^3}{3 a_{\mathrm{R}}}, \tag{69}$$

and restate the radiative flux as

$$\vec{q}_{\mathrm{r}} = -k_{\mathrm{R}} \vec{\nabla} T . \tag{70}$$

The Rosseland approximation is valid only for optical thick media. The optical thickness as defined in Eq. (31) should be $\kappa_\lambda >> 1$ for an optical thick medium. In [5] a value of $\kappa_\lambda > 10$ is postulated for optical thick situations, but this value may need to be larger in some instances and only holds on a spectral basis. This means that the main absorbing and emitting wavelength bands $d\lambda_i$ of the medium must fulfil $\kappa_\lambda > 10$ in order to be able to treat the entire medium as optically thick.

When radiation is the only energy transport mechanism (radiative equilibrium, i.e. heat conduction and convection are neglected) the Rosseland approximation is strictly considered valid only in the translucent medium at locations far enough away from any solid wall boundary [4; 5]. To solve this problem, jump boundary conditions are applied to relate Eqs. (69) and (70) to the solid wall boundary conditions [68]. The jump effect is negligible when heat conduction dominates over the radiative heat transport [69], for the case of radiation and heat conduction only. It should be noted that up to know it is not clear how to apply realistic solid wall boundary conditions to the Rosseland approximation for the coupling of gas radiation with convection and heat conduction [70], especially for high enthalpy flows dominated by forced convection.

For the implementation of the Rosseland Radiation Model into the NSMB CFD code Eqs. (69) and (70) are applied to a constant absorption coefficient a_{R}. For a spectral dependent absorption coefficient a_λ Eq. (67) is used in conjunction with the weighted-sum-of-gray-gases approach (WSGG).

3.5 The Weighted Sum of Gray Gases Model (WSGGM)

For the modelling of the spectral absorption coefficient a_λ in Eq. (67) the weighted-sum-of-gray-gases approach (WSGG) is used. The WSGG approach was introduced first by Hottel & Sarofim [3] within the framework of the zonal method. The WSGGM approximates the integration of spectral properties by a summation over a small set of I gray gases or gray bands respectively, each with a constant absorption coefficient a_i, to simulate the properties of the nongray gas. The heat transfer rates are calculated independently for each gray band and the total radiation heat flux is then obtained by adding the heat fluxes of the gray gases after multiplication with certain weight factors w_i.

Modest [4] showed that the WSGG approach can be used with any solution method for the radiative transfer equation (e.g. Rosseland diffusion approximation, P$_N$-Approximation, Discrete Ordinates Method, exact solution etc.) with the limitation that all boundaries are black and the medium is non-scattering. Lallemant et al. [71] compare several WSGG models and conclude the limitations of this approach for the application in CFD computer codes for flame modelling. Denison & Webb [58; 72-76] further developed the WSGG method and introduced the spectral-line-weighted-sum-of-gray-gases model (SLWSGGM). They determined the absorption coefficients a_i and weights w_i from the line-by-line database HITRAN 92 [77]. Modest & Zhang [78] showed that the SLWSGGM is a simple form of the general Full-Spectrum k-Distribution (FSK) method.

The notation of the following WSGG equations is analogue to Siegel & Howell [5] in conjunction with Hottel & Sarofim [3] and Smith et al. [79]. The total emissivity of a real gas or gas mixture is approximated by

$$\varepsilon_{\mathrm{g}} \simeq \sum_{i=0}^{I} w_i \left[1 - e^{-a_i S}\right]. \tag{71}$$

Neither the weighting factors w_i nor the absorption coefficients a_i may depend on path length S but local variations (i.e. from one infinitesimal volume dV to an adjacent dV) are allowed [4]. The challenge is to find suitable weights w_i and absorption coefficients a_i in Eq. (71).

In order to approximate the spectral dependence of the Rosseland equation, Eq. (67), the WSGG model by Smith et al. [79] is implemented as first spectral model into the NSMB CFD solver. In Smith's WSGGM the weighting factors are only a function of the gas temperature, i.e. $w_i = w_i(T)$. The absorption coefficients a_i in Eq. (71) are

$$a_i = a_{p,i} \sum_{k=1}^{K} X_k \, p = a_{p,i} \sum_{k=1}^{K} p_k \,, \tag{72}$$

where X_k is the molar fraction of the radiating species k, e.g. H_2O or CO_2 and p is the static pressure of the gas mixture. According to the common convention the unit "physical atmosphere" (1 atm = 101325 Pa) is used for the pressure absorption coefficients $a_{p,i}$, in the scope of this thesis. Additionally for the discussion of different WSGG models the term "atm" is used to identify the reference pressure of the corresponding WSGGM. Characteristic for Smith's WSGGM is the fact that the weights w_i and effective pressure absorption coefficients $a_{p,i}$ are evaluated by fitting Eq. (71) to a table of measured total gas emissivities ε_g of the real gas [79]. The effective pressure absorption coefficient for the "clear" gas, $i = 0$, is $a_{p,i} = 0$ to account for windows in the spectrum between spectral regions of high absorption, see Fig. 6. In Eq. (71) each weighting factor w_i must be a positive value. For a spatially constant total absorption coefficient $a \neq S$ in a gray gas, the total gas emissivity can be expressed in terms of Bouguer's attenuation law, Eq. (32), as [4]:

$$\varepsilon_g = 1 - e^{-a\,S} \,. \tag{73}$$

When the optical thickness ($\kappa = a\,S$) tends to infinity, the total gas emissivity ε_g approaches unity for an infinitely thick medium. Hence in Eq. (71), all weighting factors w_i must sum to unity

$$\sum_{i=0}^{I} w_i(T) = 1 \,. \tag{74}$$

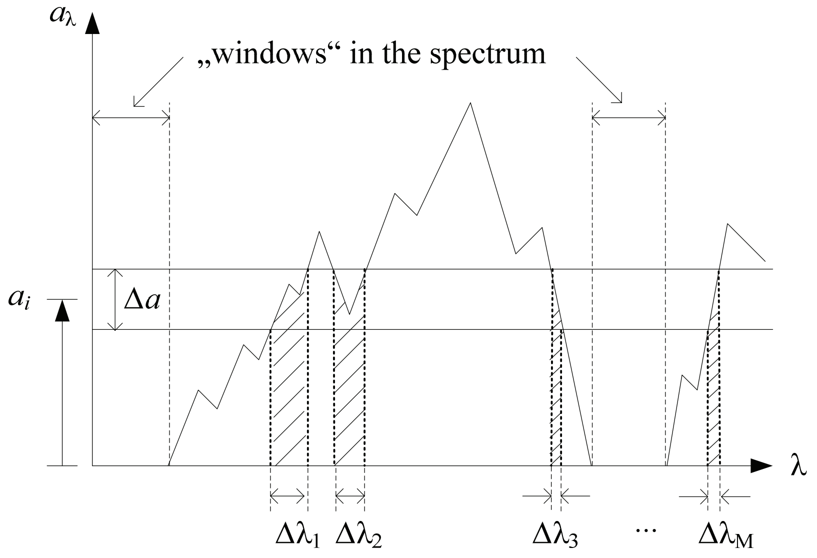

Figure 6: Physical interpretation of w_i in terms of spectral energy distribution; modified from [3]

If the number of terms in Eq. (71) is very large, the weighting factor w_i may be thought of as the energy fraction of the blackbody spectral intervals in which the absorption coefficient is around a_i, i.e.

$$w_i(T) = \sum_{m=1}^{M} \frac{e_{\lambda_m \mathrm{b}}}{e_\mathrm{b}} \Delta\lambda_m \,, \tag{75}$$

where $\Delta\lambda_m$ are the wavelength intervals in which $a = a_i \pm \Delta a / 2$, illustrated by the shaded areas in Fig. 6 [3; 4]. The WSGG method can be considered as a box model with thousands of boxes across the spectrum but relatively few different box heights a_i. The weight factors w_i are simply the sum of the $(e_{\lambda \mathrm{b}} \Delta\lambda)_m$ for all “boxes” with height a_i and normalized by the blackbody emissive power e_b; i.e., the w_i represents the fraction of the blackbody emissive power spectrum $e_{\lambda_m \mathrm{b}} / e_\mathrm{b}$ in wavelength intervals $\Delta\lambda_m$ associated with Δa (sum of shaded areas in Fig. 6).

For a molecular gas with its "spectral windows" it would take a very large path length S until the total emissivity in Eq. (73) approaches unity. For this reason Eq. (71) starts with $i = 0$. The weighting factor w_i for the "clear" gas ($i = 0$) is evaluated via the constraint:

$$w_0 = 1 - \sum_{i=1}^{I} w_i(T) . \tag{76}$$

Thus, only I values of the weighting factors need to be determined. According to [79] the weighting factors w_i are a function of only the temperature and can be expressed as polynomials (order $J-1$):

$$w_i(T) = \sum_{j=1}^{J} b_{i,j} \cdot T^{j-1} . \tag{77}$$

where $b_{i,j}$ are the polynomial coefficients given in Smith et al. [79]. In the scope of this thesis the triatomic gases water vapour (H_2O) and carbon dioxide (CO_2) are considered as main radiating species and significantly absorb in the infrared wavelength region. Absorption and emission of both species is significant only in certain (small) wavelength regions and typically looks like illustrated in Fig. 6. Water vapour has strong absorption peaks around the wavelength bands $1.38\ \mu\text{m}$, $1.87\ \mu\text{m}$, $2.7\ \mu\text{m}$, $6.3\ \mu\text{m}$ and carbon dioxide for the specific wavelength bands $2\ \mu\text{m}$, $2.7\ \mu\text{m}$, $4.3\ \mu\text{m}$ and $15\ \mu\text{m}$. Both examples are for gas temperatures around 1000 K and a characteristic pressure of 10 atm [5].

3.6 The WSGGM in Conjunction with the Rosseland Radiation Model

The previous two subchapters introduced on the one hand the Rosseland method which approximates the "transport" part of the radiative transport equation (RTE) and on the other hand the weighted-sum-of-gray-gases model (WSGGM) which approximates the spectral dependence of the radiative properties of the RTE. The current chapter derives the final relation between Rosseland and WSGGM which is implemented into the NSMB CFD solver.

The one-dimensional Rosseland diffusion equation, Eq. (67), for a refractive index close to unity is integrated over the entire wavelength spectrum

$$q_{\mathrm{r},x} = \int_{\lambda=0}^{\infty} q_{\mathrm{r},\lambda,x}\, d\lambda = \int_{\lambda=0}^{\infty} -\frac{4}{3a_\lambda} \frac{\partial e_{\lambda \mathrm{b}}}{\partial x} d\lambda , \tag{78}$$

where the spectral dependent variables are the blackbody spectral emissive power $e_{\lambda b}$ and the spectral absorption coefficient a_λ. To obtain the radiative heat flux in a certain wavelength range $\Delta\lambda$, $q_{\mathrm{r},\lambda,x}$ is integrated over $\Delta\lambda = \lambda_2 - \lambda_1$ and gives

$$q_{\mathrm{r},\Delta\lambda,x} = \int_{\lambda_1}^{\lambda_2} -\frac{4}{3a_\lambda}\frac{\partial e_{\lambda\mathrm{b}}}{\partial x}\, d\lambda\,. \tag{79}$$

As exemplified in the previous subchapter, the basic assumption of the WSGG approach is that a_λ is independent of the wavelength in a narrow wavelength range $\Delta\lambda = \lambda_2 - \lambda_1$; therefore a_λ can be written before the integral in Eq. (79). Hence, a mean absorption coefficient $a_{\mathrm{R},\Delta\lambda}$ which is constant in the interval $\Delta\lambda$ can be introduced. Equation (79) is then rearranged to

$$q_{\mathrm{r},\Delta\lambda,x} = \int_{\lambda_1}^{\lambda_2} -\frac{4}{3a_\lambda}\frac{\partial e_{\lambda\mathrm{b}}}{\partial x}\, d\lambda \equiv -\frac{4}{3a_{\mathrm{R},\Delta\lambda}}\int_{\lambda_1}^{\lambda_2}\frac{\partial e_{\lambda\mathrm{b}}}{\partial x}\, d\lambda = -\frac{4}{3a_{\mathrm{R},\Delta\lambda}}\frac{\partial}{\partial x}\int_{\lambda_1}^{\lambda_2} e_{\lambda\mathrm{b}}\, d\lambda = -\frac{4}{3a_{\mathrm{R},\Delta\lambda}}\frac{\partial e_{\Delta\lambda\mathrm{b}}}{\partial x}\,. \tag{80}$$

Dividing the first term by the second term in Eq. (80) delivers the definition for the mean attenuation coefficient $a_{\mathrm{R},\Delta\lambda}$ for the wavelength interval $\Delta\lambda$:

$$\frac{1}{a_{\mathrm{R},\Delta\lambda}} \equiv \frac{\displaystyle\int_{\lambda_1}^{\lambda_2}\frac{1}{a_\lambda}\frac{\partial e_{\lambda\mathrm{b}}}{\partial x}\, d\lambda}{\displaystyle\int_{\lambda_1}^{\lambda_2}\frac{\partial e_{\lambda\mathrm{b}}}{\partial x}\, d\lambda} = \frac{\displaystyle\int_{\lambda_1}^{\lambda_2}\frac{1}{a_\lambda}\frac{\partial e_{\lambda\mathrm{b}}}{\partial e_\mathrm{b}}\, d\lambda}{\displaystyle\int_{\lambda_1}^{\lambda_2}\frac{\partial e_{\lambda\mathrm{b}}}{\partial e_\mathrm{b}}\, d\lambda}\,. \tag{81}$$

Integrating Eq. (81) over the entire wavelength range leads to

$$\int_{\lambda=0}^{\infty}\frac{1}{a_{\mathrm{R},\Delta\lambda}} = \frac{\displaystyle\int_{\lambda=0}^{\infty}\frac{1}{a_\lambda}\frac{\partial e_{\lambda\mathrm{b}}}{\partial x}\, d\lambda}{\dfrac{\partial e_\mathrm{b}}{\partial x}}, \tag{82}$$

and gives the definition for the Rosseland mean attenuation coefficient a_R

$$\frac{1}{a_\mathrm{R}} \equiv \int_{\lambda=0}^{\infty}\frac{1}{a_\lambda}\frac{\partial e_{\lambda\mathrm{b}}}{\partial e_\mathrm{b}}\, d\lambda\,. \tag{83}$$

Integrating Eq. (80) over the entire wavelength spectrum delivers the total radiative heat flux in x-direction

$$q_{\mathrm{r},x} = -\frac{4}{3a_\mathrm{R}}\int_{\lambda=0}^{\infty}\frac{\partial e_{\lambda\mathrm{b}}}{\partial x}\, d\lambda = -\frac{4}{3a_\mathrm{R}}\frac{\partial e_\mathrm{b}}{\partial x} = -\frac{4}{3a_\mathrm{R}}\frac{\partial(\sigma T^4)}{\partial x} \approx -\frac{16\sigma T^3}{3a_\mathrm{R}}\frac{\partial T}{\partial x}\,. \tag{84}$$

Equation (84) is used in the NSMB CFD solver in the cases of a constant total absorption coefficient a_R. This approximation is not very accurate since the absorption coefficient of gases strongly depends on the wavelength. To account for the spectral property of the absorption coefficient the WSGG approach is used to calculate “weighted” radiative fluxes and sum these up to the total radiative flux. Therefore, the total radiative flux in Eq. (84) is approximated by a sum of radiative fluxes $q_{\mathrm{r},i,x}$, resulting from the i-th virtual gray gas (gray band):

$$q_{\mathrm{r},x} = \int_{\lambda=0}^{\infty} q_{\mathrm{r},\lambda,x}\, d\lambda \simeq \sum_{i=1}^{I} q_{\mathrm{r},i,x} \,. \tag{85}$$

The i-th radiative flux $q_{\mathrm{r},i,x}$ is derived by applying Eq. (84) to the i-th virtual gray gas, and expressing the Rosseland mean attenuation coefficient, Eq. (83), in terms of the i-th virtual gray gas, as

$$\frac{1}{a_{\mathrm{R}}} \equiv \frac{1}{a_i} \int_{\lambda=0}^{\infty} \frac{\partial e_{\lambda \mathrm{b}}}{\partial e_{\mathrm{b}}}\, d\lambda \simeq \frac{1}{a_i} \sum_{m=1}^{M} \frac{e_{\lambda_m \mathrm{b}}}{e_{\mathrm{b}}} \Delta\lambda_m = \frac{1}{a_i} w_i(T) \,, \tag{86}$$

where the integral over the fraction of the emissive power is approximated by the sum over all wavelength intervals $\Delta\lambda_m$, associated with a_i, as explained with Eq. (75) and depicted in Fig. 6. With Eqs. (86) and (84) the i-th radiative flux in x-direction can be calculated as

$$q_{\mathrm{r},i,x} = -\frac{16\sigma T^3}{3} \frac{w_i(T)}{a_{\mathrm{i}}} \frac{\partial T}{\partial x} \,, \tag{87}$$

where the i-th absorption coefficient is given in Eq. (72) and repeated here for a better understanding

$$a_i = a_{p,i} \sum_{k=1}^{K} X_k \, p = a_{p,i} \sum_{k=1}^{K} p_k \,. \tag{72}$$

The total radiative heat flux is obtained by adding the contributions of the I virtual gray gases

$$q_{\mathrm{r},x} = -\frac{16\sigma T^3}{3} \frac{\partial T}{\partial x} \sum_{i=1}^{I} \frac{w_i(T)}{a_{\mathrm{i}}} \,. \tag{88}$$

The sum in Eq. (88) begins with index $i = 1$ because the clear gas component ($i = 0$) does not affect the radiative heat transfer since $a_0 = 0$. However, the clear gas still affects the calculation of the weighting factors $w_i(T)$, see Eq. (76); i.e. it is indirectly included in Eq. (88). After the calculation of the direction dependent Cartesian fluxes $q_{\mathrm{r},x}$, $q_{\mathrm{r},y}$ and $q_{\mathrm{r},z}$ the divergence of the total radiative heat flux, $\nabla \vec{q}_{\mathrm{r}}$, is evaluated and added to the overall energy equation of the NSMB CFD code.

4 Implementation of the Rosseland Radiation Model (RRM)

In the following subchapters the implementation of the Rosseland Radiation Model (RRM) into the NSMB CFD code [80; 81] is described. First of all, the energy equation of NSMB is extended to include the contribution of the radiative heat flux. This is followed by a description of the finite volume discretisation of the Rosseland equations according to the finite volume notation in NSMB. For the numerical solution of the Rosseland approximation boundary conditions are required which are discussed in detail for solid walls. The chapter continues with the discussion of the implementation itself and ends with the validation of the stand-alone solution of the Rosseland equations.

4.1 The Coupling between NSMB and the Rosseland Radiation Model

For the coupling of the radiative heat transport with the fluid dynamics local thermodynamic equilibrium (LTE) is assumed and the time dependence of the radiative transfer equation is neglected. It follows from LTE that the temperature of the fluid and the corresponding radiative temperature of the medium are equal. Radiative heat transfer and fluid dynamics are only coupled within the equation for overall conservation of energy. It should be noted that photons carry momentum, thus causing radiation pressure and radiation stress [4]. However, these effects are generally negligible except at extremely high temperatures (> 50000 K at $\approx 10^5$ Pa) [82; 83] or in situations where the hydrodynamic pressure is close to vacuum [84]. Therefore, in this thesis the radiative pressure is neglected compared to the conventional fluid dynamic pressure. Hence, no coupling of the radiative heat transfer to the momentum equations of Navier-Stokes is necessary. The approximation of the radiative transfer equation via the Rosseland method has the advantage that the resulting radiative heat flux is of a diffusive type which can thus simply be added to the energy equation. At the iteration level n the evaluation of the heat conduction fluxes and the radiative fluxes is performed simultaneously from the same temperature distribution in the calculation domain. The time dependent energy equation of NSMB for viscous flows without chemical reactions is listed in Eq. (89)

$$\frac{\partial}{\partial t}(\rho E) = -\vec{\nabla} \cdot \left[\overbrace{(\rho E)\vec{V}}^{\mathrm{a}} + \overbrace{p\vec{V}}^{\mathrm{b}} + \overbrace{\underline{\underline{\tau}} \cdot \vec{V}}^{\mathrm{c}} + \overbrace{\vec{q}_{\mathrm{cd}}}^{\mathrm{d}} + \overbrace{\vec{q}_{\mathrm{r}}}^{\mathrm{e}} \right], \tag{89}$$

with the heat conduction according to Fourier's law

$$\vec{q}_{\mathrm{cd}} = -k_{\mathrm{cd}} \vec{\nabla} T, \tag{90}$$

and the Rosseland approximation of the radiative transfer equation

$$\vec{q}_{\mathrm{r}} = -k_{\mathrm{R}} \vec{\nabla} T \,, \tag{70}$$

with the radiative heat conductivity

$$k_{\mathrm{R}} = \frac{16 n^2 \sigma T^3}{3 a_{\mathrm{R}}} \,. \tag{69}$$

In this context term (a) represents the convective transport of energy, (b) the work on the fluid by pressure forces, (c) the dissipation work, (d) the heat conduction due to molecular diffusion and (e) the diffusive Rosseland radiation heat flux. Including radiation without modelling combustion means that the gas mixture is considered to be frozen. Depending on the desired complexity of the simulation, combustion modelling can be additionally added to Eq. (89). In Eq. (69) the refractive index n is assumed to be $n = c_0 / c \approx 1$ which is a suitable approximation for ordinary gas mixtures [4]. For the implemented Rosseland Radiation Model scattering is neglected because no suspended particles are considered in this thesis; see discussion of Eq. (34). Hence, only absorption and emission of the combustion gases is considered. The Rosseland mean absorption coefficient a_R is constant for gray gases; for non-gray gases the weighted-sum-of-gray-gases approach is employed in this thesis; see chapter 3.5. In order to test the Rosseland Radiation Model (RRM), the NSMB code is modified to provide a stand-alone solution of the RRM. For this purpose, radiative equilibrium is assumed for the absorbing and emitting gas mixture. This means that only radiation contributes to energy transfer and all other transfer modes (convection, conduction, viscous dissipation etc.) are excluded. Equation (89) is transformed to Eq. (91) where the total energy $E = e + 0.5\ (u^2 + v^2 + w^2)$ is substituted by the internal energy e, assuming a zero fluid velocity:

$$\frac{\partial}{\partial t}\left(\rho e\right) = 0 = -\vec{\nabla} \cdot \vec{q}_{\mathrm{r}} \,, \tag{91}$$

and the time dependent term on the left side vanishes because the problem is considered to be of a steady-state nature, i.e. ∂t tends to infinity. Equation (91) is identical in form to the basic steady-state heat conduction equation before substituting Fourier’s law. The minus sign on the right side of Eq. (91) is held for consistency reasons to the overall energy equation in Eq. (89) and to achieve a general finite volume approximation for both the stand-alone solution of the Rosseland Radiation Model (RRM) as well as the coupled solution together with the fluid dynamics. In the coupled solution of RRM and NSMB the negative divergence of the Rosseland radiative flux, $-\vec{\nabla} \cdot \vec{q}_{\mathrm{r}}$, is evaluated by the RRM subroutines and added to the NSMB array of total net fluxes.

4.2 Finite Volume Approximation of the Radiative Heat Flux

Adding the diffusive Rosseland radiation flux to the energy equation of NSMB requires a finite volume formulation of Eq. (91) in order to be consistent with the solution algorithm of NSMB [81]. In the finite volume approach, Eq. (91) is integrated over an arbitrary volume V and gives Eq. (92)

$$\iiint_V \frac{\partial(\rho e)}{\partial t}\, dV = \iiint_V -\vec{\nabla}\cdot\vec{q}_{\mathrm{r}}\, dV\,. \tag{92}$$

The unit of Eq. (92) is Watt and the divergence theorem of Gauss allows the transformation of the right-hand side of Eq. (92) to a surface integral, that is

$$\iiint_V \frac{\partial(\rho e)}{\partial t}\, dV = \iint_{\partial V} -\vec{q}_{\mathrm{r}}\cdot\vec{n}\, dS\,. \tag{93}$$

It is supposed that the arbitrary volume V is replaced by a discrete volume $V_{i,j,k}$ of a grid cell i,j,k and Eq. (93) can be written in terms of the finite volume discretisation as

$$\iiint_V \frac{\partial(\rho e)}{\partial t}\, dV \approx \frac{d}{dt}\Big[(\rho e)_{i,j,k}\;\; V_{i,j,k}\Big] \tag{94}$$

and

$$\iint_{\partial V} -\vec{q}_{\mathrm{r}}\cdot\vec{n}\, dS \approx -Q_{i,j,k} \tag{95}$$

where $Q_{i,j,k}$ is the net flux leaving and entering the grid cell i,j,k. NSMB is a structured CFD solver using only hexahedron cells for the approximation of the entire 3D calculation domain. Per definition, both the left lower corner of the 3D cell and the cell centre are addressed with the indices i,j,k as depicted in Fig. 7.

For radiative equilibrium, respectively a general steady state, the amount of energy which enters cell i,j,k must be equal to the sum which leaves the cell. Hence, the net flux $Q_{i,j,k}$ can be expressed as the sum of the heat fluxes over the six faces of a cell as

$$Q_{i,j,k} = q_{i+1/2,j,k} - q_{i-1/2,j,k} + q_{i,j+1/2,k} - q_{i,j-1/2,k} + q_{i,j,k+1/2} - q_{i,j,k-1/2}\,. \tag{96}$$

In Eq. (96) the term $q_{i-1/2,j,k}$ is defined as the heat flux oriented in the I-direction through the cell side ABCD; see Fig. 7. The minus sign before $q_{i-1/2,j,k}$, $q_{i,j-1/2,k}$ and $q_{i,j,k-1/2}$ results from the fact that the surface normals $\vec{n}$ at these surfaces are pointing in the inward direction of the corresponding cell.

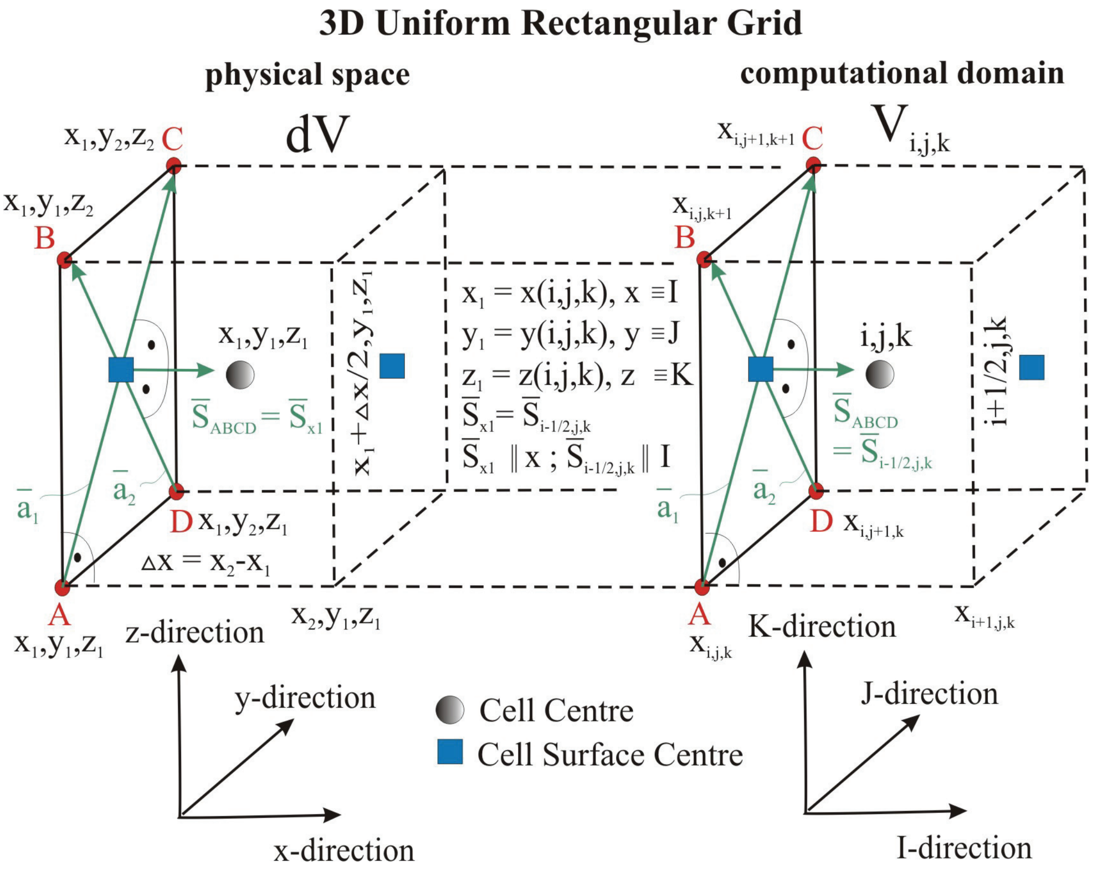

Figure 7: Interrelationship of physical space and computational domain for a 3D finite volume cell in NSMB

The radiative heat flux at cell side ABCD can be approximated as

$$q_{i-1/2,j,k} \approx \iint_{\text{ABCD}} -\vec{q}_r \cdot \vec{n}\, dS = -\vec{q}_r\Big|_{\text{ABCD}} \cdot \vec{S}^{I}_{\text{ABCD}} \tag{97}$$

with the surface normal vector $\vec{S}^{I}_{\text{ABCD}}$ in cartesian coordinates

$$\vec{S}^{I}_{\text{ABCD}} = \iint_{\text{ABCD}} \vec{n}\, dS = \frac{1}{2}\vec{a}_1 \times \vec{a}_2 = \frac{1}{2}\begin{vmatrix} \vec{e}_x & \vec{e}_y & \vec{e}_z \\ a_{1,x} & a_{1,y} & a_{1,z} \\ a_{2,x} & a_{2,y} & a_{2,z} \end{vmatrix} = \frac{1}{2}\begin{bmatrix} a_{1,y}a_{2,z} - a_{1,z}a_{2,y} \\ a_{1,z}a_{2,x} - a_{1,x}a_{2,z} \\ a_{1,x}a_{2,y} - a_{1,y}a_{2,x} \end{bmatrix} = \begin{bmatrix} S^I_x \\ S^I_y \\ S^I_z \end{bmatrix}. \tag{98}$$

The right-hand side of Eq. (97) can be construed as the heat flux $\vec{q}_r$ projected on the surface ABCD which corresponds to the radiative energy through surface ABCD per unit time and surface area of ABCD. The direction vectors $\vec{a}_1$ and $\vec{a}_2$ are given by

$$\vec{a}_1 = \begin{bmatrix} a_{1,x} \\ a_{1,y} \\ a_{1,z} \end{bmatrix} = \begin{bmatrix} x_{i,j+1,k+1} - x_{i,j,k} \\ y_{i,j+1,k+1} - y_{i,j,k} \\ z_{i,j+1,k+1} - z_{i,j,k} \end{bmatrix}, \quad \vec{a}_2 = \begin{bmatrix} a_{2,x} \\ a_{2,y} \\ a_{2,z} \end{bmatrix} = \begin{bmatrix} x_{i,j,k+1} - x_{i,j+1,k} \\ y_{i,j,k+1} - y_{i,j+1,k} \\ z_{i,j,k+1} - z_{i,j+1,k} \end{bmatrix}. \tag{99}$$

The interrelationship between the physical x, y, z and numerical i, j, k coordinate system is illustrated in Fig. 7. Using multiple structured blocks allows the handling of arbitrary shaped, complex geometries, with the user having to generate the mesh heuristically, which requires a greater effort in contrast to unstructured grids. The surface normal vectors $\vec{S}$ in the J- and K-directions are evaluated analogue to the I-direction above. For a final evaluation of the net heat flux $Q_{i,j,k}$ in Eq. (96) the radiative heat flux $\vec{q}_r$ in Eq. (97) must be approximated at each of the six cell surface centres of cell i, j, k. It is important to keep in mind that the quantity $Q_{i,j,k}$ is defined at the cell centre and $\vec{q}_r$ is defined at the corresponding cell surface centres of grid cell i, j, k. To calculate $\vec{q}_r$ directly at the surface cell centre according to Eq. (70), the radiative conductivity k_R is extrapolated to the surface centre and the temperature gradient $\vec{\nabla} T$ is calculated directly at the surface centre. For this purpose, the gradient theorem allows the calculation of the temperature gradients with the finite volume approach.

$$\vec{\nabla} T = \frac{\iiint_{V_{i,j,k}} \vec{\nabla} T dV}{\iiint_{V_{i,j,k}} dV} = \frac{1}{V_{i,j,k}} \iint_{\partial V_{i,j,k}} T \vec{n} \, dS \tag{100}$$

Equation (100) exemplarily shows the application of the gradient theorem to one finite volume cell with the discrete volume $V_{i,j,k}$. The volume integral is again transformed to a surface integral as shown in Eqs. (93) and (100), and is applied to a shifted mesh as depicted in Fig. 8. At the cell corners the value for the temperature is obtained using the average at the neighbouring cells. Near boundaries the first rows of ghost cell values are filled in such a way that the temperature gradient is calculated using the user imposed wall-temperature values.

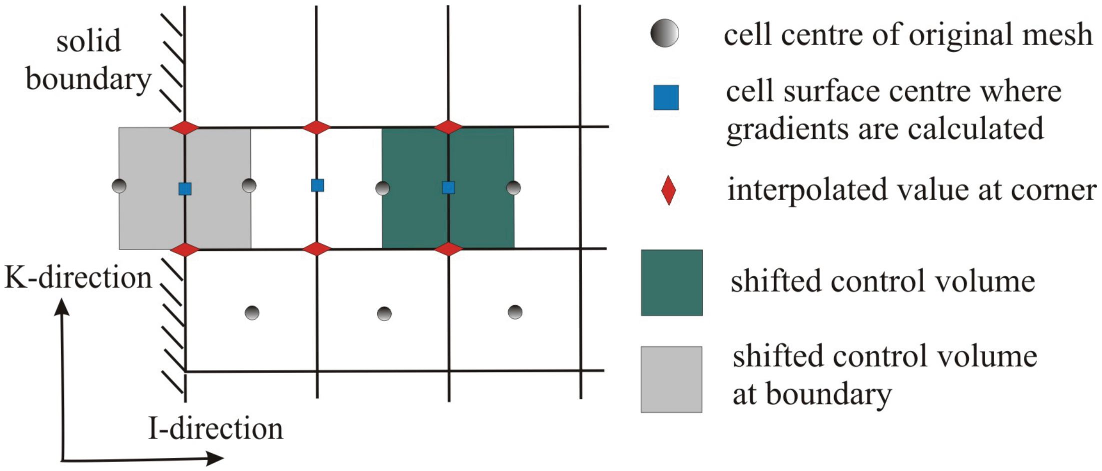

Figure 8: Shifted control volume used for the calculation of scalar gradients, based on [81]

4.3 Boundary Conditions of the Rosseland Radiation Model (RRM)

For the Rosseland Radiation Model (RRM) only the boundary condition for solid walls needs to be specified by the user. It is possible to define an adiabatic boundary condition, i.e. a zero-temperature gradient at the solid wall or a specific wall temperature. This imposed wall temperature is either used directly for the Dirichlet boundary condition or indirectly for the calculation of the jump boundary condition.

4.3.1 Dirichlet Boundary Condition

Within the NSMB CFD solver boundary conditions are imposed using ghost cells which are added outside the computational domain where the flow equations are not solved. Physical boundary conditions (e.g. fixed temperature) require only one ghost cell, whereas two ghost cells are needed for numerical boundary conditions (e.g. artificial dissipation). For the RRM only one ghost cell is required to calculate the wall heat flux based on the user defined wall temperature. This type of boundary specification is commonly called Dirichlet boundary equation, in contrast to the Neumann boundary condition where the gradient of the scalar is specified at the boundary. Before the wall heat flux is calculated the wall temperature is extrapolated to the first ghost cell. Appendix A shows the initialisation of the temperature field including ghost cells after setting the boundary conditions and before calculating the heat fluxes. The wall heat flux from cell $(1,1)$ to the solid wall is calculated from the temperature difference of $T(1,1)$ and $T_{ex}(1,0)$.

4.3.2 Jump Boundary Condition

The Rosseland approximation of the RTE works well in the interior of the computational domain, but is not accurate near boundaries except for an extremely large optical thickness. For a gray medium at radiative equilibrium between isothermal plates Heaslet & Warming [85] showed that a temperature jump occurs as depicted in Fig. 9. One can observe that the smaller the optical thickness κ_D the higher the magnitude of the temperature jump. The fact that the gas temperature T_i adjacent to a wall differs from the wall temperature T_w can be physically interpreted as follows: the radiative heat flux coming from the gas in the interior is denoted with q_rg. This flux results from the Rosseland approximation, Eq. (70), and is only valid in the gas, i.e. includes only the infinitesimal gas layer but not the solid wall as depicted in Fig. 10. The radiative heat flux between the solid wall and the infinitesimal gas layer, q_rw, is approximated by the jump condition. The infinitesimal gas layer is assumed to be on average a radiation mean free path, $\Delta\mathrm{gw}$, away from the solid wall. Thus, the average temperature T_ju of the radiation passing through the infinitesimal gas layer lies between the wall temperature T_w and the temperature T_i of the interior gas. This effect is similar to the temperature slip next to a wall which occurs in heat transfer by conduction in rarefied gases. In this thesis the jump boundary condition concept by Deissler [68] is modified to derive a suitable jump temperature.

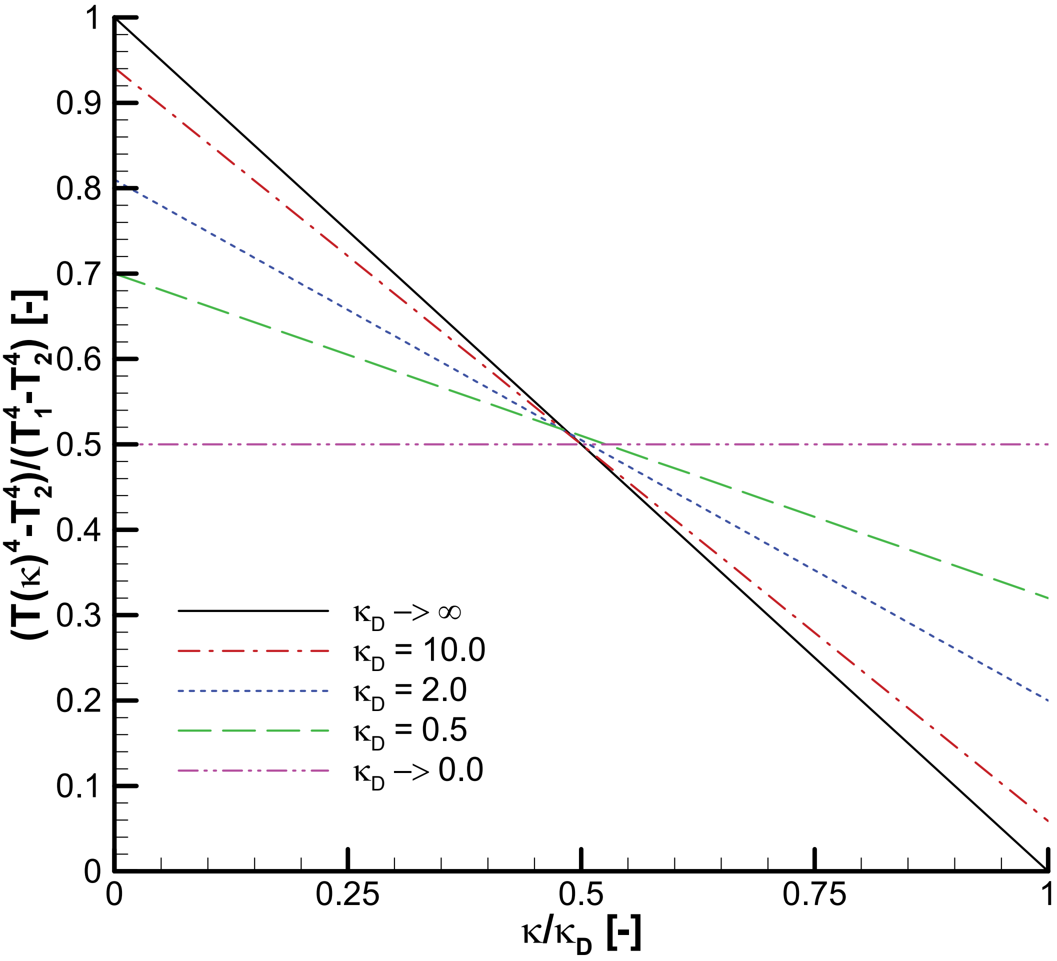

Figure 9: Dimensionless temperature distribution in gray medium contained between infinite black parallel plates, based on [85]

To calculate a physical feasible jump temperature, a one-dimensional radiative energy balance for an infinitesimal gas layer adjacent to the solid wall in Fig. 10 is regarded, and delivers:

$$q_{\mathrm{rg}} = q_{\mathrm{rw}} . \tag{101}$$

The radiative energy balance in Eq. (101) does not contain heat conduction and/or convection, since the jump boundary condition only relates the radiative heat flux from the gas, to the corresponding solid wall boundary. The solid wall boundary conditions for the other modes of heat transfer (heat conduction, convection, mass diffusion, etc.) are set separately, as usual for the finite-volume approach [81].

The linearised one-dimensional Rosseland net heat flux q_{rg} for a gray medium from the interior gas, normal to the infinitesimal gas layer near the wall follows from Eq. (70); it is

$$q_{\text{rg}} = -\frac{16}{3}\frac{\sigma}{a_{\text{R}}}T^3\frac{dT}{dn}. \tag{102}$$

The infinitesimal gas layer close to the wall can be regarded as a virtual boundary condition for the Rosseland net radiative heat flux. For the radiative net flux q_{rw} from the infinitesimal gas layer to the solid wall Deissler's [68] original approach is simplified to a first order boundary condition and gives

$$q_{\text{rw}} = -\frac{\sigma\left(T_{\text{ju}}^4 - T_{\text{w}}^4\right)}{\frac{1}{\varepsilon_{\text{w}}} - \frac{1}{2}}. \tag{103}$$

The simplification from second to first order results from the assumption that the gas is gray and therefore Siegel & Howell [5] show that the second-derivative terms are zero in the boundary-condition equations. In Eq. (103) it is assumed that the solid wall is radiating diffuse and gray, hence, the jump boundary condition can be applied to non-black boundaries.

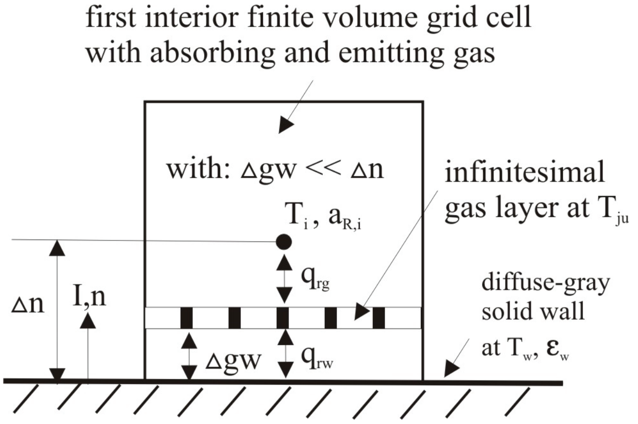

Figure 10: Temperature jump between infinitesimal gas layer and diffuse-gray wall

Equations (102) and (103) give:

$$-\frac{16}{3}\frac{\sigma}{a_{\text{R}}}T^3\frac{dT}{dn} = -\frac{\sigma\left(T_{\text{ju}}^4 - T_{\text{w}}^4\right)}{\frac{1}{\varepsilon_{\text{w}}} - \frac{1}{2}}. \tag{104}$$

The temperature gradient dT/dn in Eq. (104) relates the interior gas, where the Rosseland approximation is valid, to the infinitesimal gas layer immediately adjacent to the wall. The temperature gradient is approximated as

$$\frac{dT}{dn} \approx \frac{T_{\text{i}} - T_{\text{ju}}}{\Delta n}. \tag{105}$$

The terms a_R and T^3 in Eq. (104) are assumed as the average values of the first interior grid cell, i.e. $a_\mathrm{R} \approx a_\mathrm{R,i}$ respectively $T^3 \approx T_\mathrm{i}^3$. For the jump temperature follows the implicit relation

$$T_\mathrm{ju}^4 = T_\mathrm{w}^4 + \frac{16}{3} \frac{\frac{1}{\varepsilon_\mathrm{w}} - \frac{1}{2}}{a_\mathrm{R,i}} T_\mathrm{i}^3 \left(\frac{T_\mathrm{i} - T_\mathrm{ju}}{\Delta n} \right). \tag{106}$$

To calculate the jump temperature T_ju Eq. (106) is solved iteratively for each cell near the wall using a Newton-Raphson [86] based method. After the calculation of the jump temperature it is extrapolated into the first ghost cell ($T_\mathrm{ghost} = 2 \cdot T_\mathrm{ju} - T_\mathrm{i}$), and the net radiative wall heat flux of the Rosseland Radiation Model is proportional to the temperature difference $\left|T_\mathrm{i} - T_\mathrm{ghost}\right| / (2 \cdot \Delta n)$ which is equivalent to $\left|T_\mathrm{i} - T_\mathrm{ju}\right| / (\Delta n)$; see shifted control volume at boundary in Fig. 8.

4.3.3 Effective Jump Boundary Condition

In [5] it is concluded that Eq. (106) is only valid for pure radiation from a mathematical perspective. Indeed, the numerical simulations of the SSME main combustion chamber, performed with NSMB and applying Eq. (106) show a non-satisfying qualitative distribution of the radiative wall heat flux. Therefore, an effective jump boundary condition according to Goldstein & Howell [69] is introduced and modified in this thesis.
The jump coefficient ψ at the wall by Deissler's [68] original approach is defined as

$$\psi = \frac{1}{\varepsilon_\mathrm{w}} - \frac{1}{2}. \tag{107}$$

Equation (107) shows that for a black wall, i.e. $\varepsilon_\mathrm{w} = 1$, ψ reaches a value of 1/2. Goldstein & Howell [69] introduce an effective jump coefficient $\psi_\mathrm{eff} = f(N)$ as a function of the conduction-radiation parameter N_w, which is defined as

$$N_\mathrm{w} = \frac{k_\mathrm{cd,i}\, a_\mathrm{R,i}}{4\, \sigma\, T_\mathrm{w}^3} \sim \frac{k_\mathrm{cd}}{k_\mathrm{R}}, \tag{108}$$

where $k_\mathrm{cd,i}$ is the thermal heat conductivity of the first interior cell and σ is the Stefan-Boltzmann constant. The effective jump coefficient $\psi_\mathrm{w,eff}$ at the wall is computed in the original approach by Goldstein & Howell [69] as

$$\psi_\mathrm{w,eff} = \frac{3}{4\pi} \int_0^1 \tan^{-1}\left(\frac{1}{\psi(\gamma)} \right) d\gamma \text{, where } \psi(\gamma) = \frac{1}{\pi}\left(\frac{N_\mathrm{w}}{2\gamma^3} - \frac{2}{\gamma} - \ln\frac{1-\gamma}{1+\gamma} \right). \tag{109}$$

The relation in Eq. (109) is valid only for black walls, hence it follows from Eq. (107) that the maximal value of ψ_{eff} is 1/2. $\psi_{\mathrm{w,eff}}$ has the following solution set

$$\psi_{\mathrm{w,eff}} = \begin{cases} 1/2 & N_{\mathrm{w}} < 0.01 \\ \psi_{\mathrm{w,eff}}(N_{\mathrm{w}}) & 0.01 \le N_{\mathrm{w}} \le 10 \\ 0 & N_{\mathrm{w}} > 10 \end{cases}. \tag{110}$$

Equation (109) is valid in the presence of radiation and conduction only. In the scope of this thesis, there is a weak interaction of forced convection and turbulence with radiation, regarding the simulation of the SSME main combustion chamber. Parameter studies show that Eq. (109) leads to unphysical results for the wall quantities. This results from the fact that N_{w} is very small in the SSME main combustion chamber. Hence, $\psi_{\mathrm{w,eff}}$ tends to its maximal value of 1/2, see Eq. (110). The maximum value of $\psi_{\mathrm{w,eff}} = 1/2$ indicates physically that only radiation is present which is in fact not the case. The following relation is found empirically to produce better results in terms of quality for the SSME main combustion chamber:

$$\psi_{\mathrm{w,eff}} = \psi_{\mathrm{User}} \cdot N_{\mathrm{w}}. \tag{111}$$

In Eq. (111), ψ_{User} is heuristically defined by the user for the current CFD problem. In this thesis it was found that ψ_{User} can be numerically approximated by

$$\psi_{\mathrm{User}} \approx 1.3 \cdot 10^{-2} \cdot \left(\frac{1}{\varepsilon_{\mathrm{w}}} - \frac{1}{2} \right), \tag{112}$$

with a wall emissivity of $\varepsilon_{\mathrm{w}} \approx 0.7$. Equation (112) should be used carefully and only as a first guess as it is problem dependent. By [70] it is confirmed that for a coupled radiation-flow dynamics problem it is still not clear how to apply realistic boundary conditions for the Rosseland Radiation Model. Therefore, Eqs. (111) and (112) are assumed to represent a good compromise between accuracy and numerical stability for the SSME main combustion chamber. Taking into account the introduced modifications, Eq. (106) can now be rewritten as

$$T_{\mathrm{ju}}^4 = T_{\mathrm{w}}^4 + \frac{16}{3} \frac{\psi_{\mathrm{w,eff}}}{a_{\mathrm{R,i}}} T_{\mathrm{i}}^3 \left(\frac{T_{\mathrm{i}} - T_{\mathrm{ju}}}{\Delta n} \right), \tag{113}$$

and is used for the SSME main combustion chamber simulations with the NSMB CFD solver.
It should be noted that the use of the Rosseland model with the unchanged jump boundary condition in Eq. (109) is not possible due to stability problems as a CFX-Rosseland investigation shows. In contrast, the modified jump boundary condition in Eq. (113) allows on the one hand a stable calculation and on the other hand reproduces qualitatively good results.

4.4 Discussion of the Implementation

In the subchapter above the theory of the Rosseland Radiation Model (RRM) is described in detail whereas in this subchapter the implementation into the NSMB CFD solver is elucidated. The NSMB research software is still under development and a detailed description of the code is given in [81; 87]. To reduce the effort of migration from previous to subsequent versions, the original infrastructure of NSMB is used as much as possible. As already mentioned, only the energy equation of NSMB is expanded; it includes the contribution of the diffusive Rosseland heat fluxes. The contribution of the radiative pressure is orders of magnitude smaller compared to the hydrostatic pressure of the fluid and is neglected in the momentum equations [4]. The RRM can be used with both explicit and implicit time-stepping schemes. It is possible to evaluate a solution only for radiative equilibrium (stand-alone case), i.e. convection, heat conduction, viscous dissipation and chemical source terms are neglected. On the other hand, a fully coupled solution of gas radiation and the other modes of heat transfer is possible. Due to the diffusive nature of the Rosseland approximation the energy equation is solved simultaneously for radiation and hydrodynamics. The Rosseland implementation is designed only for steady-state NSMB simulations. Figure 11 gives an overview of the modified subroutines and the interaction of radiative subroutines with the original source code. A more detailed description of the implementation is available in the NSMB Wiki [88].

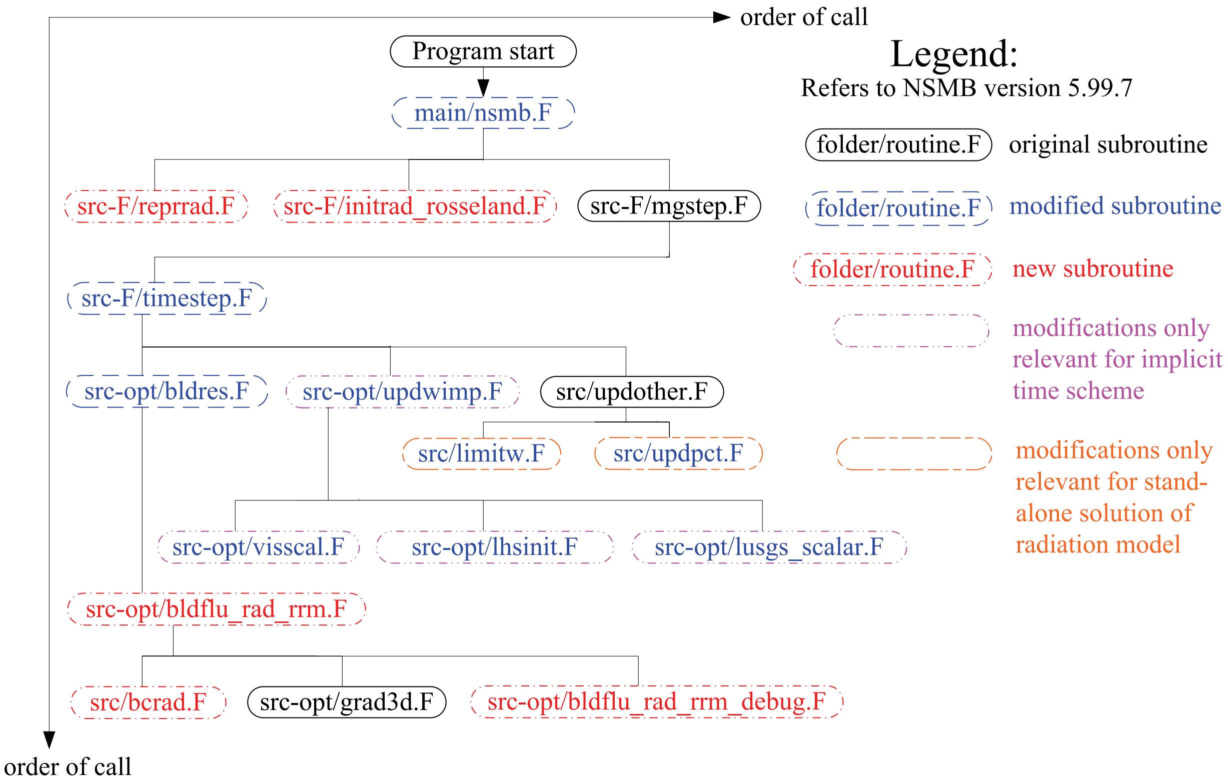

Figure 11: Flowchart of the Rosseland Radiation Model (RRM) in NMSB

After the program start the user input is read from *reprrad.F*. In *initrad_rosseland.F* all initialisation issues for the RRM are accomplished. It is important that this subroutine is also called when radiation is not activated in order to allocate the Rosseland specific arrays. The intersection from *timestep.F* to *bldres.F* represents the transition from global to local arrays, i.e. the second subroutine *bldres.F* and the subsequent subroutines only calculate values for a local block. In this context, all global radiative variables are configured by the defined addresses and passed to their local counterpart.

The next subroutine, *bldflu_rad_rrm.F*, represents the main algorithm of the Rosseland Radiation Model. This subroutine calculates the Rosseland net heat flux for a finite volume cell and adds it to the array of the total residual of NSMB's energy equation. In *bcrad.F* the boundary conditions for the RRM are set. For solid walls with a Dirichlet boundary condition the wall temperature is extrapolated into the first ghost cell and for a jump temperature boundary condition the jump temperature is calculated and also extrapolated into the first ghost cell. For adiabatic solid walls the temperature in the first ghost cell is set to the first interior cell. Symmetry surfaces, respectively singularities are treated as adiabatic solid walls for the RRM only. No explicit boundary conditions are set for inlet and outlet boundaries. For this type the temperature gradients at the boundary are calculated from the local temperatures resulting from the flow solution. For each of the three geometrical coordinate directions the following steps are carried out: first *grad3d.F* calculates the temperature gradients directly on the cell surface centre as illustrated in Fig. 8. In the second step the variables of radiative properties are extrapolated to the cell surface centre where the radiative heat flux in the ongoing direction is calculated. In the last step the net flux of all directional fluxes is accumulated for each cell and gives the radiative residual which is added to the residual of the overall energy equation.

The call of *bldres.F* is carried out for the explicit as well as the implicit time-stepping-schemes. For the explicit time scheme no further modifications considering the RRM implementation are necessary. As has been shown in [87] the implicit method can become unstable for diffusion-dominated problems if the diffusive terms are not included in the implicit operator. As described before, the RRM can become strongly diffusive for high temperatures and partial pressures. It was observed that applying the implicit time-stepping-scheme for the Rosseland approximation ensures stability and improves the convergence of a simulation. For this purpose, the viscous Jacobian matrices are expanded in the scope of this thesis and supplemented in subroutine *visscal.F*.

4.5 Validation of the Stand-Alone Solution of the Rosseland Radiation Model

This chapter describes on the one hand the verification of the Rosseland Radiation Model implementation into the NSMB CFD code and on the other hand the quality of the results compared to an analytical solution by Heaslet & Warming [85]. The stand-alone solution means that a steady-state gas in radiative equilibrium is considered, i.e. all other energy transfer modes are neglected. For this task a caloric perfect gas under atmospheric pressure is used with an inviscid steady flow without chemical heat sources, hence NSMB formally solves the Euler equations. To arrange radiative equilibrium the residual of the convective fluxes is set to zero in each time step before calculating the total residual of the overall energy equation. Therefore, NSMB solves the remaining elliptic equation given in Eq. (91).

4.5.1 Definition of the Test Case

A two dimensional, square geometry with an edge length of one meter is used to model a gas in radiative equilibrium between two black walls; see Fig. 12. The boundary condition of RRM is also valid for gray walls, but for consistency reasons with the analytical solution the walls for this test case are black. The calculation domain is discretised by finite volume cells as one structured block. For a two-dimensional calculation with NSMB at least two cells in K-direction are required. Different mesh densities are used, whereas in the following only solutions from the finest grid with 100x100 cells are presented.

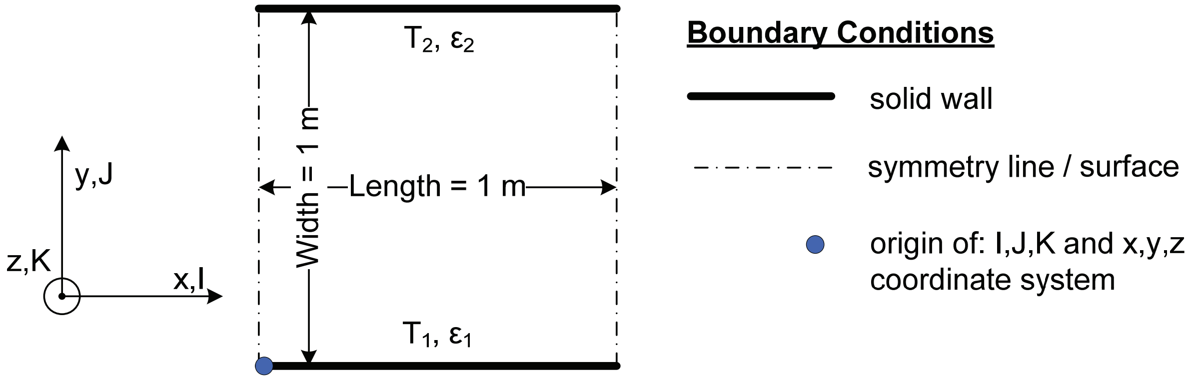

Figure 12: Geometry for the validation of the RRM standalone version

The calculation domain is initialised with an atmospheric pressure and a temperature of 300 K and the parameters of Tab. 1 are used for the radiative description. For the solid wall both Dirichlet and jump temperature boundary conditions are investigated. In case of the symmetry line, the boundary condition for the Rosseland Radiation Model (RRM) corresponds to an adiabatic boundary condition, i.e. a zero temperature gradient at the boundary.

Table 1: Parameters for the validation of the RRM stand-alone version

Parameter	Value	Description
T_1 [K]	600	Wall temperature
T_2 [K]	300	Wall temperature
$\varepsilon_1 = \varepsilon_2$ [-]	1	Wall emissivity
κ_D [-]	10	Optical thickness, with $D = 1$ m
a [1/m]	10	Total absorption coefficient

4.5.2 Results

The results of the CFD simulation with NSMB for the stand-alone solution of the Rosseland Radiation Model are presented in Fig. 13 and compared with an analytical solution by Heaslet &

Warming [85]. The result for the Dirichlet boundary condition is represented precisely by the curve for the optical thickness of $\kappa_D \rightarrow \infty$. The numerical result for the jump boundary condition is more interesting. It is observed that the implemented jump boundary condition from Eq. (106) delivers meaningful physical results for $\kappa_D \geq 10$ only. For a typical rocket combustion chamber an optical thickness of greater than 10 as listed in Tab. 10 of chapter 6.4.3 is a good assumption. As depicted in Fig. 13 the numerical result of the jump boundary condition fits quite well to the analytical result. The absolute temperature difference between analytical and numerical solution for $\kappa/\kappa_D \rightarrow 0$ is 0.14 % and 6.26 % for $\kappa/\kappa_D \rightarrow 1$.

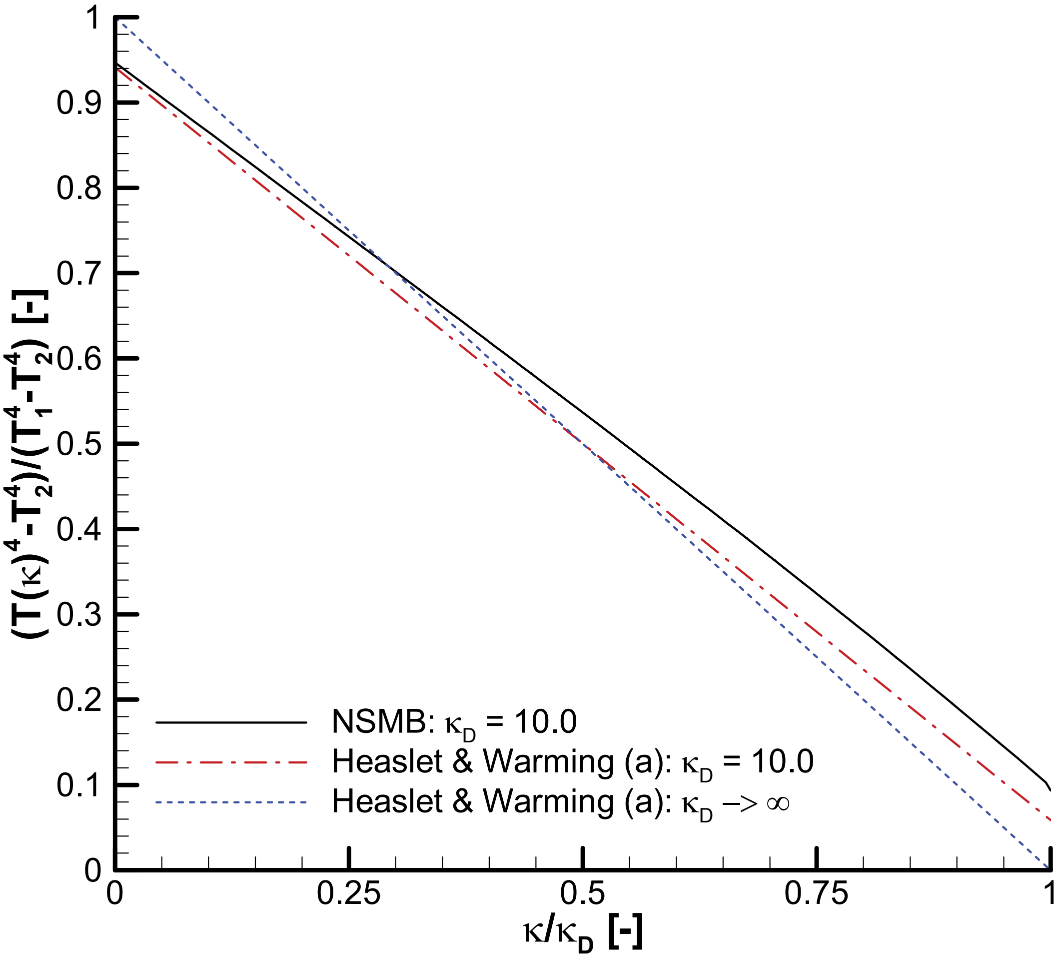

Figure 13: Temperature distribution on gray medium between infinite black parallel plates as a function of the ratio of optical thickness; (a) = [85]

An iterative method is said to be converged if the error $er^n = W^n - W_{\text{exact}}$ tends to zero as the number of time steps approaches infinity, where W_{exact} is the exact solution of the problem. In practical computations it is not possible to use the error er^n as a convergence criterion since the exact solution is in generally unknown. Therefore, in NSMB the L_2-norm of the residual is used as a measure of the rate of convergence. When using the explicit time stepping scheme the L_2-norm at the time step n is calculated as:

$$\left\|\mathrm{Res}^n\right\|_{L_2} = \sqrt{\sum_{i,j,k}\left[\left(\frac{\Delta W_{i,j,k}}{\Delta t_{i,j,k}}\right)^2 V_{i.j.k}\right]} \tag{114}$$

where $W_{i,j,k}$ stands for the ρE component of the state vector; see Eq. (2). The term $\Delta W_{i,j,k} = W^n_{i,j,k} - W^{n-1}_{i,j,k}$ represents the difference for ρE between the current timestep to the previous one. The computation is terminated when the L_2-residual is reduced by a predetermined number of orders of magnitude:

$$\left\|\mathrm{Res}^n\right\|_{L_2} < \varepsilon \cdot \left\|\mathrm{Res}^1\right\|_{L_2} \tag{115}$$

where $\left\|\mathrm{Res}^1\right\|_{L_2}$ is the residual at the first iteration. The user specifies the value of the convergence parameter ε, where $\varepsilon = 10^{-5}$ is a typical value for engineering purposes. Care must be taken regarding the convergence ε. A very small ε value does not automatically mean that a calculation is converged physically meaningful. A "converged" solution should always be checked by visualisation of the solution variables. From Eq. (115) follows that for an initialisation very close to the exact solution ε will not necessarily decrease in the order of magnitude of 10^{-5}. Nevertheless, the solution can be regarded as converged when the corresponding solution variable does not change anymore as a function of the number of iterations. For the implicit time stepping scheme the time step generally increases significantly during the computation. Therefore, the L_2-norm of the residual is calculated as follows when using the implicit time scheme [81]:

$$\left\|\mathrm{Res}^n\right\|^{\mathrm{imp}}_{L_2} = \sqrt{\sum_{i,j,k}\left[\frac{R^2_{i,j,k}}{V_{i.j.k}}\right]} \tag{116}$$

where $R_{i,j,k}$ corresponds to the net radiative heat fluxes given on the right side of Eq. (95). To investigate the performance of the solution algorithm for the Rosseland Radiation Model (RRM), Fig. 14 illustrates the convergence ε for different conditions. Although not all curves reach a convergence in the order of magnitude of 10^{-5}, all calculations in Fig. 14 are "converged". It can be observed that the implicit scheme performs better compared to the explicit method. This results from the much higher local timestep for the implicit method. The local timestep of the implicit SSOR method reaches the magnitude of order of $10^{16}\ s$. The local timestep of the explicit five stage Runge-Kutta method is in the order of magnitude of $10^{-2}\ s$. When the radiative conductivity is variable, i.e. calculated according to Eq. (69), the convergence rate is better compared to a constant value of k_{R}. This results from the fact the transport term in the differential equation, Eq. (70), is higher due to the variable k_{R}. A higher local transport term means that higher local net fluxes are possible, inducing a faster equilibrium state of the gas. The jump boundary condition needs more iterations to converge due to the additional subiterations for calculating the jump temperature for each near wall cell.

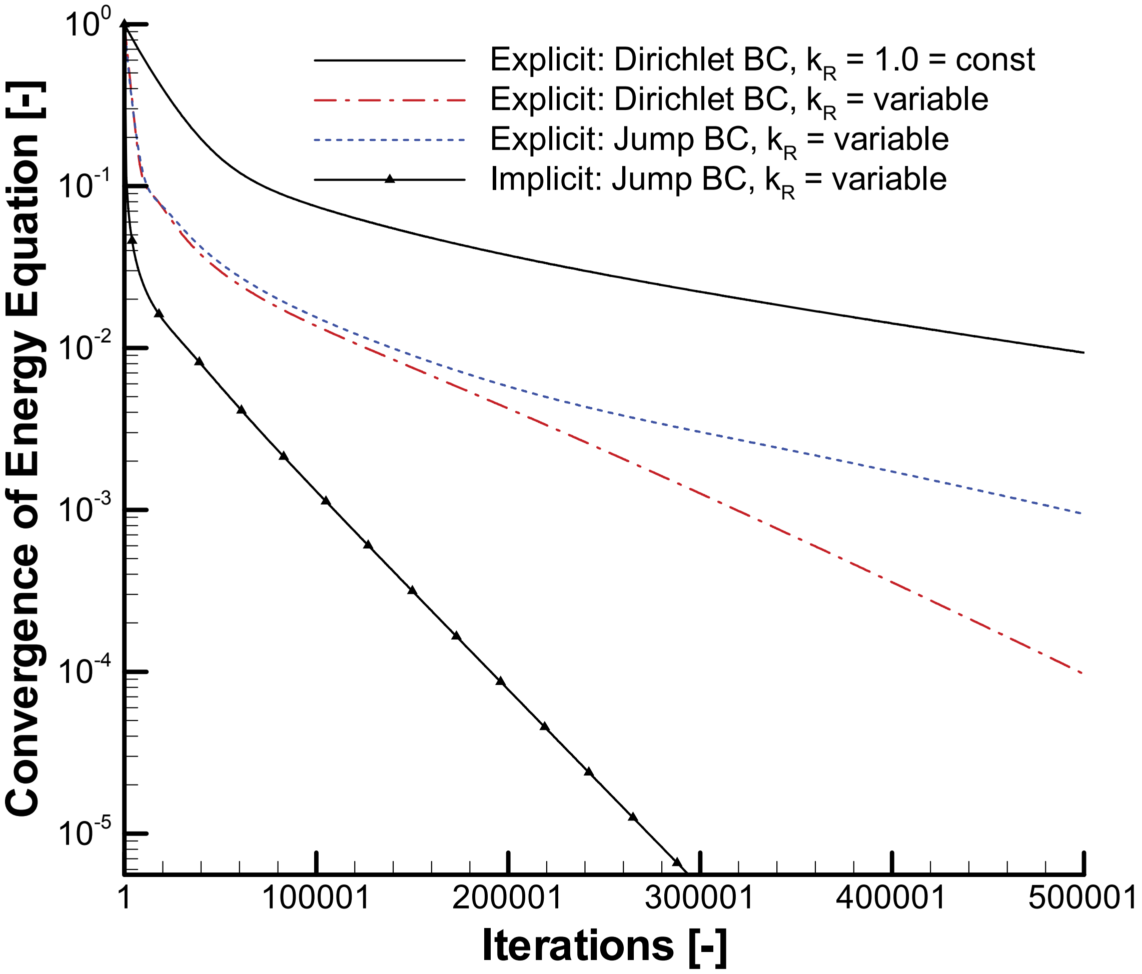

Figure 14: Convergence of the Rosseland Radiation Model (RRM) stand-alone version

5 Implementation of the Weighted Sum of Gray Gases Model

5.1 The Coupling between NSMB and the WSGG Model

The basic task of the weighted-sum-of-gray-gases model (WSGGM) is to provide the absorption coefficients a_i and the weighting factors w_i for each time step which are required in the sum of Eq. (88) for the calculation of the Rosseland radiative heat flux. The coupling between the CFD code and the WSGG model is accomplished by the pressure and temperature of the gas mixture and the molar fraction of the radiating species. In this study two typical rocket combustion systems are considered: H_2-O_2 and CH_4-O_2. Within the first system only H_2O is considered as the main radiating species and in the second system a mixture of H_2O and CO_2 contributes to thermal radiation. Regarding Eq. (72), the molar fraction X_{H_2O} and/or X_{CO_2} is required as an input for the WSGG model.

Figure 15 illustrates the new and modified subroutines for the implementation of the WSGG model into the NSMB CFD solver. After the initialisation of the WSGG variables in *initrad_spectral.F* the subroutine *wsggm.F* is called for the first time, calculating the absorption coefficients a_i and weights w_i. Depending on the selected gas and combustion model of NSMB the molar fractions of H_2O and/or CO_2 are constant (frozen flow) or calculated assuming chemical equilibrium or chemical non-equilibrium, if necessary. Currently chemical equilibrium is not available for the H_2-O_2 and CH_4-O_2 system respectively. Before the radiative heat fluxes according to Eq. (88) are evaluated, *wsggm.F* is called from *bldres.F* and a_i and w_i are calculated as a function of the current pressure, temperature of the gas and molar fraction of the radiating species.

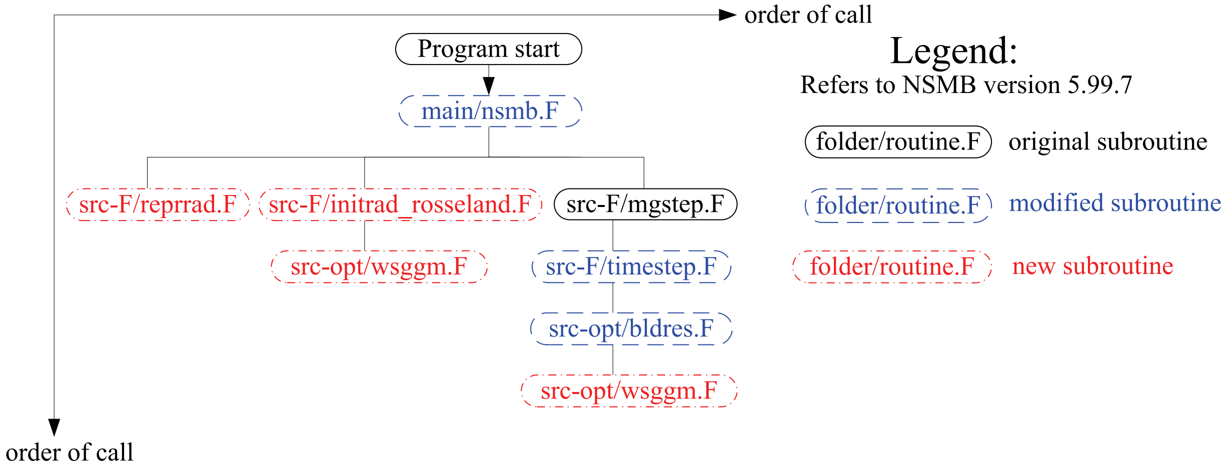

Figure 15: Flowchart of the WSGG model in NSMB

5.2 Comparison of the Weighted Sum of Gray Gases Model with EBCOW

For the implementation of the WSGG models into the NSMB CFD solver a numerical validation within the CFD code is not necessary because of the analytic characteristics of the WSGG approach. The WSGG models are stand-alone validated from the corresponding authors against measured total gas emissivities and/or compared to accurate results from a line-by-line database, e.g. HITRAN [77]. To compare the results from different WSGG models, Göbel [89] developed a tool named "Excel Based Comparison of WSGG models" (EBCOW). This tool calculates the total gas emissivity of a radiatively participating single gas or gas mixture for the input values of pressure, temperature range, molar fraction of the radiating species and characteristic path length.

Currently, the WSGG models by Smith et al. [79], Coppalle [90], Johansson [91] and the spectral-line-weighted-sum-of-gray-gases model (SLWSGGM) of Denison & Webb [72; 75; 76] are implemented in EBCOW, respectively NSMB. Except for Johansson [91] all WSGG models are also implemented by Birgel [92] in ANSYS CFX. The limitations of the WSGG models and the allocation to the corresponding combustion system within this thesis are listed in Tab. 2.

Table 2: Overview and Limitations of the (SL-)WSGG models

Source	Combustion System	Radiating Species	Temperature Regime	Reference Pressure
Smith [79]	H_2-O_2	H_2O	600K ≤ T ≤ 2400K	1 atm
Denison [72]	H_2-O_2	H_2O	500K ≤ T ≤ 2500K	1 atm
Denison [76]	H_2-O_2	H_2O	500K ≤ T ≤ 2500K	100 atm
Johansson [91]	CH_4-O_2	CO_2, H_2O	500K ≤ T ≤ 2500K	60 atm
Coppalle [90]	CH_4-O_2	CO_2, H_2O	2000K ≤ T ≤ 3000K	1 atm
Denison [75]	CH_4-O_2	CO_2, H_2O	500K ≤ T ≤ 2500K	1 atm
Denison [75]	CH_4-O_2	CO_2, H_2O	500K ≤ T ≤ 2500K	100 atm

5.2.1 Total Gas Emissivity at Atmospheric Pressure

Figure 16 shows the total gas emissivity of water vapour as single radiating species for a partial pressure path length of $p_{\mathrm{H_2O}} \cdot S = X_{\mathrm{H_2O}} \cdot p \cdot S = 1.0\ \mathrm{atm\,m}$, with $X_{\mathrm{H_2O}} = 1.0$, $p = 1.0\ \mathrm{atm}$ and $S = 1.0\ \mathrm{m}$. Figure 16 reveals that Denison's model using 10 and 20 gray spectral bands gives a good approximation of the total gas emissivity provided by the data over the entire temperature range. Differences between Denison's model for three gray bands compared to the model for 10 and 20 gray bands are significant, as the model for three gray bands underestimates the experimental data. The differences between Denison's model for 10 and 20 gray bands are small and both models estimate nearly the same value for total emissivity. Smith's model provides a good approximation of his own data [79] up to temperatures of 2000 K.

If additionally carbon dioxide is present, the total gas emissivity must be calculated as function of both radiating species, H_2O and CO_2. Figure 17 shows a fictitious test case with a partial pressure path length of $(p_{H_2O} + p_{CO_2}) \cdot S = (X_{H_2O} + X_{CO_2}) \cdot p \cdot S = 1.0 \text{ atm m}$, with $X_{H_2O} = X_{CO_2} = 0.1$ and an inert gas fraction of $X_{\text{inert}} = 0.8$, $p = 1.0 \text{ atm}$ and $S = 5.0 \text{ m}$. The total gas emissivity is calculated according to Eq. (71). In contrast to the H_2O investigations in Fig. 16, Denison's model is examined only for three and 10 gray bands as it has been shown that there is no significant difference between Denison's model for 10 and 20 gray bands [89]. In Fig. 17 it becomes obvious that Coppalle's model approximates the experimental data best over the entire temperature range, whereas above 2000 K it matches the data nearly exactly. Smith's model is slightly below Coppalle's model although differences are small below 1400 K. Johansson's model and Denison's model for three gray bands underpredict the values of total emissivity, whereas Johansson's values are slightly below Denison's for 10 gray bands.

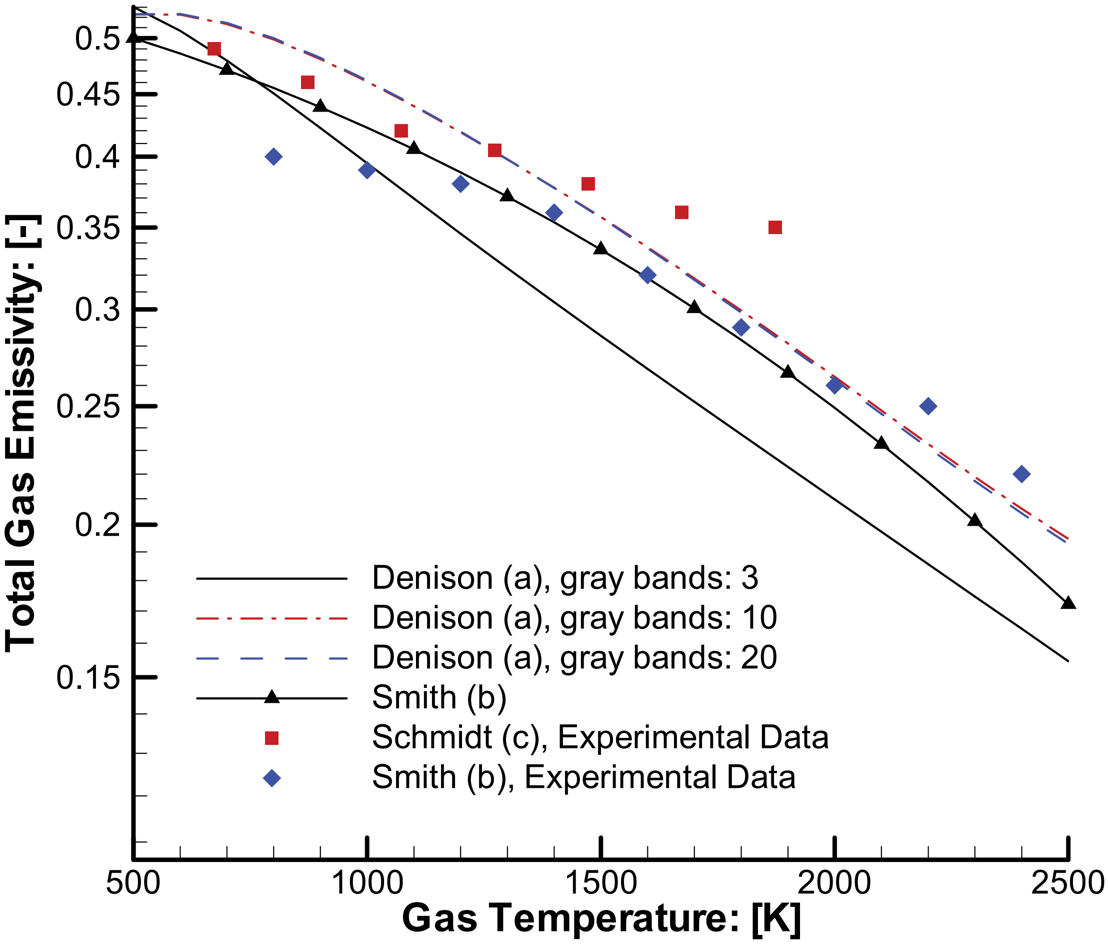

Figure 16: Comparison of WSGG models for H_2O at a partial pressure path length of 1.0 atm m; (a) = [72], (b) = [79] and (c) = [93]

The gas temperature in Figs. 16 and 17 ranges from 500 - 2500 K, resulting from the limitations of the WSGG models. All WSGG models illustrated in Figs. 16 and 17 are evaluated under atmospheric pressure, i.e. $p = 1 \text{ atm}$. For higher gas-pressures, scaling rules are given in [76]. Figures 16 and 17 reveal that for an increasing temperature total gas emissivity decreases. This follows from the fact that an increase in temperature under constant pressure leads to a decrease of the gas density. A lower gas density means less gas molecules along the path length S which can absorb and emit radiation, hence total gas emissivity decreases for higher temperatures.

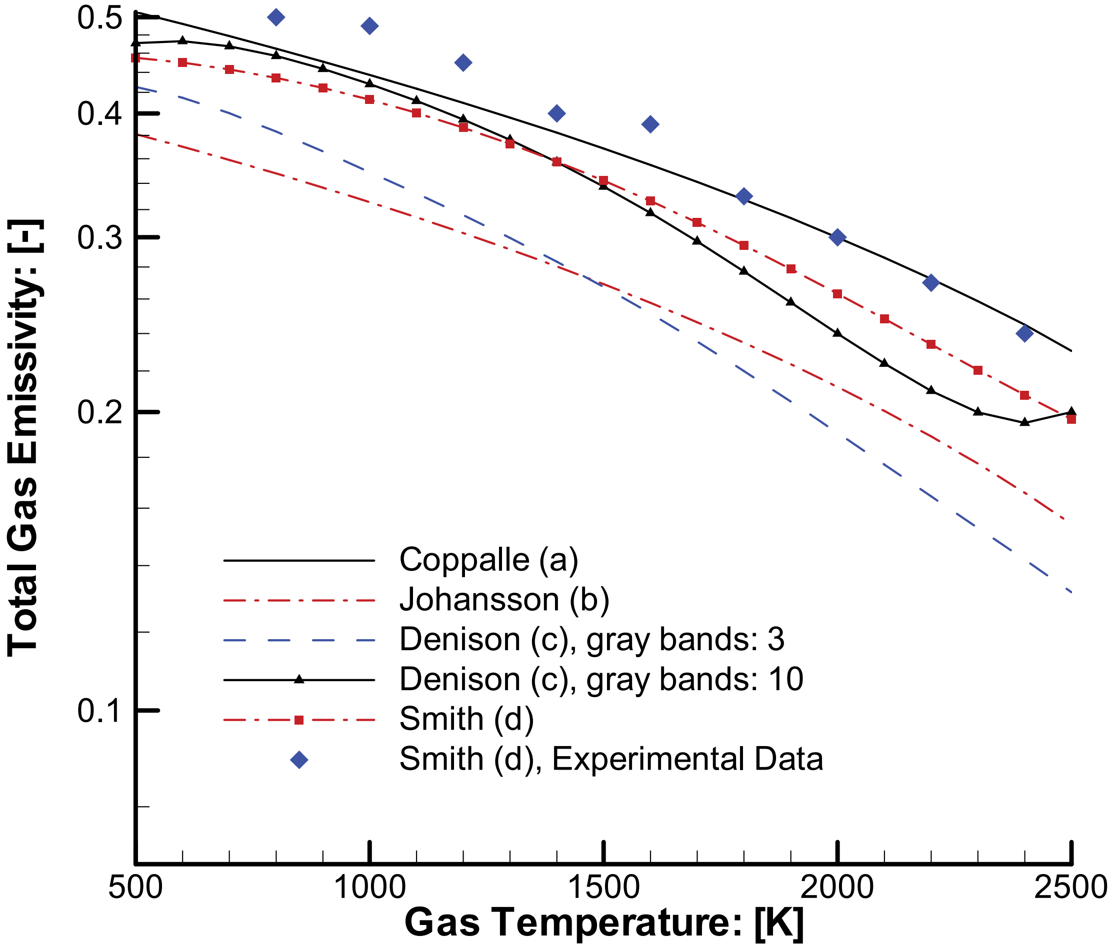

Figure 17: Comparison of WSGG models for a mixture of H_2O and CO_2 at a partial pressure path length of 1.0 atm m ; (a) = [90], (b) = [91], (c) = [75] and (d) = [79]

5.2.2 Total Gas Emissivity at Elevated Pressure for the SSME

This subchapter compares the total gas emissivity within the SSME main combustion chamber in dependence of different WSGG models. The values of the total gas emissivity are not used directly in the numerical method, since only the weights w_i and absorption coefficients a_i are required to evaluate the radiative heat fluxes. But total gas emissivity allows a suitable visualisation of the differences between the selected WSGG models.

Due to the limited temperature regimes of the WSGG models as depicted in Tab. 2, a jump function for the gas temperature entering the WSGG approach is introduced. If the gas temperature of a finite volume cell is higher than the limit-temperature of the WSGG model, the limit-temperature is used for the WSGG calculation. Using the unlimited gas temperature leads to significant unphysical results for the weights w_i and absorption coefficients a_i. Considering the gas pressure on the other hand, it was observed that exceeding the pressure limit indicates meaningful physical results according to the EBCOW analytic tool. For the H_2-O_2 combustion system Tab. 3 shows the characteristic thermodynamic state within the SSME main combustion chamber.

Table 3: Reference state of the SSME main combustion chamber for the H_2-O_2 combustion

Maximal Static Gas Temperature [K]	3858
Maximal Static Gas Pressure [MPa]	20.874
Path Length (Diameter of the SSME at inlet) [m]	0.464
Molar Fraction of H_2O [-]	0.7360

The results for total gas emissivity are shown in Fig. 18 and reveal the significant difference between the gas emissivities calculated by Smith's and Denison's model at atmospheric pressure and Denison's model at elevated pressure. If the temperature-limit of the corresponding WSGG model is exceeded, it corresponds to a zero order extrapolation of the total gas emissivity in terms of the visualization in Fig. 18.

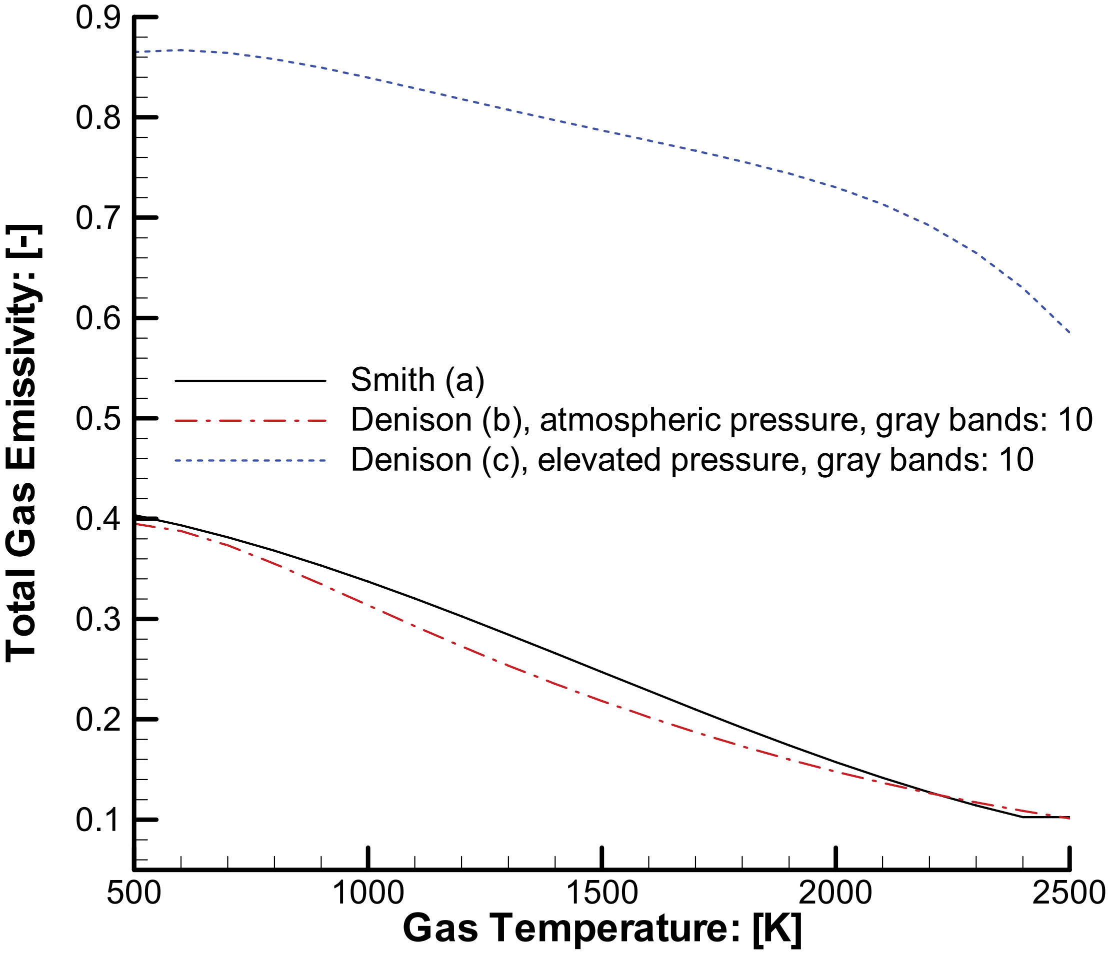

Figure 18: Total emissivity versus temperature for H_2-O_2 combustion in the SSME main combustion chamber; (a) = [79], (b) = [72] and (c) = [76]

When comparing Denison’s gas emissivity at elevated pressure using 10 gray bands to Smith’s results, the relative difference is about 125 % compared to Smith’s value. Due to the fact that the temperature regimes are identical for Denison’s atmospheric and elevated pressure case, Fig. 18 reveals that the partial pressure of the radiating species has a big influence on the total gas emissivity.

The SLWSGG model from Denison for elevated pressures is assumed to give the best approximation of the total gas emissivity with regard to the SSME main combustion chamber because it is (analytically) validated at elevated pressures up to 100 atm.

In addition to the conventional H_2-O_2 combustion system of the SSME, a novel CH_4-O_2 system is regarded using the original geometry of the SSME main combustion chamber for the CFD simulations as will be elucidated in subchapter 6.5. The CH_4-O_2 system is investigated in order to demonstrate the influence of methane on gas radiation and radiative heat loads compared to hydrogen. Table 4 summarizes the characteristic thermodynamic state of the novel methane combustion chamber.

Table 4: Reference state of the novel methane combustion chamber for the CH_4-O_2 combustion

Maximal Static Gas Temperature [K]	3711
Maximal Static Gas Pressure [MPa]	20.510
Path Length (Diameter of the SSME at inlet) [m]	0.464
Molar Fraction of CO_2 [-]	0.3279
Molar Fraction of H_2O [-]	0.6558

Figure 19 shows the total gas emissivity for the CH_4-O_2 combustion system of the novel methane combustion chamber. It is obvious that the total gas emissivity increases compared to the H_2-O_2 combustion system. This is reasonable because carbon dioxide is known as a strong radiator and hence enhances total gas emissivity. Furthermore, the differences between the atmospheric models and the model of Denison for elevated pressures are significant. A comparison of Smith, Coppalle and Johansson with Denison at elevated pressures shows that the relative differences are about 200 % on average.

For the CH_4-O_2 combustion system the application of Denison’s model at elevated pressure provides the best approximation for the conditions of the novel methane combustion chamber and induces the highest total gas emissivity.

It can be summarised that for both combustion systems, H_2-O_2 and CH_4-O_2, Denison’s SLWSGG models at an elevated pressure up to 100 atm represents the best choice for the thermodynamic conditions in the original SSME main combustion chamber, respectively the novel CH_4-O_2 combustion chamber. The largest error occurs if the temperature limit is exceeded; therefore the temperature input in the WSGG model is predictively limited. An empirical study with the EBCOW comparison tool revealed that exceeding the pressure limit of the WSGG model provides meaningful physical results, in contrast to the overstepping of the temperature limit. However, regarding the CFD simulations, it was observed for Denison’s models that a convergence is quite impossible if the pressure input in the WSGG model is not limited.

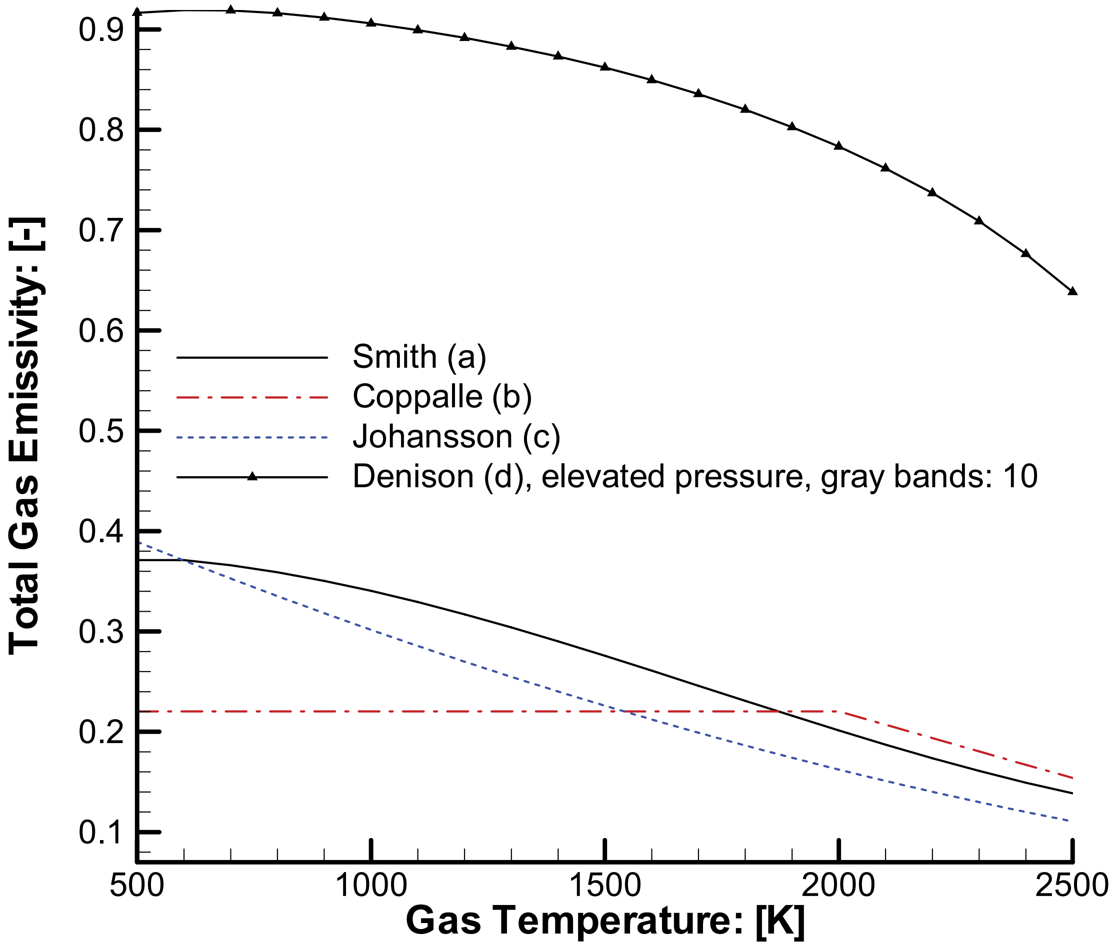

Figure 19: Total emissivity versus temperature for the CH_4-O_2 system in the novel methane combustion chamber; (a) = [79], (b) = [90], (c) = [91] and (d) = [75]

A comparison of a limited and unlimited Denison CFD calculation with respect to the radiative wall heat flux reveals that the differences are small. Hence, for the CFD simulations using Denison's models the pressure is limited to 100 atm. Considering the WSGG models of Smith and Coppalle, the pressure entered in the WSGG approach is not limited.

6 CFD Simulation of the SSME Main Combustion Chamber

6.1 Introduction

In the previous chapters the theory on radiation heat transfer and the implementation of the Rosseland Radiation Model (RRM) in NSMB was described. In this chapter the implemented RRM is applied to a practical engineering problem: the SSME main combustion chamber. The entire SSME is shown in Fig. 20. This configuration is selected on the one hand because of the high operating pressure, gas temperature and molar fraction of H_2O and on the other hand because a suitable number of published data is available.

Figure 20: The Space Shuttle Main Engine (SSME), from [94]

The Rosseland Radiation Model is a simple form of approximating the radiative transfer equation. One aim of this chapter is to investigate the performance of the Rosseland approximation compared to the P_1-method and Discrete Transfer Method (DTM), which represent more accurate transport models. For the P_1 and DTM calculations two commercial CFD solvers are used: ANSYS CFX and FLUENT. In addition to solutions by Naraghi et al. [20] and NASA results from Wang [21] the CFD results of CFX, FLUENT and NSMB are compared with each other.

An important design criteria of the SSME main combustion chamber is the quantitative distribution of the total wall heat flux (TWHF) of the combustion chamber, hence this quantity is investigated in detail. The TWHF is mainly influenced by convective and radiative heat transport in the case of a rocket combustion chamber. One focus of this thesis is to investigate the quantitative impact of gas radiation on the TWHF. For this investigation two typical rocket combustion systems are considered: liquid hydrogen-oxygen (LH_2-LO_2) and liquid methane-oxygen (LCH_4-LO_2). The first LH_2 system corresponds to the original SSME main combustion chamber, whereas the second LCH_4 system is a novel methane combustion chamber assuming identical thrust compared to the LH_2-LO_2 case and using the original geometry of the SSME main combustion chamber in order to compare the CFD results.

6.2 Definition of the Simulation Environment and Boundary Conditions

All CFD simulations are performed in steady state with local time stepping and for NSMB the full multigrid approach is used for convergence acceleration. For the CFX and FLUENT simulations Menter's [95] Shear Stress Transport (SST) version of the $k-\omega$ two equation turbulence model is used. With regard to NSMB only the one equation turbulence model by Spalart-Allmaras [96] is used due to convergence problems with the two equation turbulence models. The Spalart-Allmaras model is a low-Reynolds-number model requiring a very fine near-wall resolution in order to resolve the viscous sublayer of the boundary layer. For the current problem it is a good compromise between stability of the simulation, CPU time costs and accuracy.

For all three CFD codes the implicit time stepping scheme is applied and a second order spatial discretisation scheme is used. For the CFX and FLUENT calculations the chemistry is modelled with the Magnussen equilibrium model [97], also known as Eddy Dissipation Model (EDM). An equilibrium-chemistry and a frozen mixture of gases calculation are investigated and compared in [92], showing neglectable differences. Hence, all NSMB simulations are performed as a frozen mixture of thermal ideal gases. This ensures acceptable computation times of the NSMB simulations compared to CFX and FLUENT.

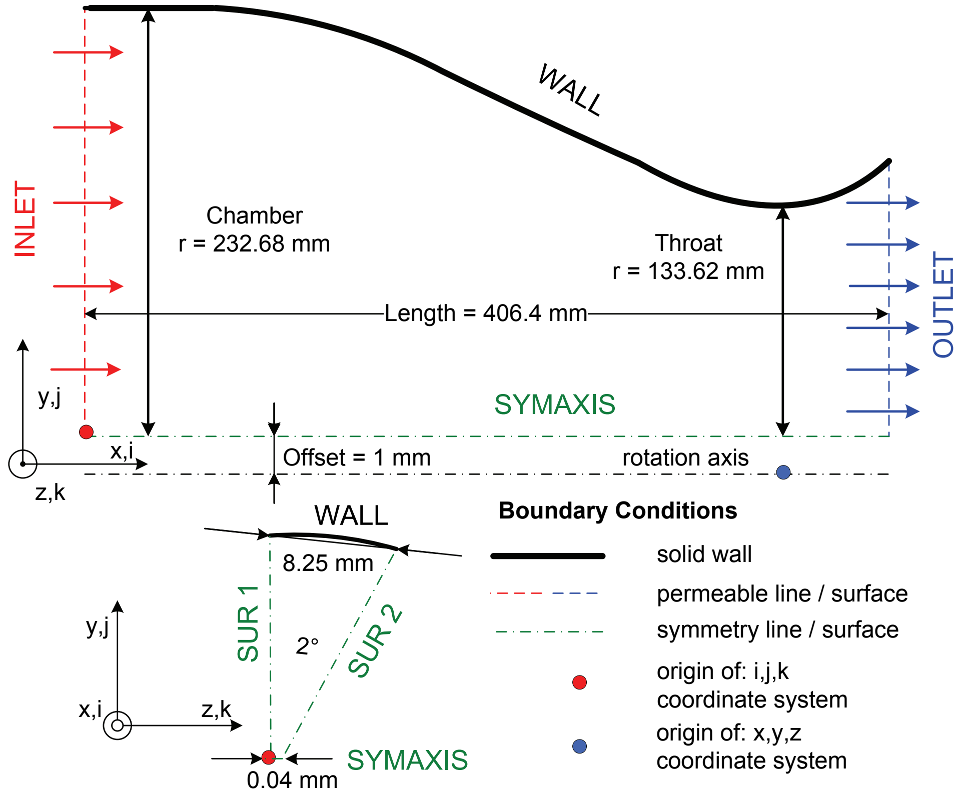

Figure 21: Geometry of the SSME main combustion chamber for all CFD simulations

For the modelling of the radiative transport the P_1-method [5] and the Discrete Transfer Method (DTM) [4] are used for CFX and FLUENT and the Rosseland model is used for the NSMB simulations. Considering the spectral modelling of the radiative transfer, the weighted-sum-of-gray-gases (WSGG) approach [3] is applied. For this purpose, the analytic WSGG models of Smith et al. [79], Denison & Webb [72; 75; 76] and Coppalle [90] are implemented in CFX and NSMB. In FLUENT, Coppalle's model is implemented by default including the scaling rules of Edwards [98]. The limitations of the WSGG models are given in Tab. 2.

For all CFD simulations the same geometry of [99] is used, as depicted in Fig. 21 and Appendix B. Several mesh derivatives are generated to investigate the mesh independency of the CFD solution, particularly the influence on the wall quantities, e.g. total and radiative wall heat flux.

The CFD inlet boundary condition of the combustion chamber is calculated with the CEA equilibrium chemistry code, also known as "Gordon and McBride" [100]. The CEA software is used to calculate the equilibrium composition of the LH_2-LO_2, respectively LCH_4-LO_2 systems. The operating conditions of both combustion systems are summarised in Tabs. 5 and 6.

Table 5: Operating conditions of the SSME main combustion chamber for the LH_2-LO_2 system, CEA hp-problem

Description	Value	Comment
Static Pressure [MPa]	20.874	Input CEA from Naraghi [20]
Oxidizer/Fuel-Ratio [-]	6 (stoichiometric: 8)	Rocketdyne [94]
Mass Flow Rate LO_2 [kg/s]	419.88	Williams [101]
Mass Flow Rate LH_2 [kg/s]	69.83	Williams [101]
Mass Fraction LO_2 (Injector) [-]	0.85714	Input CEA from Göbel [102]
Mass Fraction LH_2 (Injector) [-]	0.14286	Input CEA from Göbel [102]
Temperature LO_2 (Injector) [K]	90	Input CEA
Temperature LH_2 (Injector) [K]	20	Input CEA
Considered Species [-]	H_2, O_2, H_2O	Input CEA

For the CFD inlet boundary condition a perfectly mixed and combusted fluid is considered and all reactants are assumed gaseous. In association with the CFD simulations the notation for both systems is H_2-O_2, respectively CH_4-O_2.

Table 6: Operating conditions of the novel methane combustion chamber for the LCH_4-LO_2 system, CEA tp-problem

Description	Value	Comment
Static Temperature [K]	3711	Input CEA from Otto [103]
Static Pressure [MPa]	20.510	Input CEA from Otto [103]
Oxidizer/Fuel-Ratio [-]	3.8 (stoichiometric: 4)	Input CEA from Otto [103]
Temperature LO_2 (Injector) [K]	90	Input CEA
Temperature LCH_4 (Injector) [K]	112	Input CEA
Considered Species [-]	CH_4, O_2, CO_2, H_2O	Input CEA

In order to render the CFD results of both H_2-O_2 and CH_4-O_2 studies reproducible, the boundary conditions are presented in the following. The values for the inlet boundary condition for the H_2-O_2 study are listed in Tab. 7, the values for the CH_4-O_2 study are included in Tab. 8.

Table 7: Inlet boundary condition for the H_2-O_2 CFD study

Input Variable	**Value**	**Comment**
Total pressure [MPa]	21.3249	From Birgel [92]
Total Temperature [K]	3870	From Birgel [92]
Density [kg/m³]	9.119	Result from CEA
Isentropic Coefficient [-]	1.169	Result from CEA
Speed of Sound [m/s]	1636	Result from CEA
Turb. Kinetic Energy [m^2/s^2]	368	Approx. from [104]
Turb. Eddy Dissipation [m^2/s^3]	10064736	Approx. from [104]
Mass Fraction H_2 [-]	0.0369	Result from CEA
Mass Fraction O_2 [-]	0.0161	Result from CEA
Mass Fraction H_2O [-]	0.9470	Result from CEA

Table 8: Inlet boundary condition for the CH_4-O_2 CFD study

Input Variable	**Value**	**Comment**
Total pressure [MPa]	20.999	From Birgel [92]
Total Temperature [K]	3723	From Birgel [92]
Density [kg/m³]	17.619	Result from CEA
Isentropic Coefficient [-]	1.157	Result from CEA
Speed of Sound [m/s]	1161	Result from CEA
Turb. Kinetic Energy [m^2/s^2]	206	Approx. from [104]
Turb. Eddy Dissipation [m^2/s^3]	4228272	Approx. from [104]
Mass Fraction CH_4 [-]	0.00989	Result from CEA
Mass Fraction O_2 [-]	0.00001	Result from CEA
Mass Fraction CO_2 [-]	0.54440	Result from CEA
Mass Fraction H_2O [-]	0.44570	Result from CEA

The flow is supersonic behind the throat and therefore no physical boundary condition is required for the outlet [60]. This is a result of the fact that all characteristic lines of transport of information are pointing downstream, i.e. a downstream point in the flow cannot physically influence an upstream point. The no-slip wall boundary condition for both studies, H_2-O_2 and CH_4-O_2, is specified with a variable temperature distribution given in Fig. 22, and includes the influence of the cooling channels inside the chamber wall. The emissivity of the wall surface is derived from the wall material copper and is assumed to be $\varepsilon_w \approx 0.7$ [105].

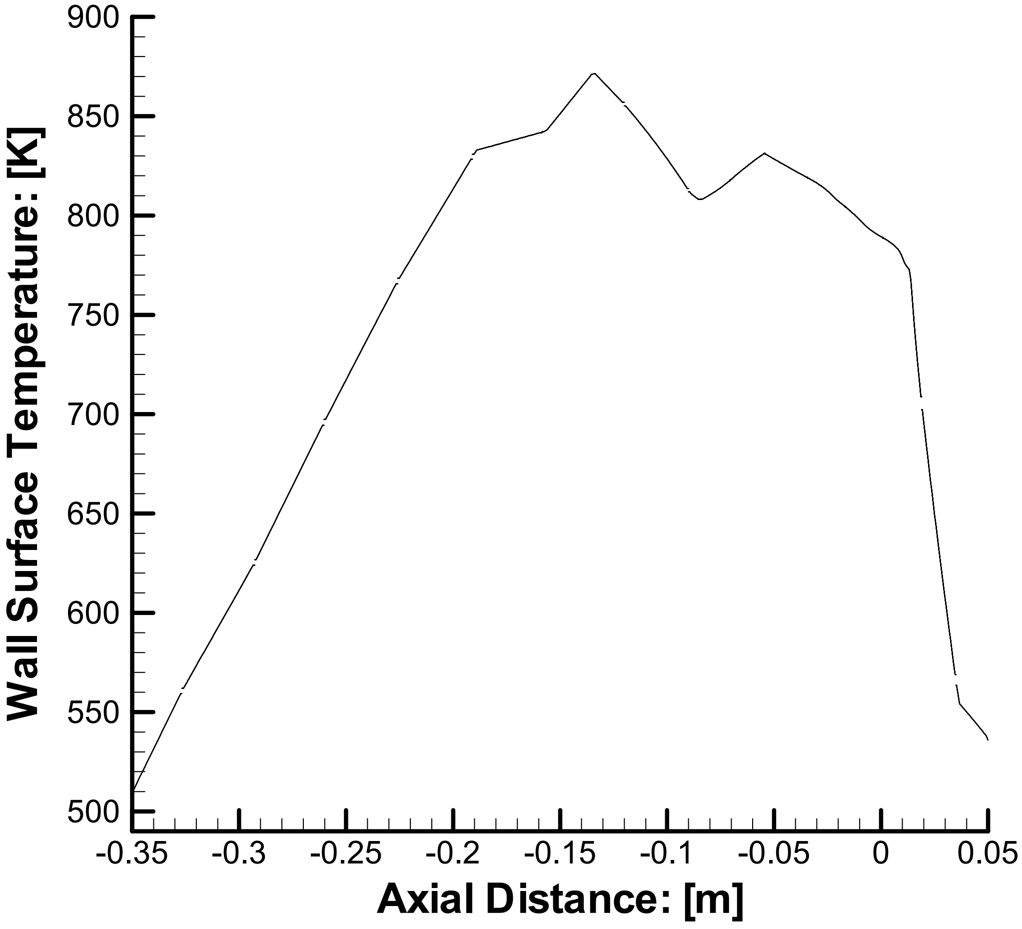

Figure 22: Cooled wall temperature distribution of the SSME main combustion chamber, based on Naraghi et al. [20]

6.3 Solution Strategy and Comments Concerning the CFD Simulations

For the solution of a new CFD problem an efficient strategy is required in order to minimise the total computational time. For this purpose, three model groups with different orders of complexity are introduced in this thesis; see Tab. 9. The first group only takes into account a mixture of thermal ideal gases in conjunction with a turbulence model. In the second group the chemistry is modelled in addition, and in the third group radiative heat transfer is included. CFX and FLUENT calculations are performed for all three groups, whereas NSMB only treats the first and third group because the results of the first and second group show that they differ only slightly from each other. Within each model group the calculation starts with a suitable initialization and after a converged solution is obtained it is used to initialise the next higher model group. A fine mesh near the solid wall is necessary to properly resolve the near-wall values. The distance of the first mesh node to the solid wall is in the order of 10^{-8} m. The CFX and FLUENT computations revealed significant convergence and stability problems with this fine wall resolution. To overcome this problem, multiple derivates of coarser meshes are created and each converged solution is extrapolated to the next finer mesh. A full multigrid approach is available with NSMB which automatically generates grid levels with different coarsenesses and subsequently delivers solutions for each grid level, with the solution automatically being extrapolated to the next finer grid level until the finest mesh is reached.

Table 9: Summary of model hierarchy groups for the CFD simulations

	1st Model Group	2nd Model Group	3rd Model Group
Gas model	Mixture of thermal ideal gases (MTIG)	Mixture of thermal ideal gases (MTIG)	Mixture of thermal ideal gases (MTIG)
Turbulence	NSMB: 1-Eq - Spalart-Allmaras CFX, FLUENT: 2-Eq - $k-\varepsilon$, SST	CFX, FLUENT: 2-Eq - $k-\varepsilon$, SST	NSMB: 1-Eq - Spalart-Allmaras CFX, FLUENT: 2-Eq - $k-\varepsilon$, SST
Chemistry	none	Eddy Dissipation	CFX, FLUENT: Eddy Dissipation NSMB: none
Radiation Transport	none	none	CFX, FLUENT: P_1, DTM NSMB: RRM
Radiation Spectral	none	none	WSGGM

The wall resolution is characterized by the dimensionless wall distance y^+, which is defined as

$$y^+ = \frac{u_* y \rho}{\mu}, \tag{117}$$

where y is the geometrical distance of the first mesh node to the wall and allows the grid designer to define a suitable node distribution normal to the wall. μ is the local dynamic viscosity and ρ the density of the fluid, while u_* represents friction velocity. This velocity is given as

$$u_* = \sqrt{\frac{\tau_w}{\rho}} \tag{118}$$

where τ_w is the wall shear stress. For an accurate wall resolution of the wall quantities, e.g. total wall heat flux, a y^+ of unity or smaller is required. The parameter y^+ has significant influence on the turbulence modelling in the boundary layer. For example, the $k-\omega$ based shear stress transport (SST) model for low-Reynolds numbers requires a $y^+ < 2$, whereas the low-Reynolds number $k-\varepsilon$ even requires $y^+ < 1$ [95]. The $k-\varepsilon$ models are primarily valid for turbulent core flows, i.e. the flow in the regions far away from a solid wall. The Spalart-Allmaras and $k-\omega$ models are designed to be applied throughout the boundary layer. In CFX and FLUENT semi-empirical scalable wall functions for turbulence modelling are implemented. The wall function approach requires flow conditions which fulfil the constraint $30 < y^+ < 300$. The wall functions are used to bridge the viscosity-affected region between the wall and the fully-turbulent region of the core flow [106]. It is important to note that wall functions neglect the laminar sublayer fraction of the boundary layer. For flows at low Reynolds numbers this fact can cause an error in the displacement thickness of up to 25 % [107].

To investigate the influence of the dimensionless distance y^+ and the use of scalable wall functions on the wall values, an initial CFD study for the H_2-O_2 system is performed with CFX and FLUENT, denoted with $y^+_{\mathrm{ave}} \approx 280$. Using wall functions allows a coarser grid near the wall and therefore reduces the effort of the grid generation, increases the stability and additionally induces a faster convergence of the CFD computation. The "$y^+_{\mathrm{ave}} \approx 280$-study" shows that scalable wall functions are not able to properly resolve the total wall heat flux. Following from this conclusion a detailed grid study is performed, identifying a suitable wall resolution. The "best of" mesh from the grid study is used for the main part of the calculations, denoted with "$y^+_{\mathrm{ave}} \leq 1$".

6.4 Results of the H_2-O_2 CFD Study

The H_2-O_2 combustion system corresponds to the original SSME main combustion chamber [94]. This subchapter compares the CFD results of the CFD solvers CFX, FLUENT and NSMB with each other and with benchmark solutions by Naraghi et al. [20] and Wang [21]. The results of the wall values are investigated in detail as a function of different radiation transport models (DTM, P_1, RRM) and different spectral WSGG models (Smith, Coppalle, Denison). The total wall heat flux (TWHF) is of main interest, as its accurate prediction is critical with respect to the failure of a rocket combustion chamber. The radiative wall heat flux (RWHF) is discussed in detail to examine the fraction of radiation compared to the overall wall heat transfer. The influence of different turbulence models and chemistry modelling on the wall values and a grid sensitivity study are investigated extensively in [92].

6.4.1 Comparison of CFX and FLUENT for $y^+_{\mathrm{ave}} \approx 280$

Figure 23 shows the total wall heat flux (TWHF) calculated by CFX and FLUENT, including radiative heat transfer. The axial distance is defined as zero at the throat of the SSME main combustion chamber. One can observe that both CFD solvers calculate the distribution of TWHF well in terms of quality as compared to the benchmark case of Naraghi et al. [20].

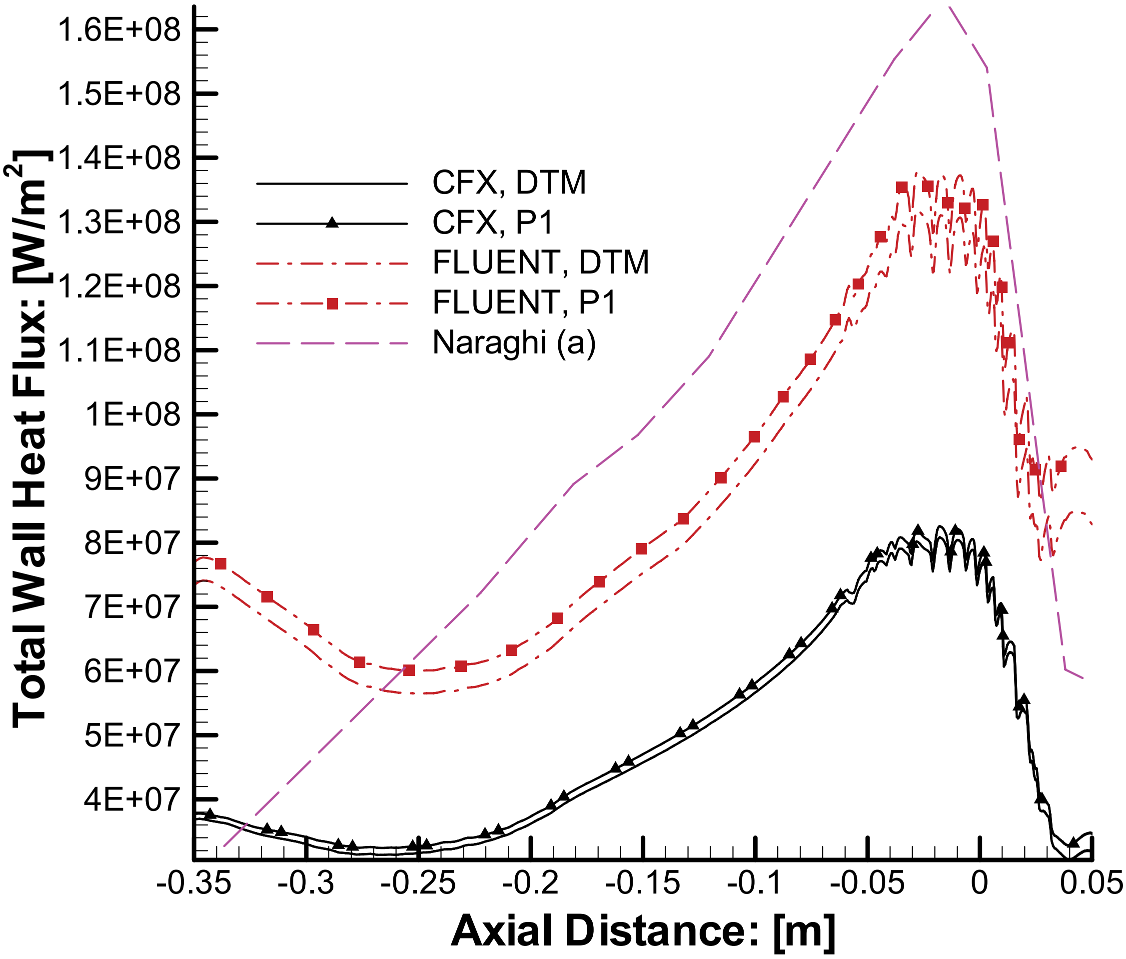

Figure 23: H_2-O_2 study - TWHF for the DTM and P_1 transport models and for Smith's WSGG model; (a) = [20]

Figure 23 reveals that the relative TWHF-difference between CFX and FLUENT is approximately 60 %. The relative TWHF-difference to the benchmark [20] depends on the CFD solver, and is for CFX about 50 % and for FLUENT about 20 %.

As will be shown later the quantitative differences between CFX and FLUENT become smaller for a dimensionless distance of $y^+_{\mathrm{ave}} \leq 1$. Hence the semi-empirical wall functions of the turbulence models seem to cause the big quantitative differences. Figure 24 depicts the radiative wall heat flux (RWHF) of the two radiation models P_1 and DTM and the spectral weighed-sum-of-gray-gases model (WSGGM) by Smith et al. [79]. One can observe that the results for the RWHF are too high using FLUENT in combination with the P_1 model when compared to Naraghi, whereas the DTM model produces a qualitatively better RWHF-distribution.

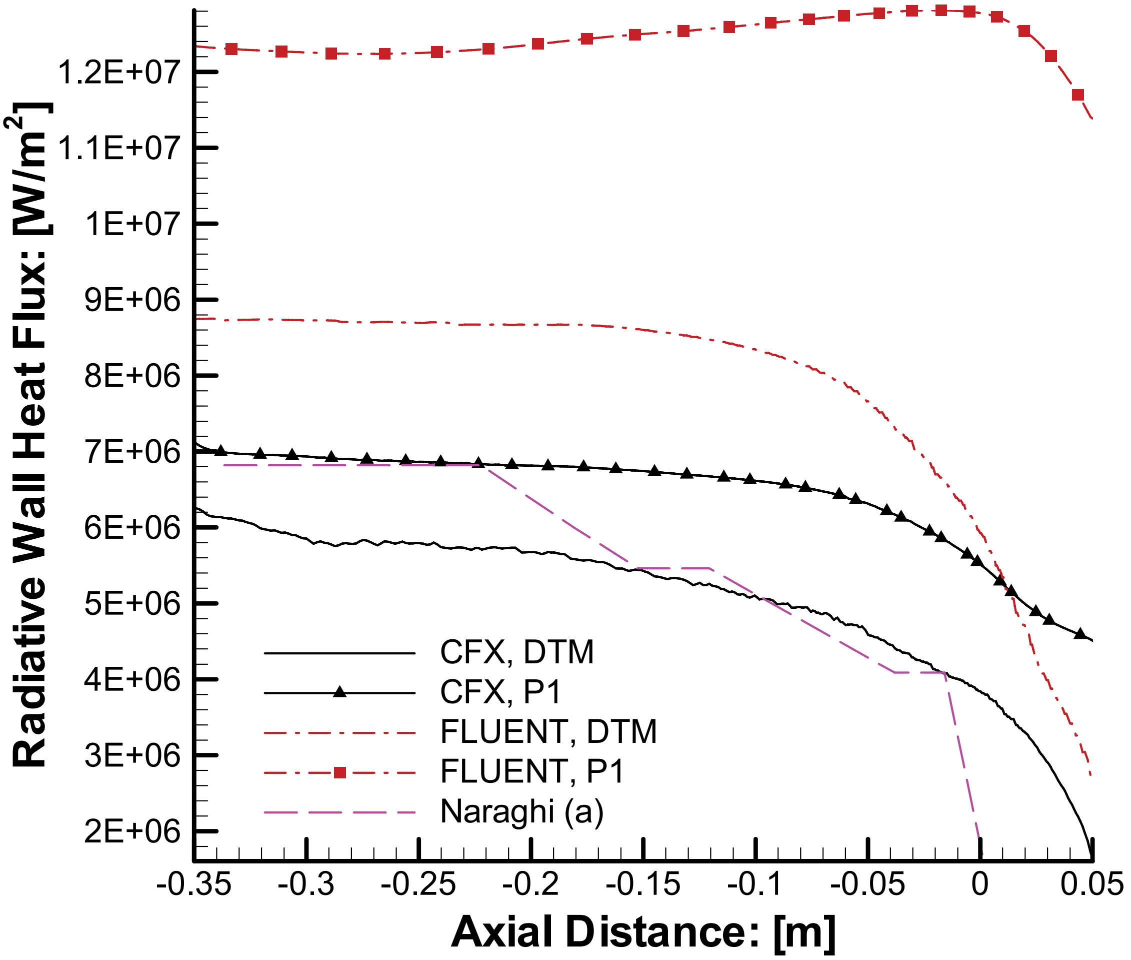

Figure 24: H_2-O_2 study - RWHF for the DTM and P_1 transport models and for Smith's WSGG model; (a) = [20]

One central aspect of this study is the amount of RWHF compared to the total wall heat flux (TWHF); this relation is illustrated in Fig. 25. Depending on the radiation model, the RWHF causes on average up to 9.3 % of the TWHF.

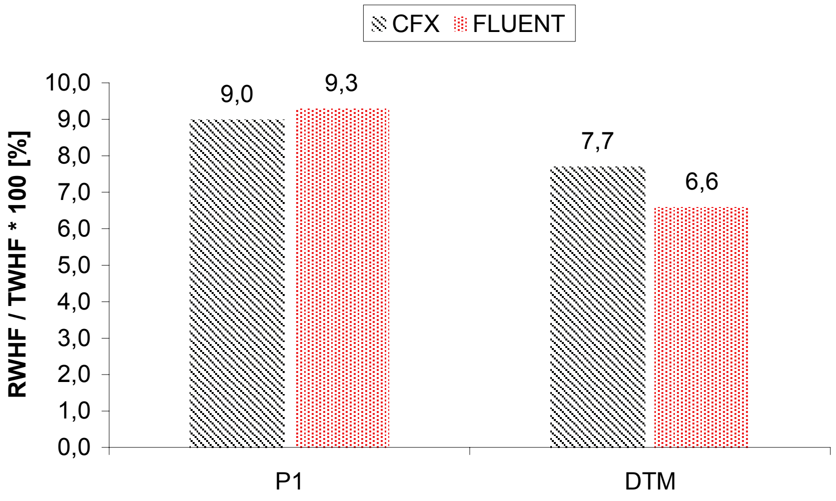

Figure 25: H_2-O_2 study - Average influence of the RWHF on the TWHF for the DTM and P_1 radiation models with Smith's WSGGM

With regard to the H_2-O_2 study this underlines that radiative energy transport from the gas mixture to the rocket chamber wall has a significant influence on the TWHF. In Fig. 26 the mesh sensitivity of the TWHF is further investigated and reveals that for $y^+_{\mathrm{ave}} \approx 2$ and smaller y^+_{ave} the CFD solution is independent of the near-wall mesh resolution of the boundary layer.

Furthermore, Fig. 26 shows that the axial TWHF distributions increase while the near-wall mesh is refined.

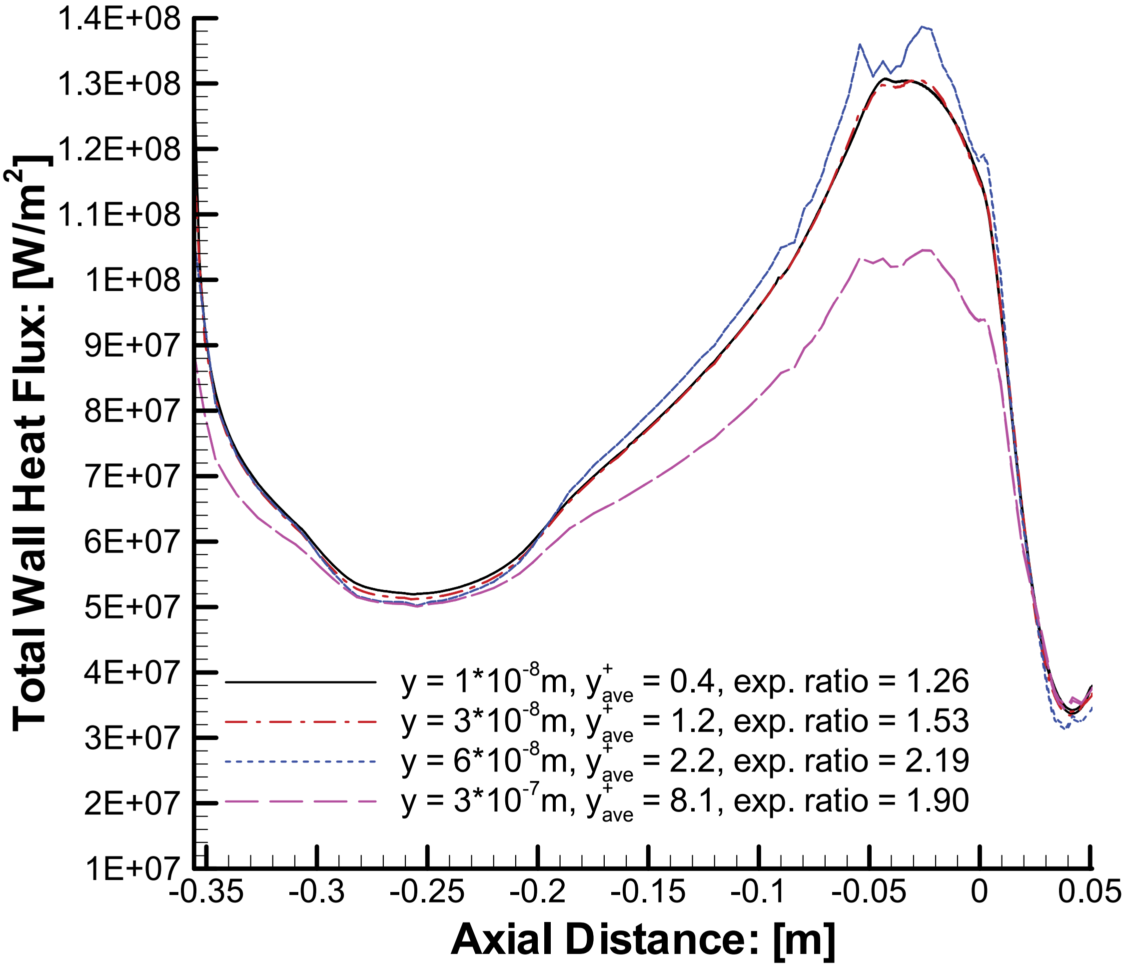

Figure 26: Mesh independency study of the CFD Solution for the TWHF

The occurring near-wall gradients, especially the temperature in the energy equation, are more accurate resolved, while the mesh density near the wall is increased. As a conclusion from this investigation an average dimensionless distance of $y^+_{\mathrm{ave}} \leq 1$ is found to give a suitable wall resolution and is therefore used in the following subchapters.

6.4.2 Comparison of CFX and NSMB for $y^+_{\mathrm{ave}} \leq 1$ and Smith's WSGGM

In this subchapter the CFX and NSMB CFD codes are compared to each other and to the benchmark computations by Naraghi et al. [20] and Wang [21] for an average dimensionless wall distance of $y^+_{\text{ave}} \leq 1$. Considering the radiative transport, three models are compared: the Discrete Transfer Method (DTM), the P$_1$-moment method and the Rosseland Radiation Model (RRM). For all calculations in this subchapter the spectral WSGG model by Smith et al. [79] is applied. Figure 27 reveals that the maximal total wall heat flux (TWHF) occurs close to the throat due to the decrease of the nozzle diameter d and the basic scaling:

$$q_{\text{TWHF}} \sim \left(\text{Re}_d\right)^{0.8}, \tag{119}$$

with

$$\text{Re}_d \sim \frac{\dot{m}}{d\ \mu}. \tag{120}$$

For a constant mass flow rate $\dot{m}$ Eq. (120) reveals that the Reynolds number increases towards the throat due to the decrease of the nozzle diameter d. As discussed later on, the dynamic viscosity μ also decreases towards the throat. Hence, the maximum value of the Reynolds number is near the throat and induces the highest TWHF. Equation (119) is derived from the Nusselt correlation for a one-dimensional, steady-state heat transfer problem in a liquid rocket chamber, given in Sutton & Biblarz [11]:

$$\text{Nu} = 0.026\left(\text{Re}_d\right)^{0.8}\left(\text{Pr}\right)^{0.4}, \tag{121}$$

with

$$\text{Nu}=\frac{h_{\text{g}}\ d}{k_{\text{cd}}}, \tag{122}$$

$$\text{Re}_d = \frac{d\ v\ \rho}{\mu}, \tag{123}$$

$$\text{Pr} = \frac{\mu\ c_p}{k_{\text{cd}}}. \tag{20}$$

The qualitative distribution of the total wall heat flux (TWHF) of the SSME main combustion chamber is discussed more detailed in the following. The present combustion chamber corresponds in principal to a convergent-divergent nozzle, whereas the smallest diameter represents the throat (axial distance = 0 m, see Fig. 27). For the CFD simulations the calculation domain ends shortly after the throat in downstream direction, for reasons described in chapter 6.2. Hence, the divergent part of the nozzle is not considered in the scope of this thesis.

The static temperature of the combusted gases has its maximum value in front of the convergent section, near the inlet; see Fig. 21. Due to the acceleration of the flow towards the throat the internal energy, Eq. (17), is converted into kinetic energy $e_{\text{kin}} = 1/2\ v^2$, according to Eq. (3). Therefore, the static temperature decreases towards the throat and induces a smaller dynamic viscosity via Sutherland's law, Eq. (19). This effect in turn implies a smaller thermal heat conductivity due to Prandtl's law, Eq. (20), assuming a constant Prandtl number.

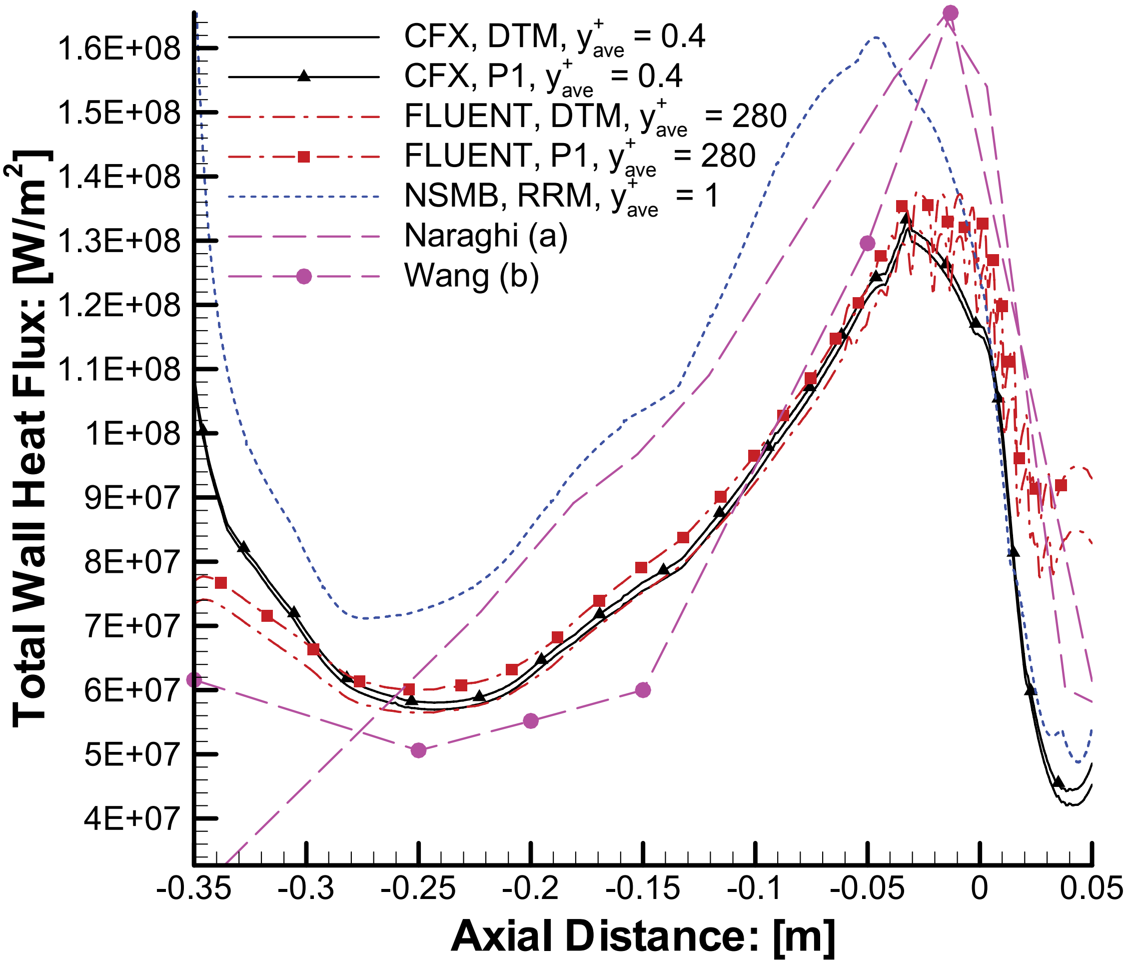

Figure 27: H_2-O_2 study - TWHF for the DTM, P_1 and RRM transport models and for Smith's WSGG model; (a) = [20] and (b) = [21]

The thermal heat conductivity is the transport coefficient of the heat flux due to conduction; see Fourier's law, Eq. (15). When the thermal heat conductivity is reduced, the thermal boundary layer becomes thinner. The thermal boundary layer acts as a thermal protection between the hot gas and the solid chamber wall. The thinner the thermal boundary layer, the higher the TWHF.

Furthermore, the decrease of the dynamic viscosity towards the throat (induced mainly by the decrease of the static temperature) additionally contributes to the increase of the Reynolds number via Eq. (120). Therefore, for the present problem the maximum value of the Reynolds number occurs near the throat, inducing the thinnest thermal boundary layer, respectively the highest TWHF at that location.

In addition to the discussed phenomena the Mangler [108] effect influences the thermal boundary layer thickness. For a laminar flow over a flat plate with a Prandtl number of unity, the Reynolds number is related to the thermal boundary layer thickness δ_{th}, according to Schlichting & Gersten [109] via

$$\delta_{\text{th}} \sim \frac{1}{\sqrt{\mathrm{Re}_d}} \cdot \sqrt{\frac{x}{l}}\,, \tag{124}$$

where l is a characteristic length, respectively the length of the flat plate and x the geometric coordinate starting at the edge of the plate. Equation (124) reveals that the boundary layer thickness grows in proportion to $\sqrt{x}$. To account for a contoured chamber wall Eq. (124) can be transformed applying Mangler's transformation [108]:

$$\overline{x} = \frac{1}{l^2} \int_0^x r_{\mathrm{w}}^2(x)\, dx\,, \tag{125}$$

where r_{w} is the radius of the combustion chamber wall and $\overline{x}$ the axial distance. Assuming a characteristic length of $l = 1$ m and a coned shape of the converging section of the chamber (i.e. $r_{\mathrm{w}}(x) = x$), Eq. (125) gives

$$\overline{x} = \frac{x^3}{3} \text{ or } x = (3\overline{x})^{1/3}. \tag{126}$$

Hence Eq. (124) can be rewritten to:

$$\delta_{\text{th}} \sim \frac{1}{\sqrt{\mathrm{Re}_d}} \cdot (3\overline{x})^{1/6}. \tag{127}$$

Equation (127) demonstrates that the contour of the combustion chamber induces a smaller thermal boundary layer thickness with growing axial distance compared to a flat plate case. This effect can be regarded to additionally enlarge the total wall heat flux (TWHF) with increasing axial distance. The observation that the maximum TWHF occurs not exactly at the throat (axial distance = 0 m), but shortly in front of it at an upstream location results from the characteristics of the $\mathrm{Ma} = 1$ line. The maximum of the TWHF occurs at that location where the $\mathrm{Ma} = 1$ line leaves the solid wall of the combustion chamber.

It can be observed in Fig. 27 that all three CFD codes calculate the position of the maximum TWHF more upstream compared to the benchmark computations by Naraghi and Wang. This discrepancy is related to the location of the $\mathrm{Ma} = 1$ line, depending mainly on the static thermodynamic quantities of the gas mixture. The chemical modelling significantly influences the thermodynamic variables of state. For example, in the case of the NSMB calculation, no chemical reactions are modelled, rather only a constant mixture of thermal ideal gases. Chemical equilibrium is assumed for CFX and FLUENT, whereas Wang [21] applies chemical non-equilibrium. In addition, all CFD codes include only the reactants H_2, O_2, H_2O, in contrast to the benchmark computations which include more reactants and reactions. A test calculation with the CEA [100] equilibrium chemistry code including the species H_2, O_2, H_2O and OH generates a static combustion temperature of 3678 K, compared to 3858 K applying only the species H_2, O_2, H_2O as used for the CFD simulations.

Furthermore, numerical reasons can have an impact on the position of the static thermodynamic conditions, because several empirical assumptions are included especially in the turbulence modelling. The TWHF is particularly affected by the axial distribution of the turbulent viscosity in the boundary layer adjacent to the solid wall.

CFX in conjunction with DTM underestimates the TWHF about 25 % on average (absolute $33 \cdot 10^6$ W/m²) compared to Wang [21]. The quantitative TWHF distribution resulting from NSMB fits better to the benchmark than CFX. The higher NSMB total wall heat flux (TWHF) results from the Spalart-Allmaras turbulence model, when compared to the SST turbulence model of CFX. For a demonstration of FLUENT's scalable wall function approach (case $y^+_{\mathrm{ave}} = 280$) the result in Fig. 27 shows good agreement compared to the CFX calculations with $y^+_{\mathrm{ave}} = 0.4$ without scalable wall functions. In comparison with Fig. 23 FLUENT's scalable wall function approach seems to work more accurately for this special case compared to CFX.

In addition to the TWHF the radiative wall heat flux (RWHF) is of main interest to get an impression of the significance of the radiative energy transfer from the hot gas mixture to the solid wall of the SSME main combustion chamber. As depicted in Fig. 28 it is apparent that the maximum RWHF occurs near the inlet. This results from the fact that the RWHF strongly depends on the static gas temperature of the gas mixture. Figure 28 indicates that the highest temperature of the combusted gases occurs near the inlet, while it decreases downstream as the flow is accelerated towards the throat. CFX in conjunction with the Discrete Transfer Method (DTM) demonstrates the best fit compared to the benchmark by Wang [21] who uses the Discrete Ordinate Method (DOM). Both models, DTM and DOM, are similar with regard to their mathematical approach which might be the main reason for the good match in contrast to the P_1 radiation model.

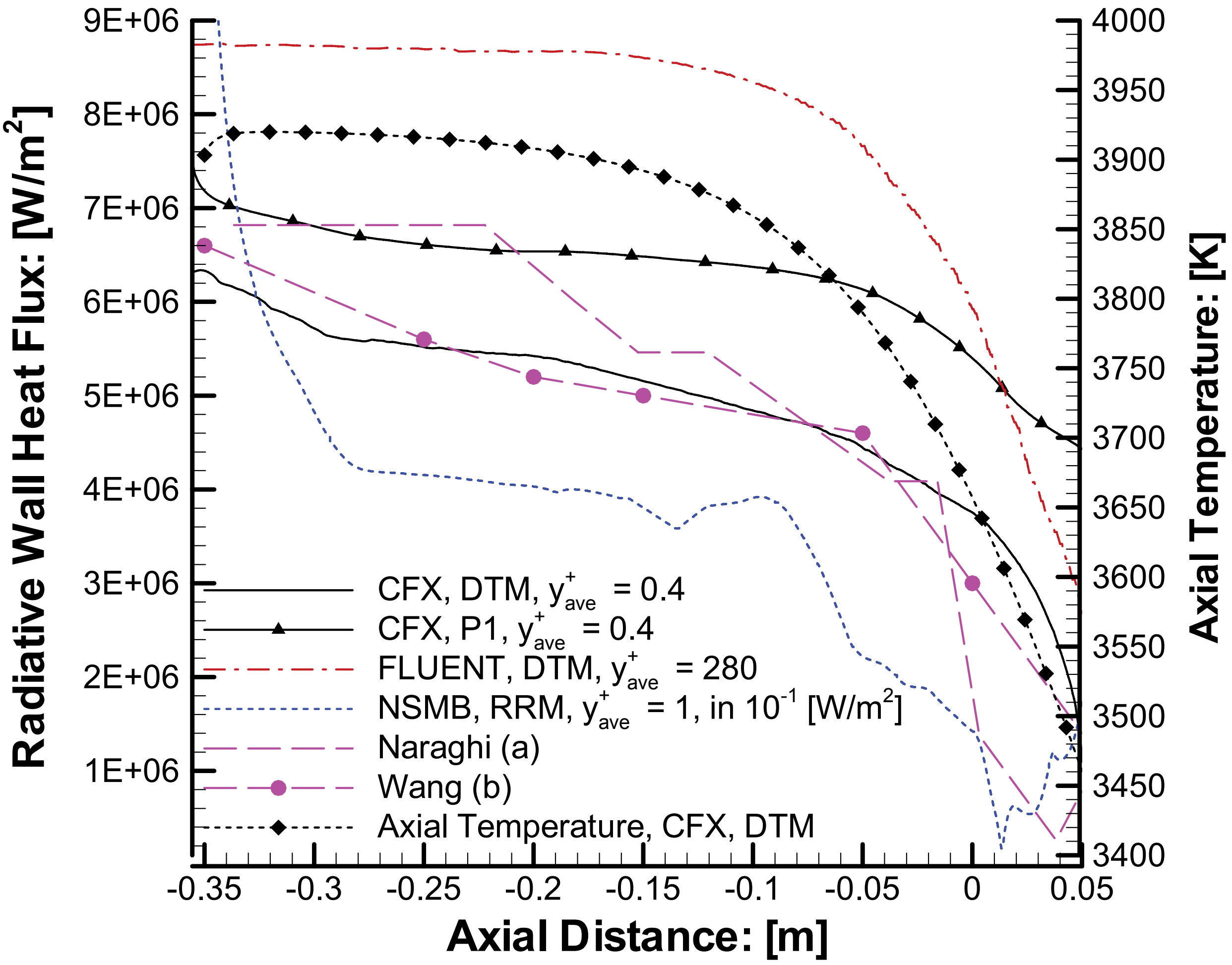

Figure 28: H_2-O_2 study - RWHF for the DTM, P_1 and RRM transport models and for Smith's WSGG model; (a) = [20] and (b) = [21]

The NSMB calculation provides qualitatively a good RWHF fit but overestimates quantitatively the radiative wall heat flux (RWHF) about a factor of approximately seven compared to Naraghi (absolute average values: $q_{\text{RWHF}}(\text{NSMB}) \approx 30.94 \cdot 10^6\ \text{W/m}^2$, $q_{\text{RWHF}}(\text{Naraghi}) \approx 4.46 \cdot 10^6\ \text{W/m}^2$). The quantitative difference between the NSMB-RRM case to the CFX-DTM calculation is additionally compared in Fig. 30. It is well known that the Rosseland approximation in general overestimates the RWHF, due to the diffusive characteristic and the invalidity near a solid wall [4; 5]. With CFX and FLUENT it was not possible to obtain a converged solution using the Roseland model in the case of the present grid with a wall resolution in the magnitude of order of 10^{-8} m. For a coarser wall resolution in the order of 10^{-5} m it was possible to obtain a converged Rosseland solution with CFX, but the RWHF was calculated unphysically high.

The standard Rosseland jump boundary condition in CFX and FLUENT is based on the jump correlation as a function of the conduction-radiation parameter N_{w}; see Eq. (109). Although the optical thickness of the SSME main combustion chamber is high enough to apply the diffusion approximation, the conduction-radiation parameter is small due to the small thermal heat conductivity k_{cd} (as typical for gases) compared to the radiative heat conductivity k_{R}. A small conduction-radiation parameter leads to a maximal temperature jump according to Eq. (110)

which is not realistic for the current problem. This fact induces either a crash for the CFX and FLUENT Rosseland calculations or leads to an unphysical high RWHF.

To eliminate this behaviour the jump boundary condition for the Rosseland model is modified in NSMB as result of an empirical investigation, allowing a more reasonable RWHF distribution. Nevertheless, the RWHF from NSMB is still too high reproduced, compared to P_1 and DTM. Up to date, a realistic jump boundary condition for the Rosseland diffusion model which is fully coupled to heat conduction and forced convection and for non-gray gases has not been worked out; see Howell [70]. Once a more realistic boundary condition for the Rosseland model is identified, it could be possible that it delivers a quantitatively more reasonable RWHF distribution. The NSMB-RRM calculations are only performed for the H_2-O_2 CFD study because of the high quantitative overprediction of the RWHF. For the CH_4-O_2 CFD study only the CFX and FLUENT CFD solvers are used in connection with the P_1, respectively the DTM.

6.4.3 Comparison of Different WSGG Models with CFX for $y^+_{\text{ave}} \leq 1$

Figure 29 reveals that the distributions of the radiative wall heat flux (RWHF) for Smith et al. [79] and Denison [72] are nearly identical if the gas pressure entering the WSGG model in Eq. (72) is limited fictitiously to a value of 1 atm. Both models are compared to demonstrate consistency between an experimental-fit-based model (Smith) and a HITRAN line-by-line based model (Denison).

The SSME main combustion chamber is operated at a much higher pressure of about 21 MPa. Hence, WSGG models are required which are valid for higher pressures. Denison's [76] SLWSGG model for a maximal gas pressure of 100 atm is selected and compared to Smith's WSGG model with unlimited pressure. It should be noted that Smith's model is only validated for a reference pressure of 1 atm. In this case, unlimited means that the pressure entered in Eq. (72) equals the static gas pressure. Both models show qualitatively good agreement with the benchmark solutions of Naraghi et al. [20] and Wang [21]. Denison's [76] model quantitatively overestimates the RWHF compared to the benchmark simulations because of the higher adiabatic gas temperature in the calculation domain, within the CFD study.

The higher adiabatic gas temperature results from neglecting the unbounded radicals H, O, OH within the scope of the CEA [100] chemistry calculation of the inlet boundary condition for the CFD simulations, see Tab. 5. Considering for example three species (H_2, O_2 and H_2O) instead of eight (H_2, O_2, H_2O, H, O, H_2O_2, OH and HO_2) in the CEA calculation, on average induces a higher gas temperature of 300 K. Including this effect would decrease the RWHF distribution of Denison [76].

Due to the highest pressure limit and line-by-line background, Denison's [76] SLWSGG model for elevated pressures up to 100 atm is defined as the "best of" spectral model for the H_2-O_2 CFD study.

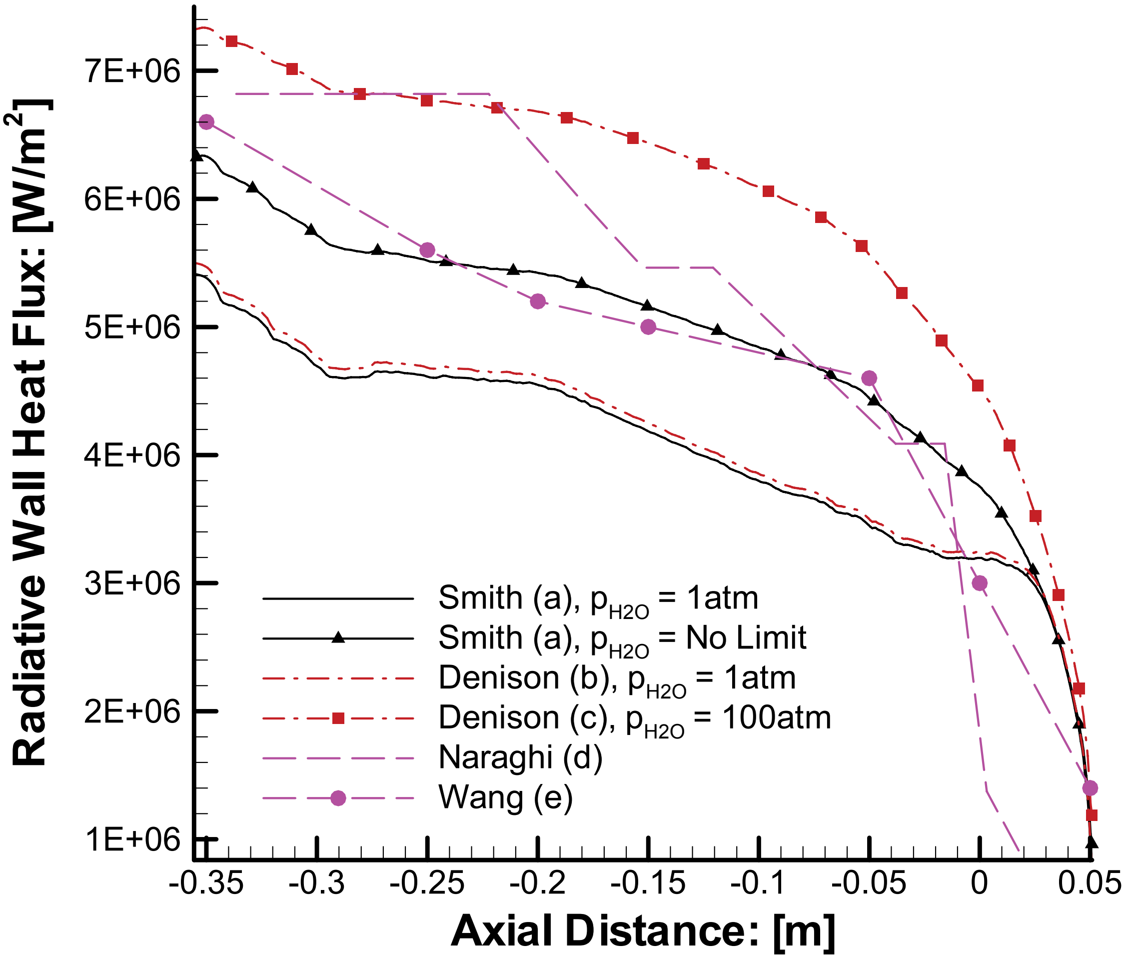

Figure 29: H_2-O_2 study - RWHF from CFX with the DTM transport model and for different WSGG models; (a) = [79], (b) = [72], (c) = [76], (d) = [20] and (e) = [21]

For the CFX “best of” case Fig. 30 illustrates for the DTM and Denison’s 100 atm case, that in average 7.7 % of the total wall heat flux is caused by radiation. Due to the strong temperature dependence of radiative heat transfer the highest value of this ratio is in the inlet region of the combustion chamber. The highest value of the static gas temperature is near the inlet, decreasing towards the throat (axial distance = 0 m). Figure 30 illustrates that the Rosseland Radiation Model (RRM) overestimates the amount of gas radiation, as already explained in the scope of Fig. 28.

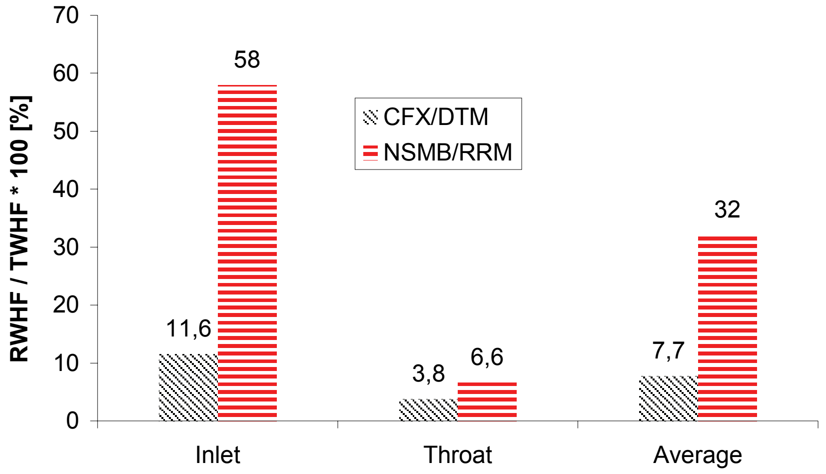

Figure 30: H_2-O_2 study - Influence of the radiative on the total wall heat flux for CFX with Denison's 100 atm [76] SLWSGG model and NSMB with Smith’s [79] WSGG model

The reason for the quantitative differences of the RWHF distributions in Fig. 29 can be found in the different optical properties of the gas mixture. The optical property of the gas mixture is characterized by the total absorption coefficient (TAC). The TAC multiplied by the characteristic optical path gives the total optical thickness. According to Eqs. (29) and (31) the total optical thickness can be calculated for the SSME main combustion chamber as:

$$\kappa \equiv a \cdot S \text{, with } a = \frac{1}{\tilde{S}} \text{ and } S = 0.464 \text{ m}, \tag{128}$$

where $\tilde{S}$ is the average penetration distance before a photon is absorbed and S is the diameter of the SSME main combustion chamber at the inlet. For an optical thickness larger than 10, the medium is commonly regarded as optical thick and the diffusion approximation of the radiative transfer equation can be applied [5]. The total absorption coefficient for different WSGG models is plotted in Fig. 31. One can observe that the TAC from Smith is almost twice as big, compared to Denison. This results from the fact that Denison’s model is limited to 100 atm, and Smith uses the unlimited pressure of approximately 210 atm. This observation reveals the strong pressure influence on the total absorption coefficient. The TAC values for a partial pressure of 1 atm are approximately 0.4 1/m. This explains the very low RWHF distribution for the 1 atm case in Fig. 29.

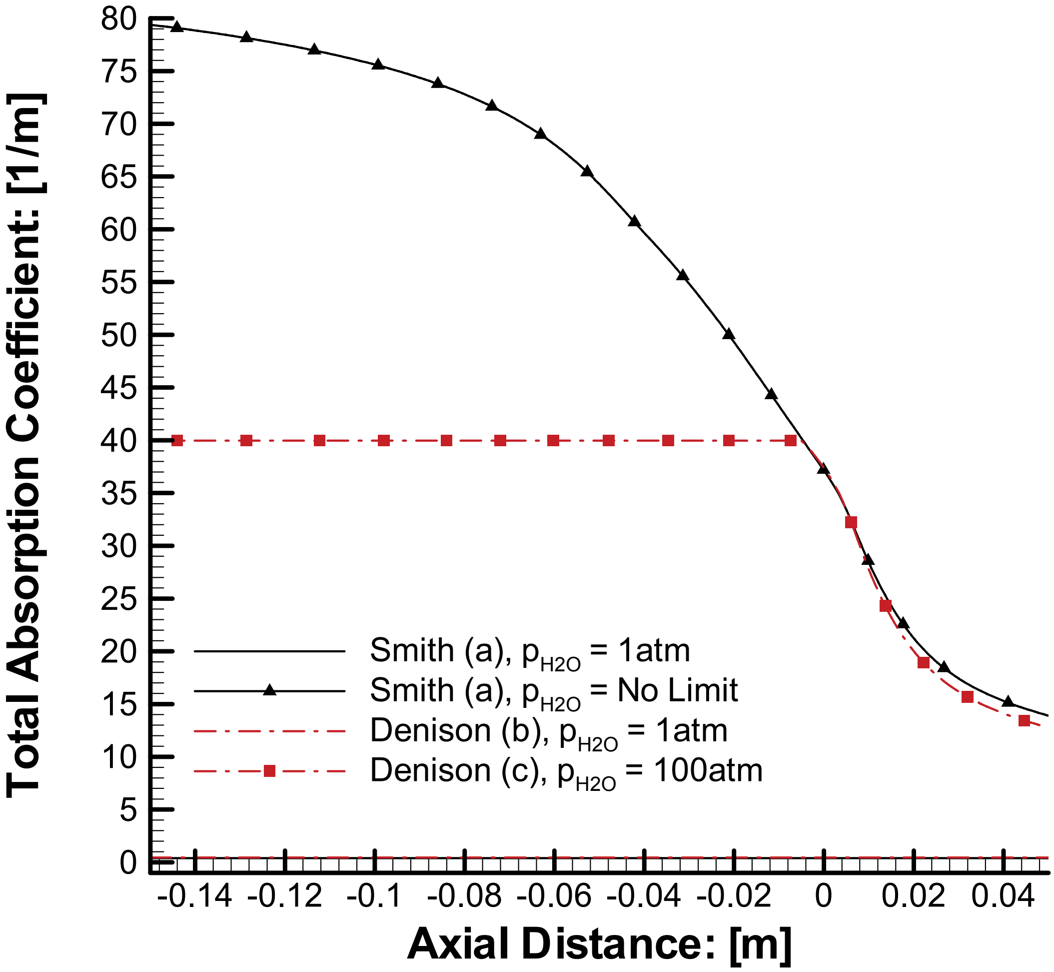

Figure 31: H_2-O_2 study - Total absorption coefficient from CFX with the DTM transport model and for y = 0.133 m = const; (a) = [79], (b) = [72] and (c) = [76]

Considering the cylindrical section of the SSME main combustion chamber (area between inlet and converging section) Tab. 10 summarizes the average values for the characteristic optical properties of the gas mixture. For the Denison, 100 atm case the photons on average travel a mean free path of $\widetilde{S} = 0.027\,\text{m}$ until they undergo absorption.

Table 10: H_2-O_2 study - Characteristic optical properties of the gas mixture from CFX with the DTM transport model, for the cylindrical section of the combustion chamber

	Smith [79] (No Limit)	Denison [76] (Limit = 100 atm)
Average total absorption coefficient a [1/m]	78	37
Average total optical thickness κ [-]	36	17
Average penetration distance $\widetilde{S}$ [m]	0.013	0.027

6.5 Results of the CH_4-O_2 CFD Study

In the previous subchapter the original hydrogen-oxygen SSME main combustion chamber is investigated in detail, whereas in this subchapter the impact of the hydrocarbon fuel methane compared to hydrogen is studied. Methane is investigated because both CO_2 and H_2O are produced during the LCH_4-LO_2 combustion, and both species are known as “strong radiators”. The advantages of the “green” propellant methane are described in subchapter 1.1.

The CEA equilibrium chemistry software [100] is applied to calculate the thermodynamic state of the LCH_4-LO_2 combustion, delivering the gas mixture at the inlet boundary condition of the CFD problem. For the CH_4-O_2 CFD study the original geometry of the SSME main combustion chamber is used in order to compare the results with those of the H_2-O_2 CFD study. A CEA parameter study reveals the CH_4-O_2 gas composition which is required to generate the same thrust at the throat for the novel LCH_4-LO_2 combustion chamber compared to the original LH_2-LO_2 SSME combustion system. As reference quantity the thrust of the rocket engine is selected because it allows the most practical comparison between the original H_2-O_2 and novel CH_4-O_2 combustion chamber considering the radiative impact of the fuel on the total wall heat flux. Other reference quantities, for example an identical reaction enthalpy for both combustion systems, were rejected because of the different mass specific energies of the H_2 and CH_4 fuels. For hydrogen the mass specific energy is 143 MJ/kg, whereas methane has an energy content of 50 MJ/kg [29]. Furthermore, the mass-specific heat at constant pressure c_p for hydrogen is seven times higher compared to methane ($c_{\mathrm{p,\,H_2}} = 14.4\ \mathrm{kJ/(kg\ K)}$, $c_{\mathrm{p,\,CH_4}} = 2.21\ \mathrm{kJ/(kg\ K)}$ at 300 K). In order to obtain the same reaction enthalpy in both systems, a higher adiabatic gas temperature is required for the methane system due to the relation $\Delta_\mathrm{R} H \sim c_\mathrm{p}\ dT$, where $\Delta_\mathrm{R} H$ is the reaction enthalpy. Due to the strong temperature dependence of the radiative energy exchange, a higher average gas temperature in the combustion chamber would distort the influence of the fuel on the optical properties of the radiative heat transfer in the gas mixture. As the reference quantity thrust delivers a lower average gas temperature for the CH_4-O_2 case; the impact of the radiative energy on the total wall heat flux can be regarded as the “lower boundary”. For higher operating pressures and temperatures in future methane combustion systems, this means that the impact of radiation is expected to be even higher compared to conventional hydrogen engines.

6.5.1 Comparison of CFX and FLUENT for $y^+_\mathrm{ave} \leq 1$ and Coppalle’s WSGGM

In this subchapter the CFD results of CFX and FLUENT are compared to each other with the radiative transport models: Discrete Transfer Method (DTM) and P_1-moment method (P_1) and Coppalle’s [90] WSGG spectral model. The intention of the CH_4-O_2 CFD study is to reveal the impact of the propellant, i.e. methane vs. hydrogen, on the radiative heat transfer within the gas and especially the radiative energy exchange between the hot gas and the combustion chamber wall. As illustrated in Fig. 32 the total wall heat flux (TWHF) of methane is in average 25.1 % (absolute $2.01 \cdot 10^7\ \mathrm{W/m^2}$) lower compared to hydrogen. This follows from the higher reaction enthalpy of the LH_2-LO_2 combustion system due to the higher specific energy of hydrogen which results into a higher average gas temperature inside the combustion chamber; see Tabs. 7 and 8. As the radiative heat transfer is governed by temperature's fourth power, temperature-differences significantly affect the radiative heat transfer. Therefore the average TWHF of the H_2-O_2 system must be higher compared to the CH_4-O_2 case.

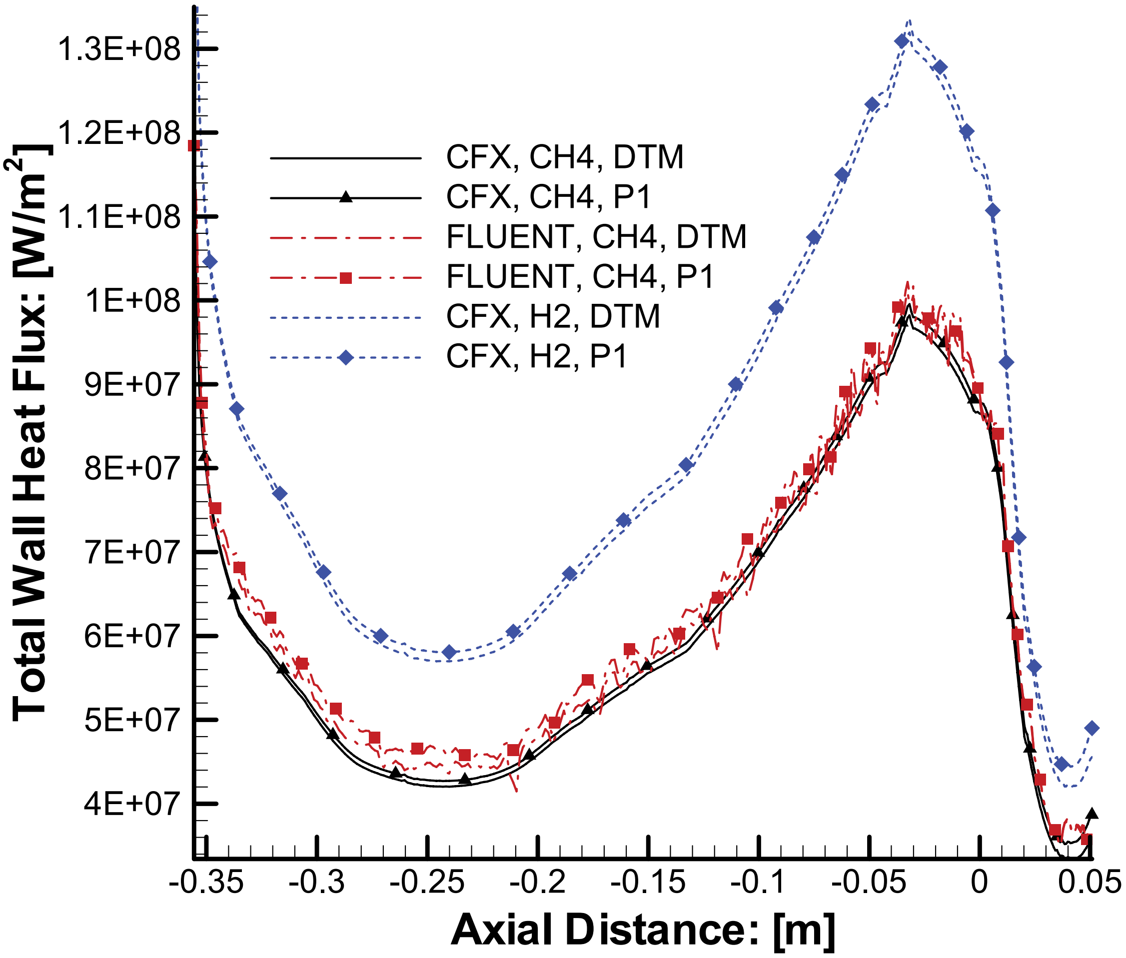

Figure 32: CH_4-O_2 study - TWHF for the DTM and P_1 transport models and for Coppalle's [90] WSGG model

Figures 32 and 33 imply that the P_1-moment method leads to higher wall heat fluxes compared to the Discrete Transfer Method (DTM). This behaviour was also observed for the H_2-O_2 case and might result from the fact that the P_1 radiative heat transfer is influenced more significantly by the neighbour cells close to the solid wall because of the diffusive characteristics of the P_1 method. The radiative wall heat flux (RWHF) from FLUENT is 24.4 % (absolute $1.04 \cdot 10^6\,\mathrm{W/m^2}$) higher on average compared to CFX. This difference is assumed to result from Edwards' [98] pressure-scaling rules which are included by default in FLUENT for Coppalle's [90] WSGG model. Coppalle's model in its original version is designed for a reference pressure of 1 atm, the pressure-scaling rules of Edwards account for higher gas pressures. The oscillations of FLUENT's P_1 calculation result from undamped numerical disturbances due to the high cell aspect ratio close to the wall and have no physical meaning. The RWHF distribution of the CH_4-

O_2 study is qualitatively consistent with the H_2-O_2 system and quantitatively in the same order of magnitude, although the total wall heat flux is smaller compared to the H_2-O_2 case.

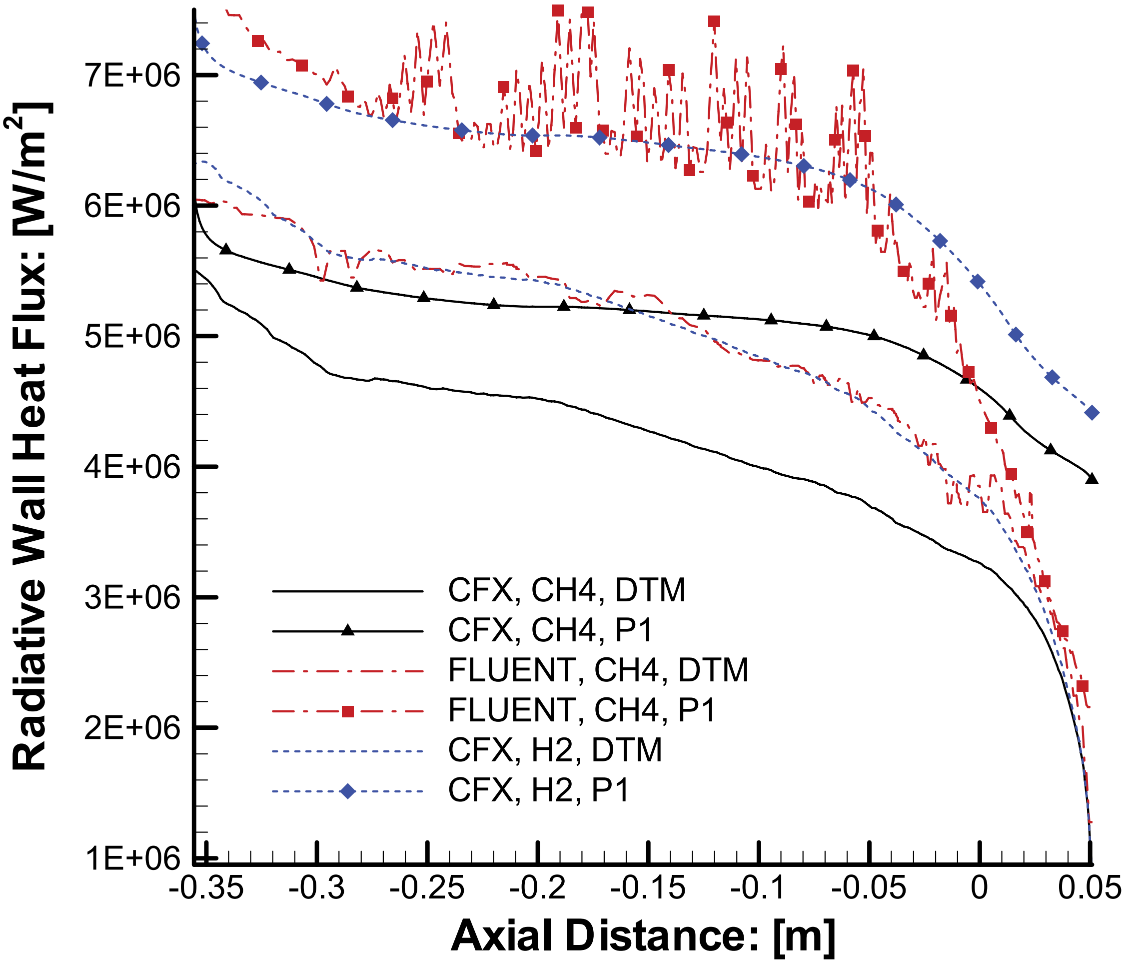

Figure 33: CH_4-O_2 study - RWHF for the DTM and P_1 transport models and for Coppalle's [90] WSGG model

6.5.2 Comparison of Different WSGG Models with CFX for $y^+_{\mathrm{ave}} \leq 1$

In this subchapter the influence of different WSGG models and WSGG conditions on the CFD solution is investigated with respect to the CH_4-O_2 case. The WSGG models with a limiting pressure of 1 atm qualitatively show the same behaviour as in the H_2-O_2 case. The limit of 100 atm for the Denison model results from Denison's [75] approach and is seen as a physical limit for the usability of his model. To investigate the behaviour of Denison's model above this pressure limit, a P_1-Denison-No-Limit calculation is performed. The quantitative difference between the P_1-Denison-100-atm-limit and "No Limit" RWHF-distribution is small as depicted in Fig. 34, however, it demonstrates that a higher partial pressure of the radiating species leads to a higher radiative wall heat flux (RWHF). According to the H_2-O_2 system, the DTM-Denison-100-atm-limit case is selected as the "best of" case for the CH_4-O_2 CFD study. As shown in Fig. 34 Denison in general induces a higher RWHF compared to Coppalle due to the validity of

Denison's model for higher operating pressures. The reason for the lower RWHF with respect to the Coppalle case is related to the total absorption coefficient and will be discussed later on in this subchapter. It should be noted that Coppalle on average underestimates the amount of the RWHF, while the P_1 transport model slightly overestimates the RWHF.

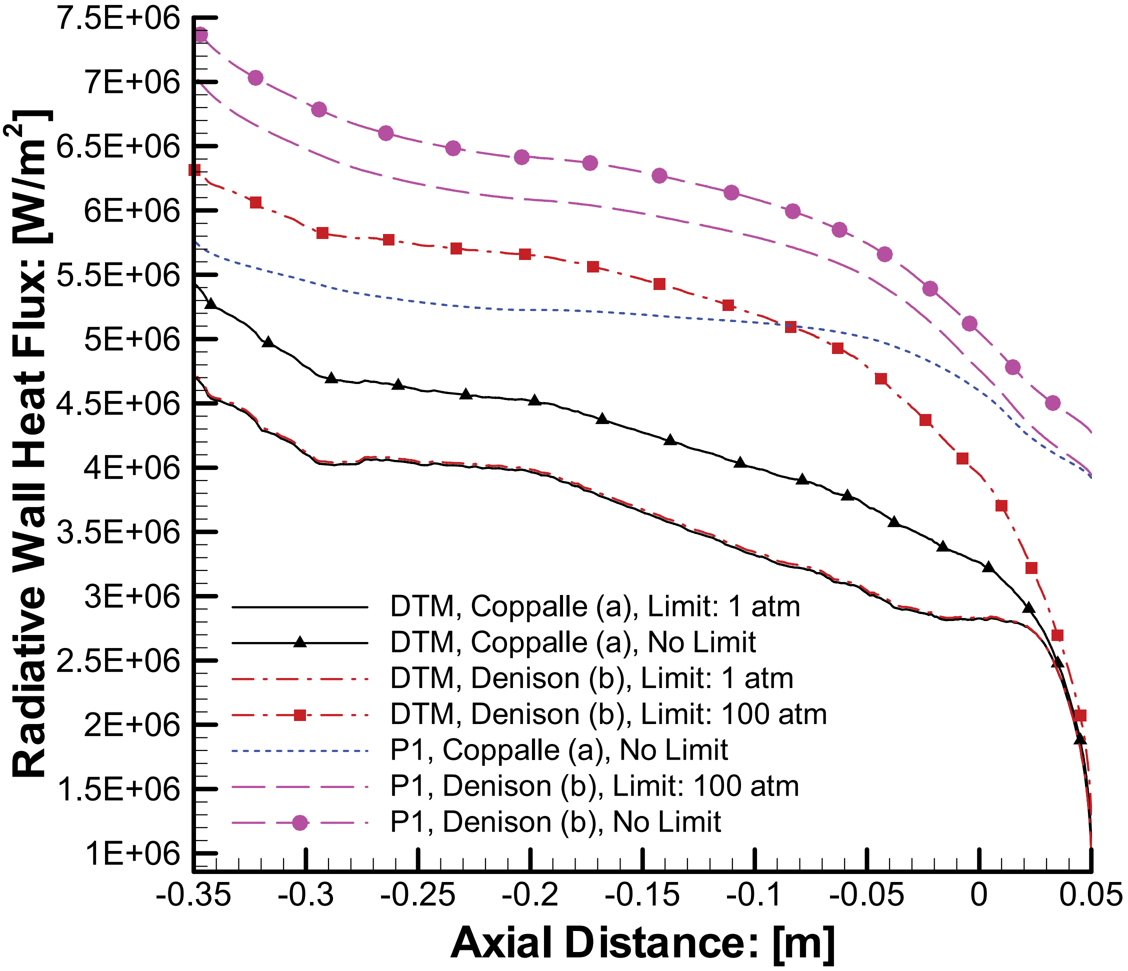

Figure 34: CH_4-O_2 study - RWHF from CFX, for the DTM transport model and for different WSGG models; (a) = [90] and (b) = [75]

Figure 35 reveals that the average amount of the radiative wall heat flux (RWHF) with regard to the total wall heat flux (TWHF) is about 8.8 %. The CH_4-O_2 CFD study reveals a slightly higher impact of the RWHF, compared to the H_2-O_2 system. As the average gas temperature in the combustion chamber of the CH_4-O_2 case is lower due to the lower mass-specific energy of methane, the higher RWHF can only result from the additional contribution of the strong radiator, CO_2. This confirms the initial assumption that using the fuel methane instead of hydrogen increases the influence of gas radiation on the overall heat transfer. The influence of the methane-gas-radiation increases only slightly due to the lower adiabatic gas temperature in the methane combustion system. Thus, for the novel methane rocket engine the impact of gas radiation would increase for higher operating conditions, i.e. temperatures and pressures.

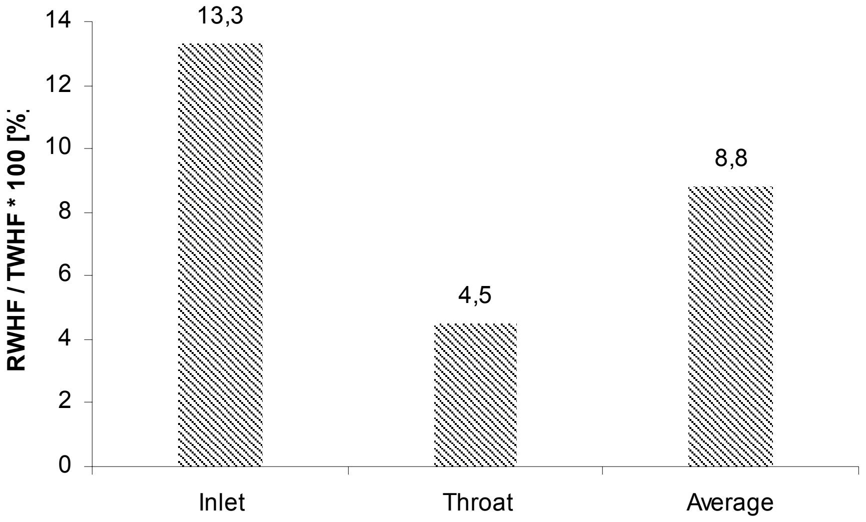

Figure 35: CH_4-O_2 study - Influence of the radiative on the total wall heat flux for CFX with DTM and Denison's [75] SLWSGG model for 100 atm

In Fig. 36 it can be observed that the radiative transport models, P_1 vs. DTM, only have a minor impact on the total absorption coefficient (TAC), i.e. both distributions are nearly identical. Furthermore, Fig. 36 shows that the TAC from Coppalle is almost twice as high compared to the more complex model from Denison.

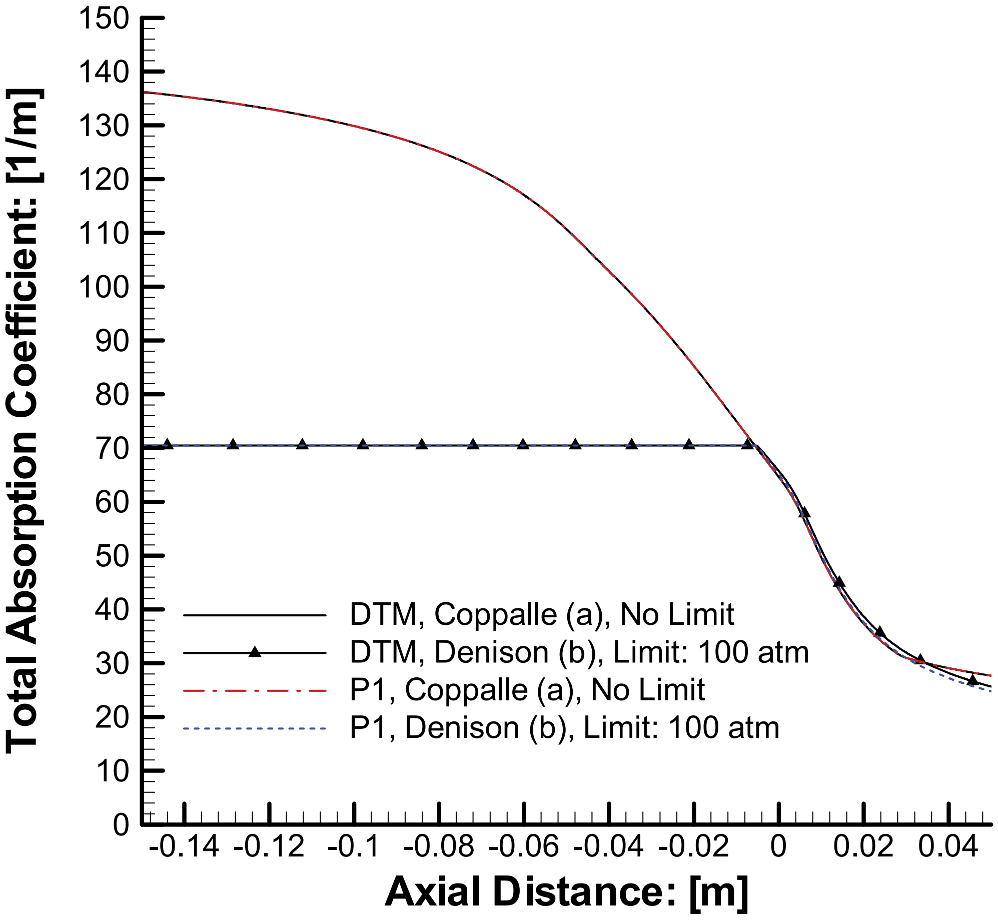

Figure 36: CH_4-O_2 study - Total absorption coefficient from CFX with the DTM and P_1 transport models and for y = 0.133 m = const; (a) = [90] and (b) = [75]

Close to the throat (axial distance = 0 m) both distributions along the constant line of a radial distance of 0.133 m immerse into the boundary layer of the SSME main combustion chamber, and fit better due to the smaller local gas temperatures. This observation indicates that the higher the gas temperature the greater the difference of Coppalle's and Denison's model.

The reason can be found in the strong temperature dependence of the weighting factors in the WSGG approach as stated in Eq. (77). Another result is the fact that a higher total absorption coefficient (TAC) leads to a lower radiative wall heat flux (RWHF) as illustrated in Fig. 34. This effect is related to the influence of the TAC on the thermal boundary layer thickness of the nozzle-flow. A higher TAC in Coppalle's model induces a thicker thermal boundary layer which in turn reduces the heat transfer to the chamber wall. Hence, Coppalle's model with its much higher total absorption coefficient underpredicts the radiative wall heat flux and thus the TWHF which is the sum of convective and radiative wall heat flux.

Table 11 lists the significant optical quantities for the methane case. In the novel CH_4-O_2 combustion chamber the photons travel a mean free path of 0.015 m on average which is nearly only half the distance compared to the H_2-O_2 rocket chamber where the penetration distance is 0.027 m; see Tab. 10. This comparison reveals that the radiating species CO_2 plays an important role for hydrocarbon fuels even when scattering is neglected, significantly affecting the "transport" characteristics of the radiative heat transfer.

Table 11: CH_4-O_2 study - Characteristic optical properties of the gas mixture from CFX with the DTM transport model, for the cylindrical section of the combustion chamber

	Coppalle [90] (No Limit)	Denison [75] (Limit = 100 atm)
Average total absorption coefficient a [1/m]	134	68
Average total optical thickness κ [-]	62	32
Average penetration distance $\tilde{S}$ [m]	0.007	0.015

Figure 37 qualitatively illustrates the two-dimensional distribution of the radiation intensity in the novel CH_4-O_2 combustion chamber. The highest intensity is near the inlet where the gas temperature has its maximum value. With increasing axial distance the gas is accelerated in x-direction and temperature decreases. Due to the strong temperature dependence radiation intensity must also decrease, as observed in Fig. 38.

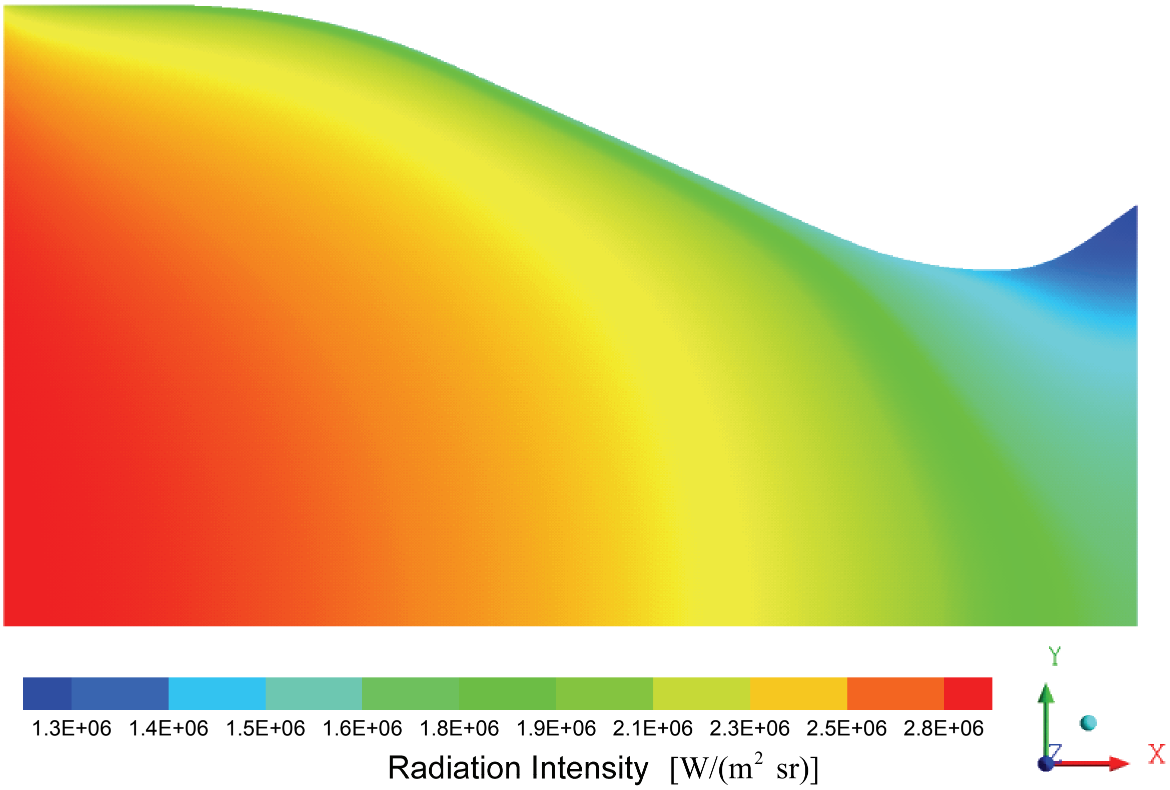

Figure 37: CH4-O2 study - Radiation Intensity for the P1 transport model and Denison's [75] 100 atm SLWSGG model

The amount of transferred radiative energy is not only dependent on pressure, temperature and species concentration of the radiating gas, but also on the characteristic radiating gas volume. The temperature difference in axial direction between the inlet and the outlet is smaller than in radial direction between the hot gas and the cooled wall, but the radiating volume fraction in axial direction is larger. Thus, a considerable amount of radiative energy is transferred in axial direction (x-direction) from the hot gas zone to the colder region. As mentioned before, the temperature gradient between the cooled solid wall and hot gas is high, however, the characteristic volume fraction in which the temperature differences occur is small compared to the axial direction. It is a common assumption that the overall heat transfer in axial direction is dominated by convection in case of a rocket combustion chamber. Heat conduction in axial direction is therefore often neglected, as it is assumed that there is only major heat conduction normal to the flow direction due to the high temperature gradients normal to the cooled solid wall. The radiative heat transfer is elliptic in space from a mathematical perspective, similar to heat conduction, but in contrast it significantly affects the axial overall heat transfer.

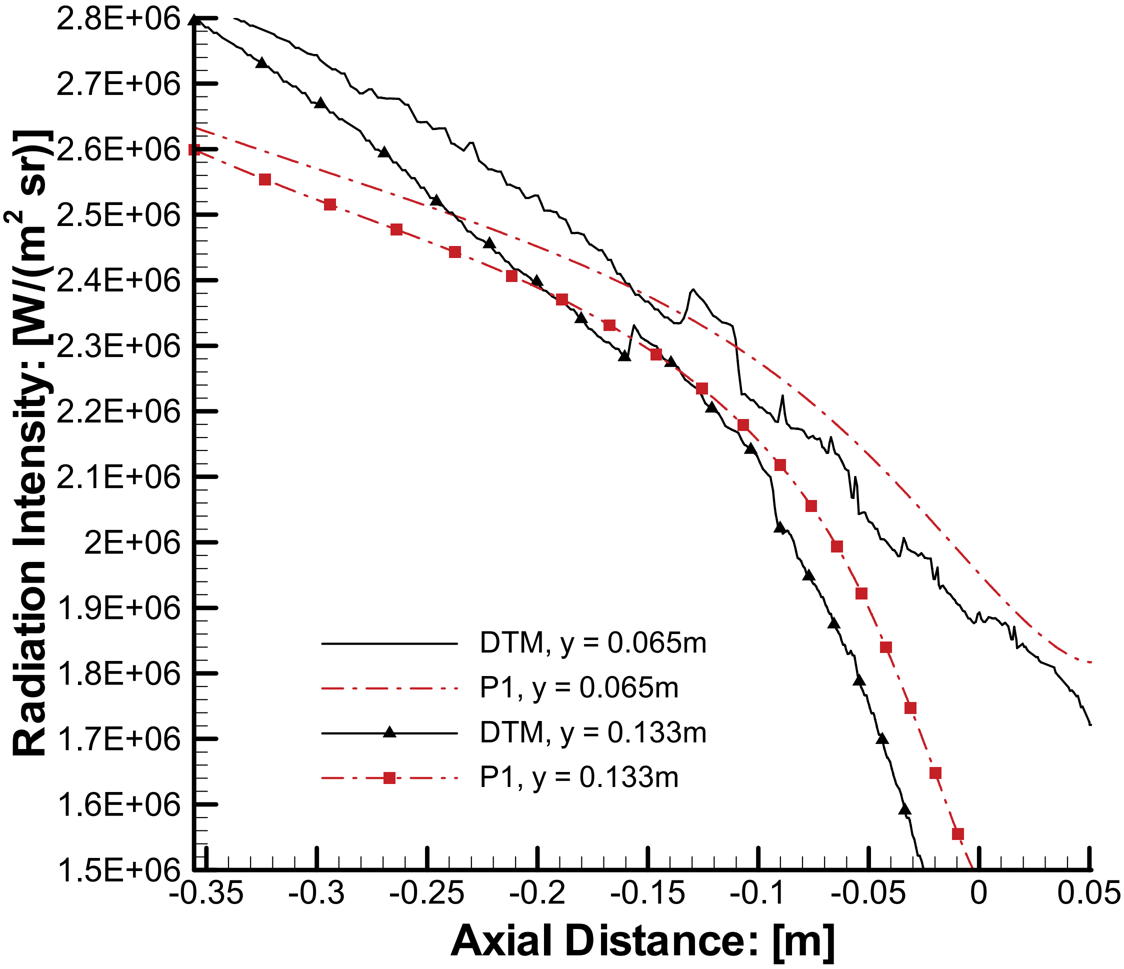

Figure 38: CH_4-O_2 study - Radiation Intensity for the DTM and P_1 transport models and Denison's [75] 100 atm SLWSGG model

Additionally, Figs. 38 and 39 investigate the one dimensional distribution of the radiation intensity along three constant lines of sight: (1) in axial direction for $y = 0.065$ m and (2) $y = 0.133$ m and in radial direction at (3) $x = 0$ m (throat). The first line corresponds to a nearly undisturbed flow, i.e. which is not significantly influenced by the solid wall; the second line touches the thermal boundary layer near the throat and the third line covers the entire range from the solid wall to the main flow. Both transport models, the P_1 and the DTM, qualitatively calculate distributions of similar intensity as illustrated in Fig. 38. In the inlet region where higher gas temperatures are present; the Discrete Transfer Method (DTM) induces a higher radiation intensity compared to the P_1-moment method. Figure 39 indicates numerical problems of the DTM close to the axis-symmetric line (radial distance = 0 m). The DTM is based on the approach that discrete rays of photons leave a solid wall and are tracked within the medium. Due to the presence of an axis-symmetric surface it has to be ensured that the gradients of intensity are zero normal to the symmetry line. Fulfilling this requirement is more complicated regarding the DTM due to its ray-based approach and the fact that the angles of the rays entering the first interior cell adjacent to the symmetry line are not perpendicular to the axis-symmetric boundary.

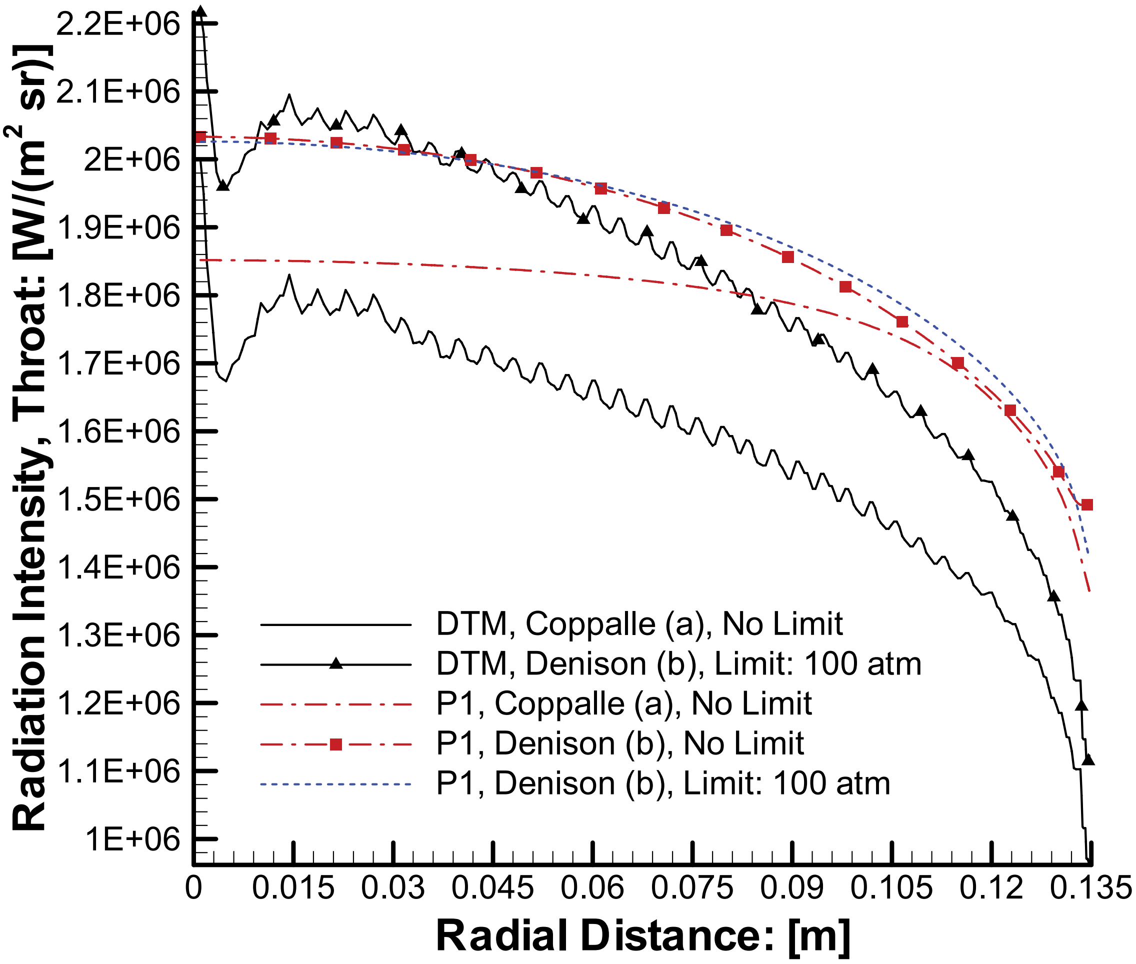

Figure 39: CH_4-O_2 study - Radiation Intensity for the DTM and P_1 transport models and for different WSGG models; (a) = [90] and (b) = [75]

Figure 39 additionally indicates that the influence of different "transport" characteristics resulting from different total absorption coefficients, see Fig. 36, i.e. Coppalle vs. Denison, affects the distribution of intensity to a greater extend than the type of radiative transfer model, i.e. DTM vs. P_1. This observation is an important result which was also confirmed by the research group under the leadership of Klar and Pinnau within the scope of the SFB 568 report [39]. In other words, a more accurate modelling of the spectral properties (e.g. Coppalle vs. Denison) has a greater impact on the prediction of the radiative heat transfer than higher-level (and more CPU-intensive) radiative transfer modelling (e.g. P_1 vs. DTM).

7 Conclusions and Outlook

7.1 General Comments

The aim of this thesis is the investigation of the influence of thermal gas radiation on the heat loads in a rocket combustion chamber. The survey is performed numerically, based on the method of Computational Fluid Dynamics (CFD). In this context the commercial ANSYS CFX and FLUENT CFD solvers and the NSMB CFD research code are applied. For the numerical simulation of radiative heat transfer two basic research areas are essential. Firstly, the transport of radiative energy needs to be approximated and secondly, the spectral dependence of the transport quantities must be modelled.

Considering CFX and FLUENT, the P_1 (P_1-moment method) and the DTM (Discrete Transfer Method) radiative transport models have already been implemented and are used "off-the-shelf" within the scope of this thesis. Including the radiative transport models, in particular the DTM increase CPU costs. Thus, one aim of this thesis is to study under which conditions less CPU-intensive transport models can be applied. Analytic calculations and a literature study indicated that the optical properties in a rocket combustion chamber can be treated as optically thick, and based on that assumption the use of diffusive transport models seems to be possible under certain restrictions. The Rosseland Radiation Model (RRM) belongs to the group of diffusive approximations of the radiative transfer equation and can be conveniently integrated into a CFD solver. Hence, this model is implemented into the NSMB CFD solver and validated for a simple test case, showing a good fit between the numerical and the analytical solution.

For the spectral modelling of the transport quantities the challenge is to take into account the strong frequency dependence of the absorbing and emitting gas. Due to the absence of suspended particles in the gas mixture of a hydrogen-oxygen rocket chamber scattering is neglected. To identify a suitable spectral approximation a literature survey is performed indicating that the weighted-sum-of-gray-gases (WSGG) approach is well qualified for a rocket combustion chamber. Several enhanced WSGG models are identified and compared with an Excel based tool (EBCOW) prior to their implementation into the CFD solver. Various WSGG models are implemented in both CFX, respectively NSMB CFD solvers. In order to use the WSGG model in conjunction with the Rosseland model in NSMB, the theory of the Rosseland approximation was extended and newly derived. Correspondence with Howell [70] and Modest [110] confirmed the derived, coupled relations for Rosseland and the WSGG approach.

In the next step a practical test case was required. For this purpose, the main combustion chamber of the Space Shuttle Main Engine (SSME) was identified. Due to the high operating pressure ($\approx$ 21 MPa), high adiabatic gas temperature ($\approx$ 3800 K), high concentration of water vapour (which is a strong radiator) and large radiating gas volume, the SSME main combustion chamber is well qualified for the demonstration of the impact of gas radiation. In this context a detailed literature survey was performed, considering the numerical analysis of radiative heat

transfer in liquid rocket engines. The literature survey revealed the studies of Naraghi et al. [20] and Wang [21] which are used as benchmark within this thesis.
In a first step the SSME main combustion chamber was simulated with CFX and FLUENT to get a first impression of the impact of gas radiation on flow dynamics and total wall heat flux. In a second step the simulation environment was successively improved. This was achieved mainly by using the $k-\omega$ low Reynolds turbulence model for the boundary layer and $k-\varepsilon$ only for the main flow. An intensive mesh study revealed that the wall quantities can only be resolved properly for a wall resolution in the order of 10^{-8} m for the distance from the solid wall to the first interior mesh node.

After the validation of the stand-alone Rosseland Radiation Model (RRM) in NSMB, the Rosseland approximation and the WSGG approach where applied to the SSME main combustion chamber. The coupling of the Rosseland model with the flow dynamics revealed the disadvantages of the Rosseland boundary condition for solid walls. According to the theory it is known that for the coupling of heat conduction and radiation a jump boundary condition can be introduced within the Rosseland approach. This jump relation was developed further in the scope of this thesis in order to take more into account the flow dynamics and to improve the quantitative prediction of the radiative wall heat flux.

7.2 Summary of the Results

Two combustion systems are studied in order to investigate the impact of gas radiation on the flow field and wall heat loads of a rocket combustion chamber. In the first case the original liquid hydrogen-oxygen (LH_2-LO_2) SSME main combustion chamber is simulated. During the combustion of hydrogen and oxygen water vapour is produced which is known as strong radiating species. Due to the fact that hydrocarbon fuels are presumed to offer several advantages compared to hydrogen, see subchapter 1.1, a novel methane-oxygen (LCH_4-LO_2) combustion chamber is simulated and the results are compared with the LH_2-LO_2 system. During the methane-oxygen combustion carbon dioxide (CO_2) is produced additionally to water vapour; both species are strong radiators. In order to compare both systems, the thrust of the rocket engine at the throat is used as reference quantity. The combustion of the liquid reactants is simulated by the equilibrium chemistry code CEA [100], also known as “Gordon and McBride”. The thermodynamic state and the species concentration of the combusted gas mixture from the CEA code is used as the inflow boundary condition for the CFD simulations. Although an almost perfectly premixed and combusted gas mixture enters the computational domain at the inlet, the total wall heat flux increases about 2% on average when the equilibrium-chemistry Eddy Dissipation Model (EDM) is activated.

Within the scope of this thesis it was proven that the inclusion of gas radiation only has minor impact on the dynamics of the flow. The influence of gas radiation on the engine thrust and on the average gas temperature in the core flow is neglectable. However, in the laminar viscous sublayer the temperature is increased due to radiation, resulting in a higher temperature gradient adjacent to the solid wall. The thermal boundary layer thickness is increased slightly due to gas radiation. The inclusion of gas radiation causes the axial temperature to decrease on average for approximately $2\ \mathrm{K}$ in the central region of the nearly undisturbed flow. Additionally, it was found that gas radiation only has small influence on the wall shear stress. Therefore, a considerable interaction between gas radiation and turbulence cannot be confirmed in this thesis. This observation probably results from the fact that all CFD calculations are carried out based on the Reynolds-Averaged-Navier-Stokes (RANS) equations.

Taking these results into account and keeping in mind that gas radiation only has a minor influence on the central flow, the investigation of the interaction between gas radiation and chamber wall was intensified. Within this survey the total wall heat flux (TWHF) and the radiative wall heat flux (RWHF) play an important role. An accurate prediction of the wall heat loads is important for estimating engine life, especially with regard to future re-useable rocket engines.

Considering the CFD calculations of the H_2-O_2 system using semi-empirical scalable wall functions within the turbulence modelling and applying an average dimensionless distance of $y^+_{\mathrm{ave}} \approx 280$, results in significant differences between CFX and FLUENT. The relative TWHF-difference between CFX and FLUENT is approximately 60 %. The relative TWHF-difference to the benchmark of Naraghi et al. [20] depends on the CFD solver, and is for CFX about 50 % and for FLUENT about 20 %. The quantitative differences between the CFD solver become smaller for an average dimensionless distance of $y^+_{\mathrm{ave}} \leq 1$.

An intensive mesh study reveals that for a $y^+_{\mathrm{ave}} < 2$, the total wall heat flux becomes independent of wall resolution. For the representative calculations a value of $y^+_{\mathrm{ave}} \leq 1$ is applied to safely achieve the required target y^+ of the used turbulence models. Due to the high Reynolds number of about $2.9 \cdot 10^8$ and the resulting thin laminar sublayer, a geometrical wall resolution of $\approx 1 \cdot 10^{-8}\,\mathrm{m}$ is required between the solid wall and the first interior mesh node in order to obtain an average $y^+_{\mathrm{ave}} \leq 1$. The very fine wall mesh allows the resolution of the near-wall region all the way down to the solid wall instead of applying the more inaccurate wall function approach which does not resolve the viscosity-affected laminar sublayer. This approach enabled an improved quantitative distribution of the TWHF of the CFX and FLUENT results. Nevertheless, the NSMB results fit the benchmark distribution of the TWHF better, although the Spalart-Allmaras turbulence model is only a one-equation model. In contrast to NSMB, CFX and FLUENT use Menter's Shear Stress Transport (SST) version of the $k-\omega$ two- equation turbulence model.

Within the CFD study the influence of different CFD solvers (CFX, FLUENT and NSMB), different radiative transport models (DTM, P_1 and RRM), different combustion systems (H_2-O_2 vs. CH_4-O_2) and different selected spectral WSGG models (Smith, Denison, Coppalle) on the total and radiative wall heat flux is investigated intensively.

The results reveal that for the best of case (CFX/DTM/Denison), the contribution of gas radiation to the total wall heat flux (TWHF) of the H_2-O_2 system is 7.7 % on average; the contribution of gas radiation to the TWHF of the CH_4-O_2 system is 8.8 % on average. Hence, the impact of gas radiation on the TWHF is higher in the CH_4-O_2 study, although the TWHF of the CH_4-O_2 system is 25 % lower compared to the H_2-O_2 case due to the lower specific energy of methane. Furthermore, the spectral-line-weighted-sum-of-gray-gases model (SLWSGGM) of Denison at an elevated pressure of 100 atm is identified as the "best of" spectral model regarding the current CFD problem.

Considering the radiative transport models it was found that the P_1 model overestimates the amount of the radiative wall heat flux (RWHF) in comparison to the DTM. The Rosseland model reveals that gas radiation contributes 32 % on average to the total wall heat flux. The NSMB-Rosseland model with the enhanced jump boundary condition provides better results than the standard jump condition of CFX. Considering the finest wall resolution, i.e. $y^+_{\mathrm{ave}} \leq 1$, it was not possible to achieve a converged solution with CFX and Rosseland. This results from the fact that the CFX standard jump boundary condition of Rosseland induces unphysically high radiative wall heat fluxes. As expected the most accurate results (compare to the benchmark) are generated by the DTM.

The inclusion of radiative heat transfer increases the computational costs significantly for all three CFD solvers. Considering the H_2-O_2 study and applying Smith's WSGG model, the NSMB-RRM combination increases the total CPU time by approximately 22 %, CFX-P_1 by 51 % and CFX-DTM by 466 % compared to a calculation without radiation. The highest CPU time increase is obtained for the CFX-DTM case in conjunction with Denison's SLWSGG model instead of Smith, leading to 992 % more CPU time.

7.3 Further Study

The focus of this thesis is the accurate prediction of the impact of gas radiation on the flow dynamics and wall heat loads in a rocket combustion chamber. Considering the modelling of the radiative heat transfer the greatest potential is considered to be in the improvement of the spectral modelling. Based on the weighted-sum-of-gray-gases (WSGG) approach Denison's models are identified as "best of" models for the present CFD problem. Nevertheless, the models are limited for a pressure of 100 atm and a gas temperature of 2500 K. This is a good starting point to further identify spectral models which are valid for higher pressure and temperature regimes. In this context the Full Spectrum *k*-Distribution correlations by Modest [4] should be taken into account. Within the scope of the literature survey of the spectral models it was found that the experimental validation of the WSGG models only applies to atmospheric pressures. To the author's knowledge, WSGG models for higher pressures have been theoretically derived only rather than experimentally validated.

The second important field of enhancement is the modelling of the radiative transport. The high CPU time for the DTM reveals the requirement for faster approximations of the radiative transfer equation. It was found that the Rosseland approximation overpredicts the radiative wall heat flux, however, it requires the lowest CPU time. Although Modest [110] suggests that the standard Rosseland approximation should never be used for gas radiation, the jump boundary condition of Rosseland should be further investigated, respectively improved; since a more realistic jump condition could allow the use of the Rosseland model with respect to gas radiation in a combustion chamber.

Howell [70] points out that currently it is not known how to apply realistic boundary conditions for Rosseland if flow is present, and radiation is coupled to forced convection and heat conduction. It seems that an analytic boundary condition for the coupled Rosseland case does induce a significant overprediction of the wall heat loads. An empirical approximation of the jump boundary condition for the Rosseland model may help to solve the problem. If this is not possible, the moment-based transport models (P_1 / M_1 [39] and higher-order) should be investigated further and coupled to more accurate spectral models.

Considering the influence of gas radiation on the flow dynamics the turbulence-radiation and chemistry-radiation interactions should be studied further. Considering a rocket combustion chamber, complex physical phenomena occur in the region where the reactants are injected. Within a few millimetres the reactants change their state from supercritical condition to a thermal ideal gas mixture. Due to the fact that gas radiation induces a strong heat transfer in upstream direction, heat transfer from gas radiation may influence the real gas effects in the injection area.

It should be further investigated which influence a structure-fluid coupling has on the thermal boundary layer, when gas radiation is included assuming a Neumann boundary condition in contrast to the present Dirichlet boundary condition. For the Neumann boundary condition an energy flux balance at the chamber wall is necessary including the convective heat flux of the wall-cooling fluid.

Appendices

A. Notation of a 2D Grid with 2x2 Cells in NSMB

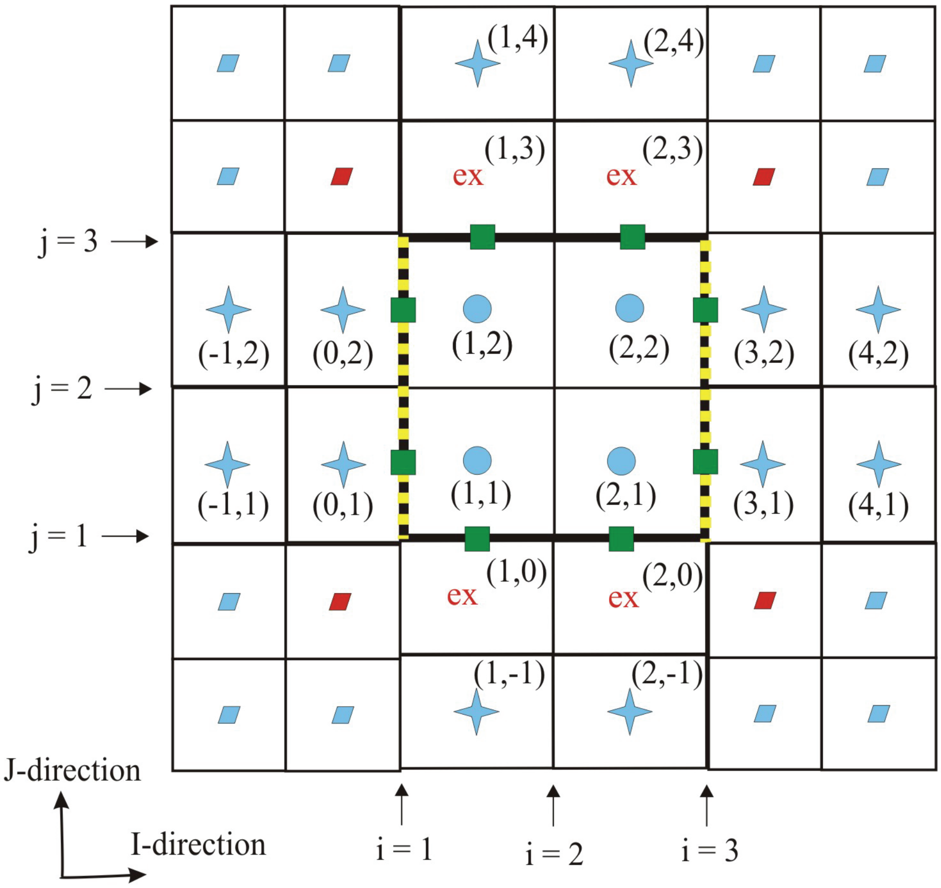

● cell centre, from interior cell (i,j)

✦ cell centre, from ghost cell edge (i,j)

▰ cell centre, from ghost cell corner (i,j)

🟩 surface centre

┅ permeable boundary

▬ solid boundary / wall

cells: n1 x n2 = 2 x 2

coordinates (nodes): imax x jmax = 3 x 3

temperature array: t (i,j,k)

🟦 T_0: free stream temperature

🟥 T_{wall}: solid wall temperature from user input

extrapolation of wall temperature to first ghost cell:

ex : extrapolated wall temperature

$T_{ex}(1,0) = 2*T_{wall} - T(1,1)$

B. Geometry of the SSME main combustion chamber

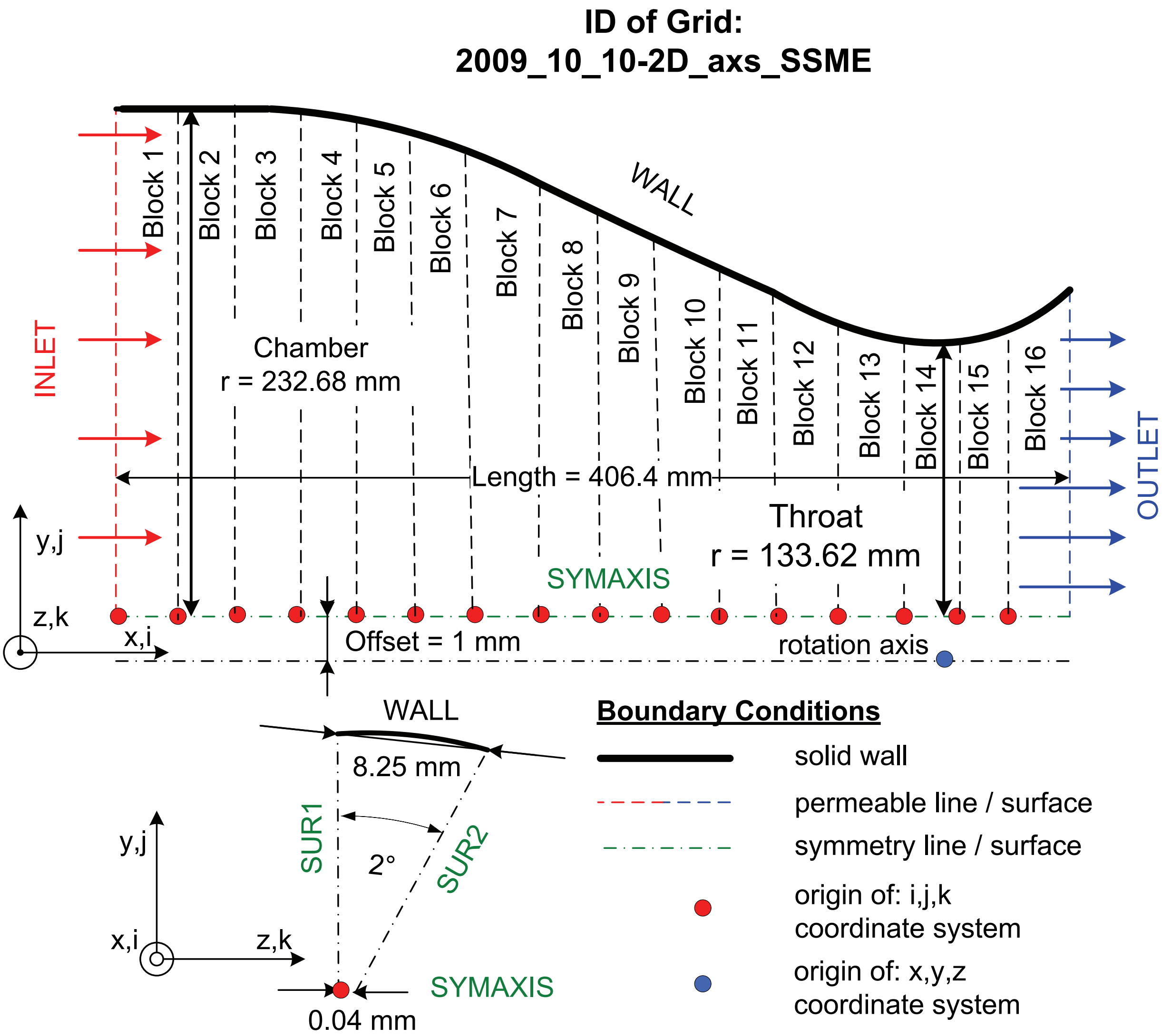

Description:

Mesh Type:
-> Hexahedral, total number of **cells**: 142848 (with k = 1) and 285696 (with k = 2)
-> CFX / FLUENT: Mesh is exported as unstructured mesh with k = 1 cell.
-> NSMB: Mesh is exported as Multiblock mesh (16 Blocks) with k = 2 cells.

Blocks 1-16:
-> Number of finite volume **cells**: i = 24; j = 372; k = 1 (CFX/FLUENT) or k = 2 (NSMB)
-> Nodes distribution in direction:

i:	j:	k:
Mesh law: uniform/exponential	Mesh law: exponential	Mesh law: uniform
max. cell space = 1.7 mm	cell space (j=1) = 0.49 mm	cell space = variable
	cell space (j=372) = 1.0E-5 mm	
	Max. growth ratio: 1.26	

Bibliography

1. Pai, S. I., Radiation Gas Dynamics, Springer Verlag, 1966.
2. Penner, S. S. and Olfe, D. B., Radiation and Reentry, Academic Press, 1968.
3. Hottel, H. C. and Sarofim, A. F., Radiative Transfer, McGraw-Hill Book Company, 1967.
4. Modest, M. F., Radiative Heat Transfer, Second Edition ed., Academic Press, San Diego (USA), London (UK), Burlington (USA), 2003.
5. Siegel, R. and Howell, J. R., Thermal Radiation Heat Transfer - 4th ed., Taylor & Francis, 2002.
6. Seaid, M., Klar, A., and Pinnau, R., Numerical Solvers for Radiation and Conduction in High Temperature Gas Flows, Journal of Flow Turbulence and Combustion, Vol. 75, pp. 173-190, 2005.
7. Hartung, L. C., Nonequilibrium Radiative Heating Prediction Method for Aeroassist Flowfields with Coupling to Flowfield Solvers, Raleigh, North Carolina State University, Department of Mechanical and Aerospace Engineering, 1991.
8. Höld, R. K. and Fornasier, L., Investigation of Thermal Loads on Hypersonic Vehicles with Emphasis on Surface Radiation Effects, München, Deutsche Aerospace AG - Military Aircraft Division, 1994.
9. Ozawa, T., Garrison, M. B., and Levin, D. A., Accurate Molecular and Soot Infrared Radiation Model for High-Temperature Flows, Journal of Thermophysics and Heat Transfer, Vol. 21, No. 1, pp. 19-27, 2007.
10. Capra, B. R., Aerothermodynamic Simulation of Subscale Models of the FIRE II and Titan Explorer vehicles in Expansion Tubes, PhD Thesis, University of Queensland, School of Engineering, 2007.
11. Sutton, G. P. and Biblarz, O., Rocket Propulsion Elements - 7th edition, John Wiley & Sons, 2001.
12. Reck, R. J. e. al., Delta 269 - failure investigation summary report, The Boeing Company, 1999.
13. Arianespace, press information, from 07.01.2003, http://www.arianespace.com/news-press-release/2003/01-07-03-Arianespace_Flight_157_The_Inquiry_Board.asp, 07.05.2010, 15:00,
14. Haarmann, T. M., Numerische Simulation des Wärmeübergangs in einer kryogenen Raketenbrennkammer, PhD thesis, RWTH Aachen, 2006.
15. Ludwig, C. B., Malkmus, W., Reardon, J. E., and Thomson, J. A. L., Handbook of infrared radiation from combustion gases - NASA-SP-3080, Marshall Space Flight Center, 1973.

16. Greenwood, T. F., Lee, Y. C., Bender, R. L., and Carter, R. E., Space Shuttle Base Heating, Journal of Spacecraft and Rockets, Vol. 21, No. 4, pp. 339-345, 1984.

17. Badinand, T. and Fransson, T. H., Radiative Heat Transfer in Film-Cooled Liquid Rocket Engine Nozzles, Journal of Thermophysics and Heat Transfer, Vol. 17, No. 1, pp. 29-34, 2003.

18. Nelson, H. F., Radiative Heating in Scramjet Combustors, Journal of Thermophysics and Heat Transfer, Vol. 11, No. 1, pp. 59-64, 1997.

19. Liu, J. and Tiwari, S. N., Radiative Heat Transfer Effects in Chemically Reacting Nozzle Flows, Journal of Thermophysics and Heat Transfer, Vol. 10, No. 3, pp. 436-444, 1996.

20. Naraghi, M. H., Dunn, S., and Coats, D., Modeling of Radiation Heat Transfer in Liquid Rocket Engines, AIAA-2005-3935, Joint Propulsion Conference, Arizona, 2005.

21. Wang, T.-S., Multidimensional Unstructured-Grid Liquid Rocket-Engine Nozzle Performance and Heat Transfer Analysis, Journal of Propulsion and Power, Vol. 22, No. 1, pp. 78-84, 2006.

22. Melcher, J. C. and Allred, J. K., Liquid Oxygen / Liquid Methane Test Results of the RS-18 Lunar Ascent Engine at Simulated Altitude Conditions at NASA White Sands Test Facility, 1-2-3456.

23. XCOR Aerospace, Unknown Author, http://www.xcor.com/products/engines/M15_LOX-Methane_rocket_engine.html, 01.01.2010, 15:59.,

24. Arnold, R., Suslov, D., and Haidn, O. J., Experimentelle Untersuchung zur Filmkühlung in einer Subscale-Brennkammer mit LOX/CH4-Vebrennung, Deutscher Luft- und Raumfahrtkongress, 2008.

25. Preclik, D., Hagemann, G., Knab, O., Mäding, C., Haeseler, D., Haidn, O., Woschnak, A., and DeRosa, M., LOX/Hydrocarbon Preparatory Thrust Chamber Technology Activities in Germany, 41st Joint Propulsion Conference, Tucson (Arizona), 2005.

26. Lux, J. and Haidn, O., Effect of Recess in High-Pressure Liquid Oxygen/Methane Coaxial Injection and Combustion, Journal of Propulsion and Power, Vol. 25, No. 1, pp. 24-32, 2009.

27. Lux, J. and Haidn, O., Flame Stabilization in High-Pressure Liquid Oxygen/Methane Rocket Engine Combustion, Journal of Propulsion and Power, Vol. 25, No. 1, pp. 15-23, 2009.

28. Locke, J. M., Pal, S., and Woodward, R. D., Chamber Wall Heat Flux Measurements for a LOX/CH4 Uni-element Rocket, 43rd AIAA/ASME/SAE/ASEE Joint Propulsion Conference and Exhibit, 2007.

29. Burkhardt, H., Sippel, M., Herbertz, A., and Klevanski, J., Comparative Study of Kerosene and Methane Propellant Engines for Reusable Liquid Booster Stages, 4th International Conference on Launcher Technology "Space Launcher Liquid Propulsion", Liège (Belgium), 2002.

30. Barry, P., Methane Blast, Science@NASA, 5-4-2007.

31. Boeing, Waverider Project, http://www.boeing.com/defense-space/military/waverider/index.html, date: 20.03.2010, 13:43 h,

32. Hank, J. M., Murphy, J. S., and Mutzman, R. C., The X-51A Scramjet Engine Flight Demonstration Program, 15th AIAA International Space Planes and Hypersonic Systems and Technologies Conference, 28 April - 1 May 2008, Dayton, Ohio, 2008.

33. Yan, W.-M. and Li, H.-Y., Radiation Effects on Mixed Convection Heat Transfer in a Vertical Square Duct, Int.J.Heat Mass Transfer, Vol. 44, No. 7, pp. 1401-1410, 2001.

34. Yih, K. A., Effects of Radiation on Natural Convection about a Truncated Cone, Int.J.Heat Mass Transfer, Vol. 42, No. 23, pp. 4299-4305, 2000.

35. Lan, C.-H., Ezekoye, O. A., and Howell, J. R., Computation of Radiative Combined-Mode Heat Transfer in a Two-Dimensional Rectangular Participating Medium Using the Spectral Method, Proc. 2000 Natl. Heat Transfer Conf., 2000.

36. Krishnaprakas, C. K., Narayana, K. B., and Dutta, P., Interaction of radiation with natural convection, Journal of Thermophysics and Heat Transfer, Vol. 13, No. 3, pp. 387-390, 1999.

37. Krishnaprakas, C. K., Narayana, K. B., and Dutta, P., Combined convective and radiative heat transfer in turbulent tube flow, Journal of Thermophysics and Heat Transfer, Vol. 13, No. 3, pp. 390-394, 1999.

38. Bataller, R. C., Viscoelastic fluid flow and heat transfer over a stretching sheet under the effects of a non-uniform heat source, viscous dissipation and thermal radiation, International Journal of Heat and Mass Transfer, Vol. 50, No. 15-16, pp. 3152, 2007.

39. Klar, A. and Pinnau, R., Projektergebnisse SFB 568, Teilprojekt D1: 2004-2007, Entwicklung und Analyse numerischer Verfahren für Strahlungstransportgleichungen und Kopplung strömungsdynamischer Gleichungen, TU Kaiserslautern, Fachbereich Mathematik, 2007.

40. Teleaga, I., Seaid, M., Gasser, I., Klar, A., and Struckmeier, J., Radiation models for thermal flows at low Mach number, Journal of Computational Physics, Vol. 215, No. 2, pp. 506-525, 1-7-2006.

41. Dubroca, B., Seaid, M., and Teleaga, I., A consistent approach for the coupling of radiation and hydrodynamics at low Mach number, Journal of Computational Physics, Vol. 225, No. 1, pp. 1039-1065, 1-7-2007.

42. Mazumder, S., Numerical study of chemically reactive turbulent flows with radiative heat transfer, Ph.D. thesis, University Park, PA, The Pennsylvania University, 1997.

43. Li, G., Investigation of turbulent-radiation interactions by a hybrid FV/PDF Monte Carlo Method, Ph.D. thesis, The Pennsylvania University, University Park, PA, 2002.

44. Faeth, G. M., Gore, J. P., Chuech, S. G., and Jeng, S. M., Radiation from turbulent diffusion flames, Annual Review of Numerical Fluid Mechanics and Heat Transfer, Vol. 2, pp. 1-38, 1989.

45. Mazumder, S. and Modest, M. F., A PDF approach to modeling turbulence-radiation interactions in nonluminous flames, International Journal of Heat and Mass Transfer, Vol. 42, No. 971, pp. 991, 1999.

46. Mazumder, S. and Modest, M. F., Turbulence-radiation interactions in nonreactive flow of combustion gases, ASME Journal of Heat Transfer, Vol. 121, No. 726, pp. 729, 1999.

47. Li, G. and Modest, M. F., Importance of Turbulence-Radiation Interactions in Turbulent Diffusion Jet Flames, ASME Journal of Heat Transfer, Vol. 125, pp. 831-838, 2003.

48. Gupta, A., Modest, M. F., and Haworth, D. C., Large-Eddy Simulation of Turbulence-Radiation Interactions in a Turbulent Planar Channel Flow, ASME Journal of Heat Transfer, Vol. 131, pp. 1-8, 2009.

49. Matsuyama, S., Ohnishi, N., Sasoh, A., and Sawada, K., Numerical Simulation of Galileo Probe Entry Flowfield with Radiation and Ablation, Journal of Thermophysics and Heat Transfer, Vol. 19, No. 1, pp. 28, 2005.

50. Wright, M. J., Bose, D., and Olejniczak, J., Impact of Flowfield-Radiation Coupling on Aeroheating for Titan Aerocapture, Journal of Thermophysics and Heat Transfer, Vol. 19, No. 1, pp. 17, 2005.

51. Whiting, E. E., Yen, L., Arnold, J. O., and Paterson, J. A., NEQAIR96, Nonequilibrium and Equilibrium Radiative Transport and Spectra Program: User's Manual, NASA RP-1389, 1996.

52. Feldick, A. M., Duan, L., Modest, M. F., Martin, M. P., and Levin, D. A., Influence of Interactions Between Turbulence and Radiation on Transmissivities in Hypersonic Turbulent Boundary Layers, 48th AIAA Aerospace Sciences Meeting Including the New Horizons Forum and Aerospace Exposition, 4 - 7 January 2010, Orlando, Florida, 2010.

53. Byun, D. and Baek, S. W., Numerical investigation of combustion with non-gray thermal radiation and soot formation effect in a liquid rocket engine, International Journal of Heat and Mass Transfer, Vol. 50, No. 3-4, pp. 412, 2007.

54. Naraghi, M. H. and Nunes, E. M., Effects of Gas Radiation on the Thermal Characteristics of Regeneratively Cooled Rocket Engines, ASME International Mechanical Engineering Congress, November 17.-22., 2002.

55. Naraghi, M. H. and DeLise, J. C., Conjugate Conductive, Convective and Radiative Heat Transfer in Rocket Engines, National Heat Transfer Conference, Vol. 5, 1995.

56. Naraghi, M. H. and Hammad, K. J., Exchange Factor Model for Radiative Heat Transfer Analysis in Rocket Engines, Journal of Thermophysics and Heat Transfer, Vol. 5, No. 3, pp. 327-334, 1991.

57. Naraghi, M. H. and Hammad, K. J., Radiative Heat Transfer in Rocket Thrust Chambers and Nozzles, AIAA 24th Thermophysics Conference, 1989.

58. Denison, M. K. and Webb, B. W., A Spectral Line-Based Weighted-Sum-of-Gray-Gases Model for Arbitrary RTE Solvers, Journal of Heat Transfer, Vol. 115, No. 4, pp. 1004-1012, ASME, 1993.

59. Wang, T.-S. and Luong, V., Hot-Gas-Side and Coolant-Side Heat Transfer in Liquid Rocket Engine Combustors, Journal of Thermophysics and Heat Transfer, Vol. 8, No. 3, pp. 524-530, 1994.

60. Anderson, J. D., Computational Fluid Dynamics, McGraw-Hill, New York, 1995.

61. Levermore, C. D., Relating Eddington Factors to Flux Limiters, Journal of Quantitative Spectroscopy & Radiative Transfer, Vol. 31, No. 2, pp. 149-160, 1984.

62. Eddington, A. S., The Internal Constitution of the Stars, Dover, New York, 1959.

63. Milne, F. A., Thermodynamics of the Stars, Handbuch der Astrophysik, No. 3, pp. 65-255, Springer-Verlag, Berlin, 1930.

64. Krook, M., On the Solution of the Equation of Transfer, Astrophysical Journal, Vol. 122, pp. 488-497, 1955.

65. Rosseland, S., Astrophysik auf atomtheoretischer Grundlage, Verlag von Julius Springer, Berlin, 1931.

66. Jeans, J. H., The Equations of Radiative Transfer of Energy, Monthly Notices Royal Astronomical Society, Vol. 78, pp. 28-36, 1917.

67. Rosseland, S., Theoretical Astrophysics - Atomic Theory and the Analysis of Stellar Atmospheres and Envelopes, Clarendon Press, Oxford, 1936.

68. Deissler, R. G., Diffusion Approximation for Thermal Radiation in Gases with Jump Boundary Condition, Journal of Heat Transfer, Vol. 86, No. 2, pp. 240-246, 1964.

69. Goldstein, M. and Howell, J. R., Boundary Conditions for the Diffusion Solution of Coupled Conduction-Radiation Problems, NASA Technical Note, NASA TN D-4618, 1968.

70. Howell, J., Personal Communication, 2009.

71. Lallemant, N., Sayre, A., and Weber, R., Evaluation of Emissivity Correlations for H2O-CO2-N2/Air Mixtures and Coupling with Solution Methods of the Radiative Transfer Equation, Prog.Energy Combust.Sci., Vol. 22, pp. 543-574, 1996.

72. Denison, M. K. and Webb, B. W., An absorption line blackbody distribution function for efficient calculation of total gas radiative transfer, Journal of Quantitative Spectroscopy and Radiative Transfer, Vol. 50, No. 5, pp. 499-510, 1993.

73. Denison, M. K. and Webb, B. W., Development and application of an absorption-line blackbody distribution function for CO2, International Journal of Heat and Mass Transfer, pp. 1813-1821, 1995.

74. Denison, M. K. and Webb, B. W., The Spectral Line-Based Weighted-Sum-of-Gray-Gases Model in Nonisothermal Nonhomogeneous Media, Journal of Heat Transfer, Vol. 117, No. 2, pp. 359-365, ASME, 1995.

75. Denison, M. K. and Webb, B. W., The Spectral-Line Weighted-Sum-of-Gray-Gases Model for H2O/CO2 Mixtures, Journal of Heat Transfer, Vol. 117, No. 3, pp. 788-792, ASME, 1995.

76. Denison, M. K. and Webb, B. W., The Absorption Blackbody Distribution Function at Elevated Pressure, First International Symposium on Radiation Transfer, Vol. 1, pp. 228-238, 1995.

77. Rothman, L. S., Gamache, R. R., Tipping, R. H., Rinsland, C. P., Smith, A. H., Benner, D. C., Devi, V. M., Flaud, J.-M., Camy-Peyret, C., Perrin, A., Goldman, A., Massie, S. T., Brown, L. R., and Toth, R. A., The HITRAN molecular database: Editions of 1991 and 1992, Journal of Quantitative Spectroscopy and Radiative Transfer, Vol. 48, No. 5/6, pp. 469-507, 1992.

78. Modest, M. F. and Zhang, H., The full-spectrum correlated-*k* distribution for thermal radiation from molecular gas-particulate mixtures, ASME Journal of Heat Transfer, Vol. 124, No. 1, pp. 30-38, 2002.

79. Smith, T. F., Shen, Z. F., and Friedman, J. N., Evaluation of Coefficients for the Weighted Sum of Gray Gases Model, ASME Journal of Heat Transfer, Vol. 104, pp. 602-608, 1982.

80. Vos, J. B., Rizzi, A. W., Corjon, A., Chaput, E., and Soinne, E., Recent advances in aerodynamics inside the NSMB (Navier Stokes Multi Block) consortium, Aerospace Sciences Meeting and Exhibit, 36th, Reno, 1998.

81. Vos, J. B. e. al., NSMB Handbook Version 4.5, Lausanne, Switzerland, CFS Engineering, 1999.

82. Pai, S. I., Inviscid flow of radiation gas dynamics, Journal of Mathematical and Physical Sciences, Vol. 39, pp. 361-370, 1969.

83. Özisik, M. N., Radiative Transfer and Interactions With Conduction and Convection, John Wiley & Sons, New York, 1973.

84. Thellmann, A., Mundt, Ch., Welch, C., and Jack, C., Entry of a Solar Kite into a Planetary Atmosphere, 56th International Astronautical Congress, Fukuoka / Japan, 2005.

85. Heaslet, M. A. and Warming, R. F., Radiative Transport and Wall Temperature Slip in an Absorbing Planar Medium, International Journal of Heat and Mass Transfer, Vol. 8, No. 7, pp. 979-994, 1965.

86. Ness, A. J., Solution of Equations of a Thermal Network on a Digital Computer, Solar Energy, Vol. 3, No. 2, pp. 37, 1959.

87. Weber, C., Développement de méthodes implicites pour les équations de Navier-Stokes moyennées et la simulation des grandes échelles: Application à l'aérodynamique externe, Institut National Polytechnique de Toulouse, 1998.

88. NSMB Wiki, http://www.unibw.de/thermo/mitarbeiter/, Points of Contact: Mundt, Göbel, Thellmann, 22.05.2010, 15:30 h, 2010.

89. Göbel, F., Implementation of Spectral Models for Gas Radiation into the CFD Solver NSMB and Validation on the basis of the SSME Main Combustion Chamber, Universität der Bundeswehr München, Institute of Thermodynamics, 2009.

90. Coppalle, A., The Total Emissivities of High Temperature Flames, Combustion & Flame, Vol. 49, pp. 101-108, 1983.

91. Johansson, R., Leckner, B., and Andersson, K., Account for ratios of H2O to CO2 in the calculation of thermal radiation of gases with the weighted sum of grey gases model, Proceedings of the 6th Mediterranean Combustion Symposium, 2009.

92. Birgel, D., CFD Simulation of the SSME Main Combustion Chamber operated by H2-O2 and CH4-O2 with CFX and FLUENT including Thermal Gas Radiation, Universität der Bundeswehr München, Institute of Thermodynamics, 2010.

93. Schmidt, E., Messung der Gesamtstrahlung des Wasserdampfes bei Temperaturen bis 1000 °C, Zeitschrift Technische Mechanik und Thermodynamik, Vol. 3, pp. 57-70, 1932.

94. Rocketdyne, Fact Sheet Rocketdyne SSME, Canoga Park, 2005.

95. Menter, F. R., Two-equation eddy-viscosity turbulence models for engineering applications, AIAA-Journal, Vol. 32, No. 8, pp. 1598-1605, 1994.

96. Spalart, P. R. and Allmaras, S. R., A One-Equation Turbulence Model for Aerodynamic Flows, AIAA Paper 92-0439, 1992.

97. Magnussen, B. F., The Eddy Dissipation Concept for Turbulent Combustion Modelling. Its Physical and Practical Implications, Presented at the First Topic Oriented Technical Meeting, International Flame Research Foundation, IJmuiden, The Netherlands, 1989.

98. Edwards, D. K. and Matavosian, R., Scaling Rules for Total Absorptivity and Emissivity of Gases, Journal of Heat Transfer, Vol. 106, pp. 684-689, 1984.

99. Sisco, J., https://engineering.purdue.edu/AAE/Academics/Courses/aae539/2007/spring/homework_projects/homework_project_1/hwkprj1contour.xls, 21.12.2009, 13:30., 2010.

100. Gordon, S. and McBride, B. J., Computer Program for Calculation of Complex Chemical Equilibrium Compositions, Rocket Performance, Incident and Reflected Shocks, and Chapman-Jouget Detonations, NASA-SP-273, Glenn Research Center, 1976.

101. Williams, W., Report of the SSME Assessment Team, 1993.

102. Göbel, F., Birgel, D., and Thellmann, A., CFD Simulation of Hydrogen-Oxygen and Methane-Oxygen System for Space Shuttle Main Combustion Chamber including Radiative Effects, 60th International Astronautical Congress, 2009.

103. Otto, O., CFD Simulation of Methane-Oxygen System for Space Shuttle Main Combustion Chamber including Radiative Effects, Munich, Universität der Bundeswehr München, Faculty of Aerospace Engineering, Institute of Thermodynamics, 2009.

104. Versteeg, H. K. and Malalasekera, W., An introduction to computational fluid dynamics - The finite volume method, Longman Scientific & Technical, Essex, 1995.

105. Schuldt, A., http://www.mainengine.de/ssme/ssme_haupttrw.html, 23.12.2009, 11:44., 2009.

106. Fluent Inc., FLUENT 6.3 User Guide, 2006.

107. ANSYS CFX 11.0, ANSYS CFX-Solver Theory Guide, 2006.

108. Mangler, W., Zusammenhang zwischen ebenen und rotationssymmetrischen Grenzschichten in kompressiblen Flüssigkeiten, Zeitschrift für Angewandte Mathematik und Mechanik (ZAMM), Vol. 28, pp. 97-103, 1948.

109. Schlichting, H. and Gersten, K., Grenzschicht-Theorie, Vol. 10. Auflage, Springer-Verlag, Berlin, Heidelberg, 2006.

110. Modest, M. F., Personal Communication, 2009.